TESIS DE DOCTORADO

THERMAL CONDUCTIVITY OF SUPERLATTICES AND FERROELECTRIC THIN FILMS. EFFECT OF BOUNDARY SIZES AND VACANCIES

David Bugallo Ferrón

ESCUELA DE DOCTORADO INTERNACIONAL DE LA UNIVERSIDAD DE SANTIAGO DE COMPOSTELA

PROGRAMA DE DOCTORADO EN CIENCIA DE MATERIALES

SANTIAGO DE COMPOSTELA

AÑO 2021

DECLARACIÓN DEL AUTOR DE LA TESIS

Thermal conductivity of superlattices and ferroelectric thin films. Effect of boundary sizes and vacancies

D./Dña. David Bugallo Ferrón

Presento mi tesis, siguiendo el procedimiento adecuado al Reglamento, y declaro que:

1) *La tesis abarca los resultados de la elaboración de mi trabajo.*
2) *En su caso, en la tesis se hace referencia a las colaboraciones que tuvo este trabajo.*
3) *La tesis es la versión definitiva presentada para su defensa y coincide con la versión enviada en formato electrónico.*
4) *Confirmo que la tesis no incurre en ningún tipo de plagio de otros autores ni de trabajos presentados por mí para la obtención de otros títulos.*

En Santiago de Compostela, 3 de mayo de 2021.

Fdo.....

AUTORIZACIÓN DEL DIRECTOR/TUTOR DE LA TESIS

D./Dña. **José Francisco Rivadulla Fernández**

En condición de: **Tutor/a y director/a**

Título de la tesis: Thermal conductivity of superlattices and ferroelectric thin films. Effect of boundary sizes and vacancies

INFORMA:

Que la presente tesis, se corresponde con el trabajo realizado por D/Dña **David Bugallo Ferrón**, bajo mi dirección/tutorización, y autorizo su presentación, considerando que reúne los requisitos exigidos en el Reglamento de Estudios de Doctorado de la USC, y que como director/tutor de esta no incurre en las causas de abstención establecidas en la Ley 40/2015.

En **Santiago de Compostela**, **30 de Abril de 2021**

Firma electrónica

AUTORIZACIÓN DEL DIRECTOR/TUTOR DE LA TESIS

D./Dña. **Eric Langenberg Pérez**

En condición de: **Director/a**

Título de la tesis: Thermal conductivity of superlattices and ferroelectric thin films. Effect of boundary sizes and vacancies

INFORMA:

Que la presente tesis, se corresponde con el trabajo realizado por D/Dña **David Bugallo Ferrón**, bajo mi dirección/tutorización, y autorizo su presentación, considerando que reúne los requisitos exigidos en el Reglamento de Estudios de Doctorado de la USC, y que como director/tutor de esta no incurre en las causas de abstención establecidas en la Ley 40/2015.

En **Barcelona**, **30 de abril de 2021**

Firma electrónica

Document signat digitalment per: Eric Langenberg Perez

CONTENTS

Motivation 3

Objectives 6

1. Introduction 7

1.1. Phonons and heat transport 7

1.2. Phonon scattering mechanisms: Debye model 13

1.2.1. Analysis of the thermal conductivity of a model oxide: $SrTiO_3$. 18

1.3. Active control of the thermal conductivity 25

1.3.1. Ferroelectric materials 29

2. Experimental techniques 35

2.1. X-ray methods 35

2.2. The 3ω method 44

2.2.1. Analysis of the possible sources of error 51

3. Thermal conductivity of $SrTiO_3/LaCoO_3$ Superlattices 55

3.1. Objectives of the chapter, context and discussion of previous results 55

3.2. Fabrication of the $SrTiO_3/LaCoO_3$ superlattices 65

3.3. Structural characterization of the superlattices 70

3.4. Thermal conductivity of the superlattices 77

3.5. Conclusions 94

4. Thermal conductivity of $BaTiO_3$. Effect of stoichiometry and Size 95

4.1. Objectives of the chapter, context and discussion of previous results 95

4.2. Fabrication of $BaTiO_3$ thin films. 99

4.3. Structural characterization of the films 102

4.4. Thermal conductivity of the films 117
4.5. Conclusions 123
5. Thermal conductivity of $PbTiO_3$ thin films: Effect of stoichiometry and ferroelectric domain walls 125
5.1. Objectives of the chapter, context and discussion of previous results 125
5.2. Fabrication of the $PbTiO_3$ films 130
5.3. Structural characterization of the films 133
5.4. Thermal conductivity of the films 144
5.5. Conclusions 150
6. General Conclusions and outlook 151
Resumo en Galego 153
Técnicas experimentais 157
Resultados e conclusións 159
Conclusións xerais 166
Bibliography 167
Anex: figure permissions 189

MOTIVATION

The most recent evolution the world has experienced is probably the one based on the control of electrons. Electronics has certainly revolutionized the way we communicate, store information, and live our lives in general. Since the first transistor was invented and built in 1947, earning Shockley, Bardeen and Brattain the Nobel Prize in Physics in 1956,[1] the rise of new, faster, smaller and more reliable technological devices has been continuous. On the other hand, photonics has also helped this evolution greatly, particularly with the introduction of optical fibers, enabling faster transmission of big amounts of data over large distances. It has also led to other important contributions to society such as the screens on modern electronic devices. The control on the transport of electrons and photons, the two particles that transmit electric current and light respectively, has hence enabled humanity to attain the level of development it has reached.

The transmission of sound is probably one of the most rudimentary techniques our species and many others use to communicate. Furthermore, sound is linked to the evolution of ancient and modern

languages, thus covering an important role in the evolution of human societies. The study of the transmission of sound has led to various applications, such as sonars[2] and ultrasound imaging[3]. Nevertheless, there is a lack of active control on the particle responsible for the transmission of both sound and heat in electrically insulating solids, the phonon. **Phonons** are the normal vibrational modes of single crystalline materials in which all atoms vibrate collectively. These quasiparticles (as they cannot be defined without the media through which they travel) carry the heat in electrically insulating materials and experience a series of scattering processes that determine the final thermal conductivity of the system.[4]

Recent advancements in phononics[5] have led to the design of thermal and acoustic diodes,[6–8] an important step forward towards the design of phononic circuits. However, a reliable thermal transistor that allows control on the passage of phonons has not yet been obtained. This phonon valve would constitute an essential element for a logic phononic circuit, as well as enable the control of heat flow in solid devices.[9] The control over the propagation of coherent phonons in nanostructures is essential also in the development of new ways of information processing.[10,11]

The goal of this thesis is to study thermal transport in two kinds of technologically relevant structures: superlattices and thin films of ferroelectric materials.

The thesis is organized as follows:

In the first chapter I will present a brief introduction to the main factors that affect the thermal conductivity in crystalline insulating solids. I will present the theoretical models that we used to guide ourselves in the formulation of the initial hypothesis, and in the analysis of the results.

In Chapter 2, I will discuss the most relevant experimental techniques used for the characterization of the samples studied in this thesis. I will present in deeper detail the main characteristics of the different types of X-ray analysis, as well as of the 3ω method, used to measure the thermal conductivity of the samples.

The experimental results will be presented in Chapters 3-5; a brief introduction to the most relevant results and literature of each part, as well as a clear motivation of the study, is presented at the beginning of each chapter.

Chapter 3 deals with the systematic study of the effect of thickness and periodicity on heat transport in epitaxial oxide superlattices.[12–14]

Chapters 4 and 5 will focus on the study of thermal transport in two relevant ferroelectric perovskites: $BaTiO_3$ and $PbTiO_3$. In particular, I will discuss the effect of point defects and/or ferroelectric domain walls, and how they may affect the propagation of phonons in thin films of these materials.

OBJECTIVES

The objective of Chapter 3 is to understand how coherent and incoherent phonons contribute to the heat transport in superlattices, and analyze the coherent-to-incoherent crossover that has been suggested to exist. Particularly it will also focus on how the total thickness and period thickness affects the thermal conductivity as well as changes to the periodicity itself.

The objectives of Chapters 4 and 5 are to understand thermal transport in two of the most relevant ferroelectric materials, how the domain walls affect them and also how cationic defects can not only affect thermal transport but also the ferroelectricity of the materials.

The final objective is that the results presented in this thesis contribute to a better understanding of the phenomena of thermal transport in thin oxide films, in order to achieve active control over heat transport in nanostructures.

1. INTRODUCTION

1.1. PHONONS AND HEAT TRANSPORT

When a system in thermodynamic equilibrium is subjected to the action of a thermal gradient, a flux of heat is stablished to restore the equilibrium state. For a small enough thermal gradient, the relationship between the flux and the temperature gradient is linear, and the proportionality constant is the thermal conductivity, κ. Under these premises, a general expression for the thermal conductivity can be easily derived in the framework of the kinetic theory of gases:[15]

$$\kappa = \frac{1}{3} C v \lambda \qquad \textbf{(1.1)}$$

C is the heat capacity per unit volume, v is the velocity of the molecules of the gas, and λ is their mean free path. In general, we could say that to calculate the thermal conductivity of any system, it is necessary to know the energy stored in the excitations responsible for the transport of heat, their propagation speed, and for how long they can travel before being effectively scattered in a process that contributes to the thermal resistance.

In the case of crystalline insulating solids, as the materials studied in this thesis, the particles that transport heat are coherent atomic vibrations, called *phonons*.[4] Phonons are the equivalent in crystalline solids to normal vibration modes in molecular language, *i.e.* coordinate movements of all the atoms of the molecule, that occur at a given natural frequency.[16] The thermodynamic and transport properties of the lattice (specific heat, thermal conductivity, etc) must then be some function of the energy distribution of these particles, its excitation spectrum. Obtaining the total spectrum of the crystal, requires solving the equations of motion for the local forces at play; this problem can be treated relatively easily in a crystalline solid, due to the translational symmetry and the Bloch theorem (*for any wavefunction that satisfies the Schrödinger equation, there exists a vector, k, such that translation by a lattice vector l is equivalent to multiplying by a phase factor* e^{ikl}).[17]

In the simplest approximation of a crystalline solid (a one-dimensional monoatomic chain composed of N atoms of mass *m*, spaced a distance *a*) the frequency of each phonon can be obtained as a solution of the equation of motion in the harmonic oscillator approximation, as:

$$\omega_k = \sqrt{\frac{\alpha}{m}}\, 2\, sin\left(\frac{ka}{2}\right) \quad (1.2)$$

α is the force constant, and k is the momentum of the phonon. Because of the periodic nature of the wavefunction, the N values of k are within $\pm\pi/a$; any other value has an equivalent inside this region. As

shown in Figure 1.1, when the wavelength (momentum) is much larger (smaller) than the interatomic distance, *a*, the solid behaves as an elastic continuum, with the waves moving at a speed $\sqrt{\frac{\alpha}{m}}a$. At larger *k*, phonons are progressively dispersed, *i.e.* their velocity becomes a function of the momentum, as the wave vector approaches the limit of the Brillouin zone at π/a.

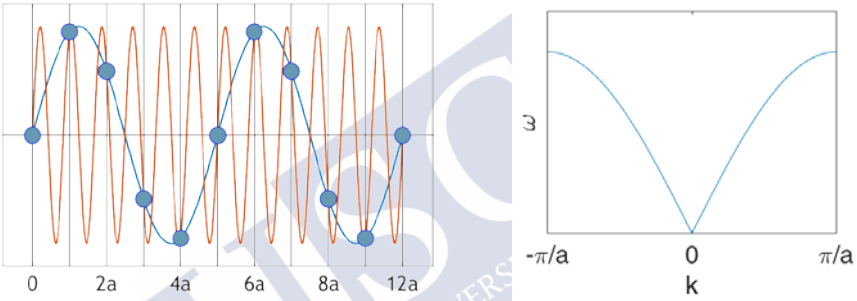


Figure 1.1. Left: representation of two phonons, with different k, which carry the same information, as the position of all the atoms is the same for both waves, where a is the interatomic distance. Right: phonon dispersion of a monoatomic chain, in the harmonic oscillator approximation.

Solving the equations of motion for a slightly more complicated 1D chain, composed of two atoms of different masses arranged periodically --m-M-m-M-m-M--, keeping the same interatomic distance, *a*, and force constant, α, gives two solutions for the frequency at a given *k* (Figure 1.2):

$$\omega_{\pm}^{2} = \alpha\left(\frac{1}{m}+\frac{1}{M}\right) \pm \alpha\sqrt{\left(\frac{1}{m}+\frac{1}{M}\right)^{2} - \frac{4\,sin^{2}\,ka}{mM}} \qquad (1.3)$$

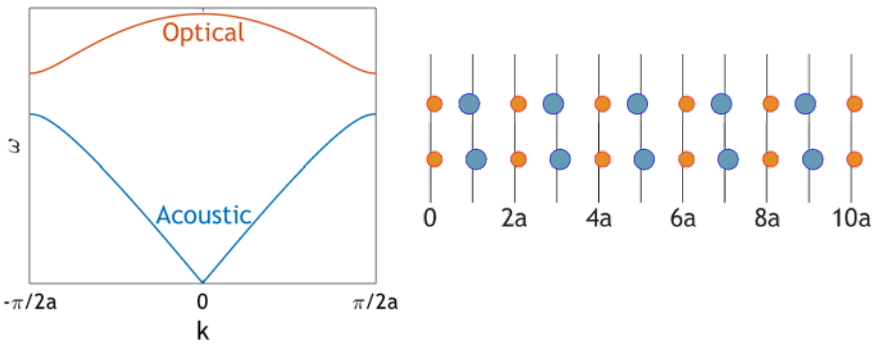


Figure 1.2. Left: phonon dispersion for a diatomic line of atoms separated by a distance a. Right: representation for an optical (top) and acoustic(bottom) modes in a diatomic line. The black lines represent the equilibrium position of each atom.

The solution at lower ω shows the same linear proportionality to *k*, at $k \rightarrow 0$, and it is called the *"acoustic branch"*; the other solution at higher ω, whose frequency at $k \rightarrow 0$ is $2\alpha\left(\frac{1}{m}+\frac{1}{M}\right)$, defines a movement in which m and M displace opposite to each other. In an ionic crystal, this movement creates an oscillating dipolar moment, which can be excited by an electromagnetic radiation; this solution is called the *"optical branch"*.

Optical phonons have a small group velocity (the derivative of their dispersion curves shown in Figure 1.3 for a diatomic linear chain) and hence can be neglected in a first approximation when calculating the thermal conductivity of materials. However, they may have an important indirect effect over the propagation of acoustic phonons: for instance, Christensen *et al.*[18] reported how the lowering of the optical branch in a host-guest structure causes the acoustic band to flatten,

leading to a lowering of the speed of phonons and therefore a reduction of the thermal conductivity.

Adding one or two extra dimensions to the crystal, adds new branches to the phonon spectrum, which are distinguishable by their polarization: transverse or longitudinal, with respect to the direction of propagation of the wave. The longitudinal branch has the largest velocity, due to the largest restoring forces with respect to transverse, shear waves.

To calculate the specific heat of these heat-carrying excitations in equation 1.1, we must first determine their total average energy or population of phonons at any value of *k*, in thermal equilibrium at any temperature. This can be done from the Bose-Einstein distribution function, so that the total average energy is:

$$E = \sum_{k,p} \frac{\hbar\omega_{k,p}}{e^{\frac{\hbar\omega_{k,p}}{Tk_B}} - 1} \qquad \textbf{(1.4)}$$

(the index *p* represents the three polarizations). The specific heat, at constant volume:

$$C = \frac{dE}{dT} = \frac{1}{Vk_BT^2} \sum_p \int d\omega D_p(\omega) \frac{(\hbar\omega_{k,p})^2 e^{\frac{\hbar\omega_{k,p}}{Tk_B}}}{\left(e^{\frac{\hbar\omega_{k,p}}{Tk_B}} - 1\right)^2} \qquad \textbf{(1.5)}$$

Where $D_p(\omega)$ is the frequency distribution, the fraction of phonons of a branch with frequencies between ω and ω+dω. Introducing a cutoff at a maximum frequency $\omega_D = k_B\Theta_D/\hbar$, and assuming the same velocity for each branch (the Debye approximation):[4]

$$C = 9Nk_B\left(\frac{T}{\Theta_D}\right)^3 \int_0^{\Theta_D/T} \frac{x^4 e^x}{(e^x-1)^2}\,dx \qquad \textbf{(1.6)}$$

$x = \frac{\hbar\omega}{k_B T}$; Θ_D is the Debye temperature. In the low temperature limit, this expression produces the famous $C \propto T^3$ temperature dependence observed in crystalline solids.[15]

Inserting this expression back in 1.1, for an isotropic solid, in the relaxation time approximation, results in a final expression for the thermal:[19]

$$\boldsymbol{\kappa_{(T)} = \frac{1}{2v\pi^2}\int_0^{\omega_D} \tau(\omega)\frac{\hbar^2\omega^4}{k_B T^2}\frac{e^{\frac{\hbar\omega}{k_B T}}}{\left(e^{\frac{\hbar\omega}{k_B T}}-1\right)^2}d\omega} \qquad \textit{(1.7)}$$

Note that the integrand of this expression represents the spectral thermal conductivity, the contribution of each frequency to the thermal conductivity at a given T. This magnitude can be very informative and will be discussed in different parts along this thesis.

The key for the approximate calculation of the thermal conductivity is the calculation of the relaxation time of the phonons, τ(ω), due to the different scattering mechanisms that reduce the thermal conductivity.

In the next section, I discuss in detail the approximate calculation of $\tau(\omega)$ for the main events of scattering discussed in this thesis.

1.2. PHONON SCATTERING MECHANISMS: DEBYE MODEL

The different mechanisms that contribute to the total thermal resistance can be considered (in a first approximation) as independent of each other, so they add as terms of a summation of scattering probabilities (inverse of relaxation times, τ). In this thesis, we will consider the effect of Umklapp or phonon-phonon scattering, boundary scattering, and point defect scattering.

A rapid estimation of the phonon mean free path and its temperature dependence, $\lambda(T)$, can be made assuming that local fluctuations of density, $<\Delta>$, induced by temperature, will scatter phonons with a probability proportional to the mean square of its amplitude: $\lambda^{-1} \approx \gamma^2 <\Delta^2>/a$ (a is a length of the order of the lattice constant and γ is the Grüneissen parameter)[4]. Given the proportionality between $<\Delta^2>$ and the thermal energy, $k_B T$, we may reach an expression for λ inversely proportional to T. This approximation is strictly valid only at high temperatures, where specific heat and sound velocity may be considered as constants, so that the total thermal conductivity varies as 1/T also.

However, at low temperatures, below the Debye Temperature, the situation is more complex, as the thermal fluctuations of density are essentially the same as the phonons themselves, and the problem of determining λ reduces to the calculation of the scattering rate of phonon-phonon processes.

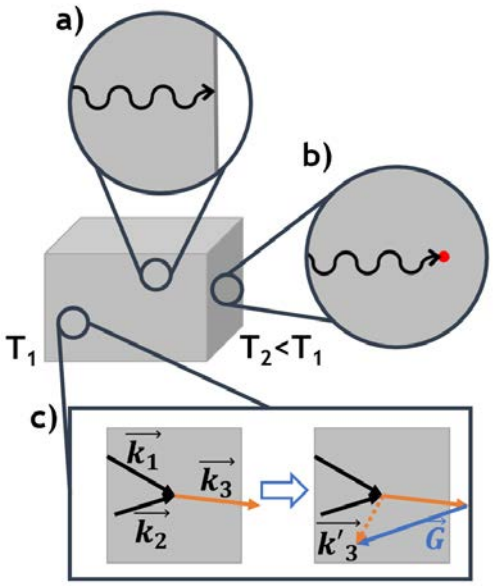


Figure 1.3. Scheme representing the three possible phonon scattering mechanisms in a crystalline solid: a) by a boundary, b) by a defect, and c) Umklapp process where the box represents the first Brillouin zone. If the resulting phonon, with moment $\vec{k_3}$ lies outside the first Brillouin zone, it is transformed into one inside it by a reciprocal lattice vector $\vec{G}$.

Two phonons can recombine giving place to a different one, with different momentum. If the resulting momentum lies inside the first Brillouin zone of the material, this is called a "Normal process" (N-process) and the total momentum is conserved. If the momentum of the resulting phonon is outside the first Brillouin zone, the phonon-phonon scattering event is called "Umklapp process" (U-process). In this case, that mode will be transformed into one inside the first Brillouin zone by the addition of reciprocal lattice vector $\vec{G}$, which relates two different points in the reciprocal space where

phonons are represented (Figure 1.3 c,). This process, while conserving the energy, does not conserve the total momentum of the system (that is why crystal momentum cannot be considered totally equivalent to a classical momentum).

Thermal resistance due to phonon-phonon scattering is largely due to U-processes, and the probability of such events is determined by the product of the phonon number at the appropriate *k* and *k'* states (*k*+*k'*=*k''*+*G*), determined by the Boltzmann factor:

$$n_k n_{k'} \approx e^{-\hbar\nu/k_B T} e^{-\hbar\nu'/k_B T} \sim e^{-\theta/k_B T}$$

Thus, the mean free path of phonons (and hence thermal conductivity) increases exponentially as temperature decreases, until it reaches the physical diameter of the crystal, ϕ. The proportionality constant must include the Grüneisen parameter (γ), that describes the change in frequency with volume,[20] the average mass per atom $\overline{M}$, the speed of phonons and the Debye temperature Θ_D (the characteristic vibrational energy scale of the material).[21–24]

Below this limiting temperature, $\lambda \approx \phi$, the thermal conductivity is determined by the temperature dependence of the specific heat in the Debye approximation ($\propto T^3$). There is then a limiting boundary scattering mechanism, related to the size of the crystal; ϕ (called the Casimir length) is determined by the grain boundaries in polycrystalline materials, or the diameter of an effective cross-sectional area in the case of a single crystal.[25,26]

Finally, on interacting with point defects of size smaller than their wavelength, phonons will experience a scattering of the Rayleigh type,[21] proportional to the fourth power of the frequency, $C\omega^4$. These point defects can be atomic substitutions (isotopes, etc), a vacancy, or an interstitial atom. The parameter of $C\omega^4$, contains the information about the size and concentration of defects (the average volume per atom, δ^3, and the molar fraction of each type of defect, x_i), as well as the differences in mass, radius, and the bond-strength around the defect.[27] These are embodied in the parameter S_i, for the different N positions on the lattice.

$$S_i^2 = S_1^2 + (S_2 + S_3)^2$$

$$S_1 = \frac{\Delta M}{M}\frac{1}{2\sqrt{3}}, S_2 = \frac{\delta(v^2)}{v^2}\frac{1}{\sqrt{6}} = -2\gamma\frac{\Delta R}{R}\frac{1}{\sqrt{6}}, S_3 = -Q\gamma\frac{\Delta R}{R}\sqrt{\frac{2}{3}}$$

$$S_i^2 = \frac{1}{12}\left(\frac{\Delta M}{\bar{M}}\right)^2 + \frac{2}{3}\left(1 + \frac{2}{\sqrt{3}}Q + \frac{1}{3}Q^2\right)\gamma^2\left(\frac{\Delta R}{\bar{R}}\right)^2 \quad \textbf{(1.8)}$$

where ΔM (ΔR) is the change of mass (radius) caused by the defect with respect to the average, and Q is a factor which depends on the harmonicity of the bonds, according to Klemens.[27]

However, this approach assumes that every position in the crystal is equal. In reality, since there is a big difference in both mass and radius between the distinct ions forming the material, the contributions for the different atoms can be separated, allowing for a better description of the

system to be achieved. Consequently, in a system $A_aB_bC_c$ we can divide the lattice in three sublattices, which in perovskites (the case in all the materials in this thesis) are the A and B cations and the oxygen atoms, respectively.[28,29]

$$S_i^2 = S_1^2 + (S_2 + S_3)^2 = \frac{a}{a+b+c}\left[\frac{1}{12}\left(\frac{M_A}{\bar{M}}\right)^2 + \frac{2}{3}\left(1 + \frac{2}{\sqrt{3}}Q + \frac{1}{3}Q^2\right)\gamma^2\left(\frac{R_A}{\bar{R}}\right)^2\right] + \frac{b}{a+b+c}\left[\frac{1}{12}\left(\frac{M_B}{\bar{M}}\right)^2 + \frac{2}{3}\left(1 + \frac{2}{\sqrt{3}}Q + \frac{1}{3}Q^2\right)\gamma^2\left(\frac{R_B}{\bar{R}}\right)^2\right] + \frac{c}{a+b+c}\left[\frac{1}{12}\left(\frac{M_C}{\bar{M}}\right)^2 + \frac{2}{3}\left(1 + \frac{2}{\sqrt{3}}Q + \frac{1}{3}Q^2\right)\gamma^2\left(\frac{R_C}{\bar{R}}\right)^2\right] \quad (1.9)$$

Thus, adding the scattering probabilities of these three processes as independent of each other:[19,21–24,28,30]

$$\tau^{-1}(\omega) = \tau_B^{-1} + \tau_U^{-1} + \tau_D^{-1} = A + B\omega^2 T e^{-\frac{\Theta_D}{\alpha T}} + C\omega^4 = \frac{v}{\phi} + \frac{\hbar\gamma^2}{\bar{M}v^2\Theta_D}\omega^2 T e^{-\frac{\Theta_D}{\alpha T}} + \frac{3\delta^3}{\pi v^3}\sum_{i=1}^{N} x_i S_i^2 \omega^4 \quad (1.10)$$

The terms A, B and C are related to the boundary scattering, Umklapp or phonon-phonon scattering and point defect scattering, respectively. The term α in the exponential of the Umklapp term is a fitting parameter, that normally spans between 1-3.[21]

We have now a set of several equations to calculate the main contributions to the thermal conductivity of a real material, using the equations (1.7)-(1.10). These expressions, although they might look very simple and based on crude approximations (like considering a single velocity for all phonons), allow an intuitive interpretation of the

main scattering mechanisms contributing to the thermal conductivity of solids, as will be further discussed in this work. Particularly, this approach will be used in this thesis as a guide to disentangle the contributions of defects and boundaries in different situations, with the purpose of understanding how thermal transport can be influenced and controlled.

1.2.1. Analysis of the thermal conductivity of a model oxide: $SrTiO_3$.

To show the effect of the different scattering mechanisms on the thermal conductivity of a model system, we are going to perform some of the calculations of the previous section for the case of $SrTiO_3$ (STO) thin films, using the experimental values available in the literature. This will serve to illustrate how we came to formulate some of the starting hypotheses, and the materials chosen to test them. In the end, since the aim of this thesis is to understand and control the thermal conductivity of different nanostructured materials, it is of the utmost importance to have an initial have an initial idea as accurate as possible, about the effect of the different scattering mechanisms, in different length and frequency scales, temperature, and any other parameter that we can control in our experiments.

First, we can calculate the magnitude of the Umklapp parameter, which should be intrinsic to the material itself and should be the least influenced by a change in the physical dimensions of the system. Using

data from literature[31] (shown in Table 1.1) the Umklapp contribution for strontium titanate was calculated as $\tau_U^{-1} = 2.66 \cdot 10^7 e^{-\frac{345}{T}} T\omega^2\ s^{-1}$.

Table 1.1. Data used for the calculation of the relaxation times.

γ	***2.75 (Ref. 31)***
V (m/s)	***5297 (Ref. 31)***
$\overline{M}$ ***(kg/mol)***	***0.0368***
Θ_D***(K)***	***690 (Ref. 31)***
δ^3 ***(m³)***	***1.29·10⁻²⁹***

The effect of the size boundary in a thin film of STO can be evaluated from the boundary scattering parameter: $\tau_B^{-1} = \frac{5297}{\phi} s^{-1}$. For our calculations we considered 3 different thicknesses: 10 nm, 100 nm, and 500 nm.

Finally, thin films of STO are expected to have a certain amount of vacancies and imperfections that form during growth.[32–35] Therefore, we have arbitrarily introduced a 1% of O^{2-} vacancies, plus a 1% of either Ti^{4+} or Sr^{2+} vacancies. The value of the relaxation time due to point defect scattering calculated in this way is $\tau_D^{-1} = 1.68 \cdot 10^{-42} \cdot \omega^4\ s^{-1}$ (for Sr vacancies), and $\tau_D^{-1} = 4.83 \cdot 10^{-42} \cdot \omega^4 s^{-1}$ (for Ti vacancies).

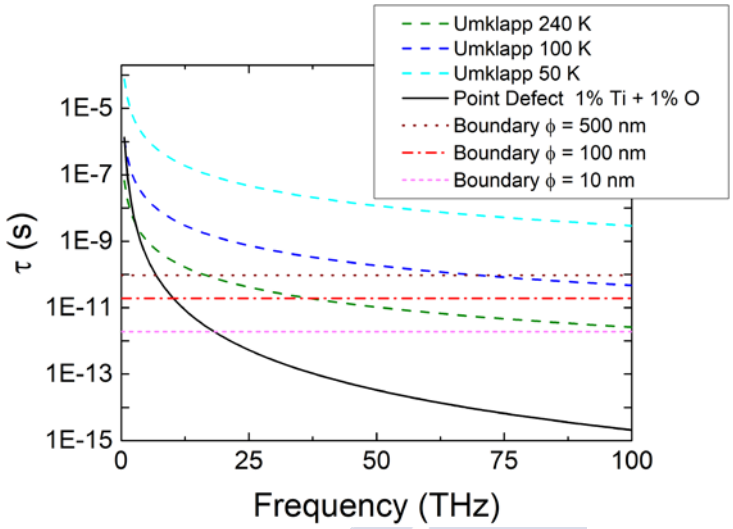


Figure 1.4. Relaxation times of the different scattering mechanisms calculated for $SrTiO_3$.

In Figure 1.4 we show the frequency dependence of the relaxation time for the different contributions, at 50 K, 100 K, and 240 K. The effect responsible for the smallest relaxation time will be the limiting scattering factor in the thermal conductivity.

The limiting factor for the propagation of high frequency phonons, above ≈15-20 THz, is the presence of point defects. However, ab initio calculations of the cumulative thermal conductivity in STO (Figure 1.5), show that the contribution of phonons above 15 THz is not so relevant, in the rage of temperatures studied in this thesis (data provided by A. O. Fumega).[36]

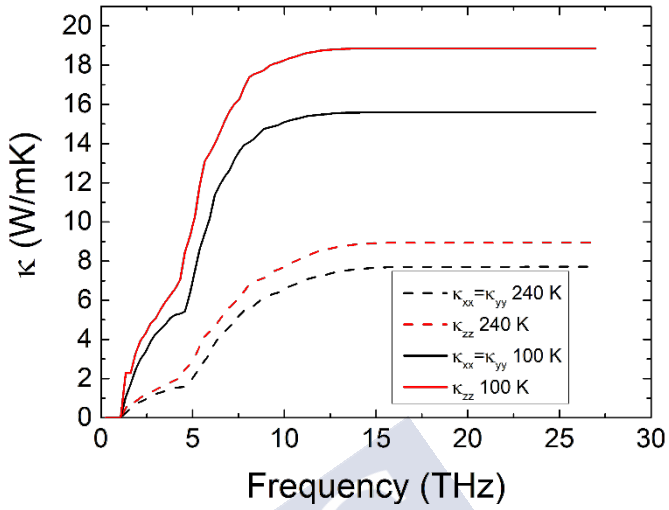


Figure 1.5. Accumulated thermal conductivity of the 0 K structure of $SrTiO_3$ at 240 and 100 K in the z direction (κ_{zz}) and x or y direction ($\kappa_{xx} = \kappa_{yy}$) (provided by A. O. Fumega, for more information on the calculation, see ref. [36])

On the other hand, at intermediate temperatures, around 100 K, the boundary scattering in the range 10-100 nm controls the relaxation time of phonons below ≈ 15-5 THz (Figure 1.4).[37] Thus, introducing artificial (or natural) boundaries in this range of sizes should be a useful strategy to control the thermal conductivity of STO.

The information in Figure 1.4 can be plotted in a more intuitive way: the integrand of the Debye equation for κ(T) (equation 1.7) represents the spectral thermal conductivity, *i.e.* a sort of spectrum of the contribution of the different frequency phonons to the thermal conductivity, at each temperature. In Figure 1.6 I plotted this magnitude for STO at different temperatures, using the Umklapp parameter calculated before, and $C = 7.13 \cdot 10^{-43}$ s^3 (obtained from the fit to a STO

thin film shown in Figure 1.7), and two different boundary sizes of 100 nm (to reproduce the effect of boundary scattering by the interfaces of a typical thin film) and 10 μm, to mimic a single crystal.

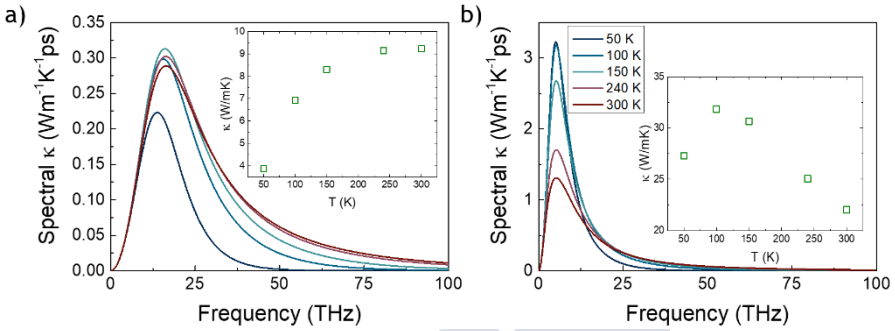


Figure 1.6. Spectral thermal conductivity for STO calculated from the Debye model using different temperatures and boundaries: a) 100 nm; b) 10 μm. The insets show the result of the integrated area of each curve, up to a cutoff frequency of 100 THz, which is the thermal conductivity at each temperature.

The spectral thermal conductivity shows how the relative contribution of higher frequency phonons, more susceptible to the effect of impurities and other small size imperfections, becomes important in the thin film. The effect of the boundary limits the propagation of lower frequency phonons, which are more important in the bulk, at low temperatures.

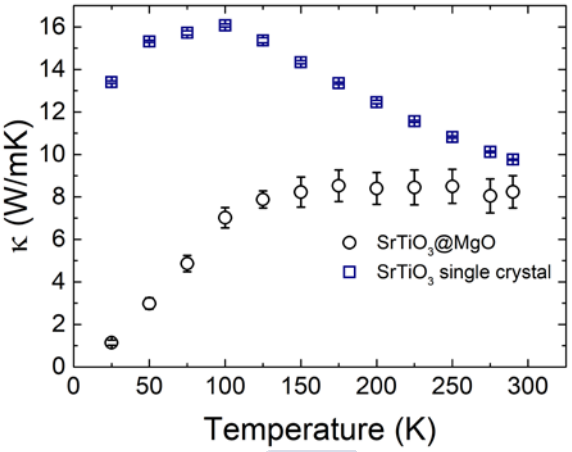


Figure 1.7. Thermal conductivity of a $SrTiO_3$ thin film, 80 nm thick, deposited on top of magnesium oxide (001), and a $SrTiO_3$ single crystal.

The thermal conductivity obtained from the numerical integration of the spectral κ, shown in the inset, reproduces the qualitative behavior of κ(T) of a single crystal and a thin film (80 nm) of STO, measured for the present thesis (Figure 1.7). As shown in both figures (calculated and experimental), the characteristic 1/T temperature dependence, and the maximum at ≈ 100 K, are suppressed in the thermal conductivity of the thin film due to boundary scattering.

Figure 1.8 shows spectral thermal conductivity calculated for STO, $BaTiO_3$ (BTO) and $PbTiO_3$ (PTO), three materials that will be studied in this thesis.

Panel a) shows the spectral thermal conductivity at 300 K, with a boundary size of 1 μm (single crystal) and a 1% of vacancies in the A site of the perovskite (Sr, Ba or Pb). BTO shows the higher contribution

from higher wavelengths: phonons below 30 THz are responsible for 44% of the total thermal conductivity in BTO, while this value increases to 66% for STO and to 75% for PTO. Thus, PTO is a good candidate for a study of the effect of boundary size over the thermal conductivity of an insulating oxide.

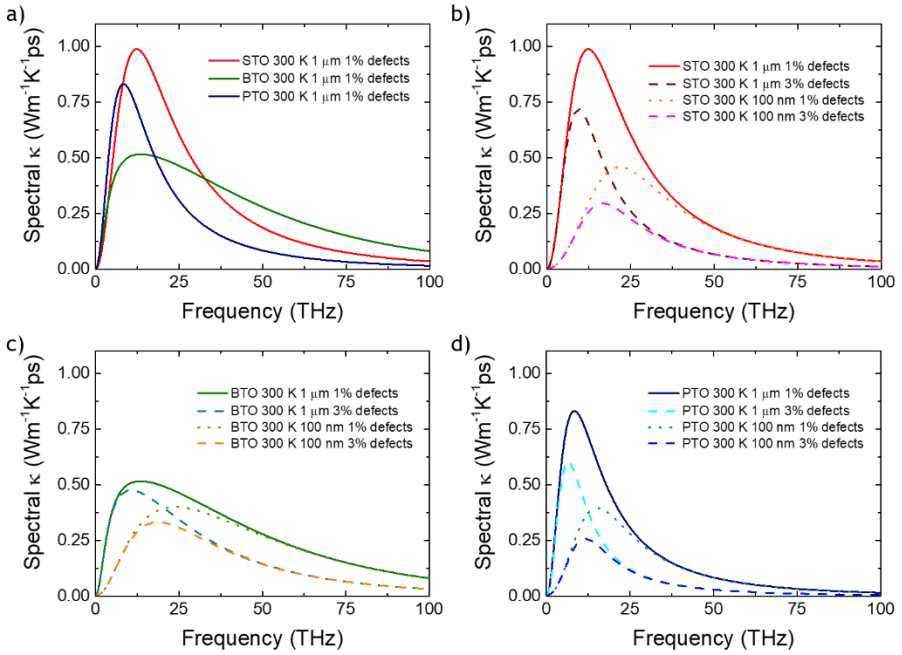


Figure 1.8. Spectral thermal conductivity at 300 K for STO, BTO, and PTO, respectively, with different boundaries and concentrations of defects in the A site of the perovskite. a) shows a comparison for the same concentration of A site; b), c) and d) show the effect of increasing the defect concentration and reducing the boundary size for STO, BTO and PTO, respectively.

On the other hand, increasing the concentration of vacancies leads to a reduction of the higher frequency phonons (Figure 1.8 b, c, and d). Given the lower contribution of low frequency phonons in BTO, this

material is comparatively better for a study of the effect of point defects on the thermal conductivity of an insulating oxide.

This type of guidance will be crucial when designing the different experimental approaches to control the thermal conductivity of these materials, as will be discussed in the experimental part of this thesis.

1.3. ACTIVE CONTROL OF THE THERMAL CONDUCTIVITY

As previously stated, the control achieved on electrons has allowed for the different electrical components and electronics as a whole. One key enabler is how much the electrical conductivity can be varied in certain materials. For example, on a field effect transistor the change in conductivity from the on to the off state can change up to 8 orders of magnitude.[38] This big change cannot be expected for the thermal conductivity, however. The main reason behind this is the available range of thermal conductivities in different materials compared to the range of electrical conductivities. While electrical conductivities in solids can range from 10^{-17} to 10^{7} S/m,[39,40] thermal conductivities are normally comprised between 0.026 W/mK for air[41] and 2230 W/mK for diamond[42] at room temperature. This is a huge difference, 20 orders of magnitude in solids for electrical conductivity compared to 6 in not only solid materials, but also gases, for thermal conductivity.

Here I will discuss some approaches currently pursued for an active control of the thermal conductivity, which range from the use of phase

change materials (PCMs), systems based on electrochemical processes, magnetic materials, liquids, ferroelectrics, etc.[43–49]

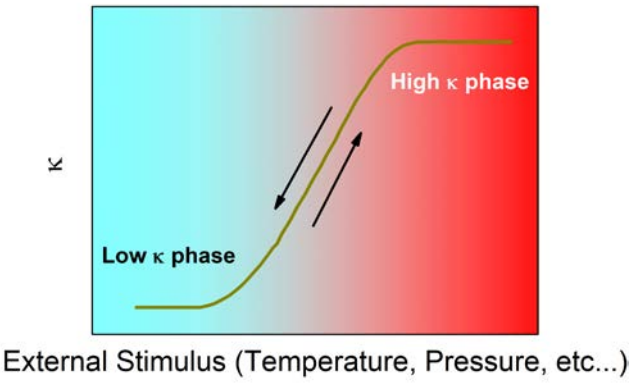


Figure 1.9. Scheme representing the change in thermal conductivity upon a change in an external stimulus such as temperature in the case of phase change materials.

In PCMs a change from one solid phase to another at T_C may lead to a large variation in thermal conductivity.[43] The main drawback of these systems is that they need to undergo a thermal cycling across T_C, and their operation is limited to the vicinity of the phase transition.

Liquid suspensions have also shown great changes in thermal conductivity upon melting and freezing cycles, in a similar mechanism to PCMs. For instance, Zheng *et al.*[46] demonstrated the possibility of achieving a reversible temperature regulation of thermal conductivity using liquid–solid phase transitions in stable suspension of graphite flakes in hexadecane. Their strategy consisted in a thermal cycling of the liquid across the freezing/melting temperatures, at a large enough concentration of graphite so that a percolated network of the flakes is

formed on freezing. This results in a reversible change of the thermal conductivity by a factor up to 3.2, depending on the loading of the dispersion. The use of different solvents and/or particle dispersed can change the temperature at which the melting/freezing happens, suggesting a new approach to this old problem.

A quite similar behavior can be observed in pure ionic liquids. Ionic liquids are formed by two organic ions of opposite charges, and they present a combination of coulombic and hydrogen bond intermolecular forces. López-Bueno *et al.*[47] have shown how, depending on the intermolecular interactions, these ionic liquids may form a solid crystalline phase or a glassy phase upon cooling. They showed a hysteretic behavior associated with a glass-crystal transition, with reversible changes higher than 30% in the thermal conductivity. Therefore, they are also plausible candidates for effective thermal regulation.

Electrochemical control of thermal conductivity has also been recently achieved, through reversible intercalation of Li^+ in MoS_2.[44] Although a change in *k* of an order of magnitude has been achieved, its main limitation is the long time required to switch from the *on* to the *off* state (in the order of minutes). However, this approach still poses as an interesting candidate for certain applications in energy harvesting or thermal management.

Ferromagnetic materials can also be a future candidate for such applications. Recently the thermal conductivity of monolayer CrI_3 was calculated for the ferromagnetic and paramagnetic state, shown to have a difference higher than 2 orders of magnitude.[48] The change is caused by the change in the structure due to spin-lattice coupling, that reduces phonon-phonon scattering, with a higher symmetry. Furthermore, the measurement of the thermal conductivity of iron oxide ferromagnetic packed beds under different field configurations and intensities has proven to increase the thermal conductivity as much as 15%.[49]

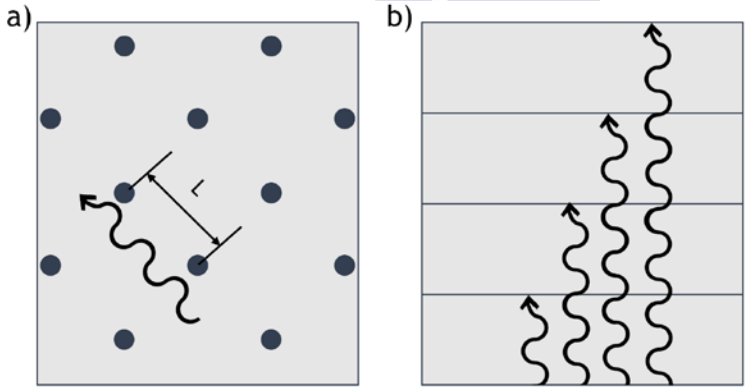


Figure 1.10. a) Scheme representing a phononic crystal. L must be in the order of the wavelength of the phonons to affect their dispersion. b) Scheme of an approach based on barriers to impede thermal conductivity; each barrier is a phonon scattering center.

It is also worth mentioning some cases in which there is a particular design to affect the thermal conductivity of the system without having a possibility to modify. This is the case of phononic crystals, in which periodic features such as holes are introduced in them, in such a way that they create a gap of momenta for phonons.[5,50,51] The introduction

of barriers, such as Ge nanodots in a Si matrix has also been used to reduce the thermal conductivity of systems,[52] which is required to improve the performance of thermoelectric materials.[53,54] This are schematized in Figure 1.10

However, probably above all these, the main focus is nowadays placed on ferroelectrics since these materials can achieve a fast and reliable thermal conductivity change with a relatively high on/off ratio. The use of electric fields to tune their κ, which can be rapidly switched at a constant temperature, offers important advantages over some of the methods previously discussed.

1.3.1. Ferroelectric materials

Ferroelectrics (FE) are a subclass of piezoelectric materials, which are not centrosymmetric and develop a spontaneous electric dipole in the unit cell.[55] The phenomenon of ferroelectricity was first discovered in 1920 in $KNaC_4H_4O_6 \cdot 4H_2O$, the Rochelle salt,[56] which was already known to be piezoelectric at the time. The particularity of ferroelectric materials, in opposition to piezoelectrics, is that their polarization can be reversed with an external electric field, which leads to interesting applications such as ferroelectric random access memories or FeRAMs.[57]

One of the most common types of FE material is that caused by ionic displacement. The origin of the ferroelectricity in this family of

compounds is a displacement of one atom in the unit cell from the position it should occupy to keep the material non-polar.[55] The mechanism behind it can be understood as a polarization catastrophe, in which the restoring forces that move the atom to that position are smaller than the local electric field that the polarization creates.[55] In $PbTiO_3$ (structure shown in Figure 1.11 a) and similar materials like $BaTiO_3$, the origin of the polarization is a tiny displacement of the Ti^{4+} from the center of the TiO_6 octahedra. The displacement of the atoms leads to the center of mass of positive charges (Pb^{2+} and Ti^{4+} cations) being different from the one of the negative charges (O^{2-} anions). The result is that the symmetry of the lattice is reduced from a high temperature (paraelectric) cubic phase to a low temperature (ferroelectric) tetragonal phase. In the case of $PbTiO_3$ the lone pair in Pb^{2+} also contributes to the tetragonal distortion.[58]

The proximity of the phase transition is foreshadowed by some optical phonon modes, which reduce their frequency substantially upon cooling from the paraelectric phase.[59] It is important to understand that the decrease of frequency does not result from a change in the bond strength, but from a loss of order, a braking of the bond itself, due to the proximity to the phase transition. Thus, the soft phonon mode precludes a decrease in crystal symmetry, and may have a huge impact in the thermal conductivity of a solid,[60] through strong scattering of acoustic modes.[60,61] This is the case for some materials even if they never actually reach the ferroelectric phase, with the phonon mode not

fully freezing. Imagine for a moment a crystal with two one atomic sublattices, and that one of them melts (a phase transition affecting just one of the sublattices). The melted phase cannot support transverse waves, and the vibrations associated to these mode cease to occur. The optical phonon associated with this mode is the soft phonon. Even if the sublattice does not melt completely, there will be a substantial change in the frequency of these mode as the melting temperature is approached.

For instance, the softening of an optical mode was observed in $SrTiO_3$,[62] despite not being a complete FE (it is a quantum paraelectric).[63] However, the ferroelectric phase can be achieved by means of strain,[64] leading also to a high decrease in the thermal conductivity, as reported by Sarantopoulos *et al*.[64]

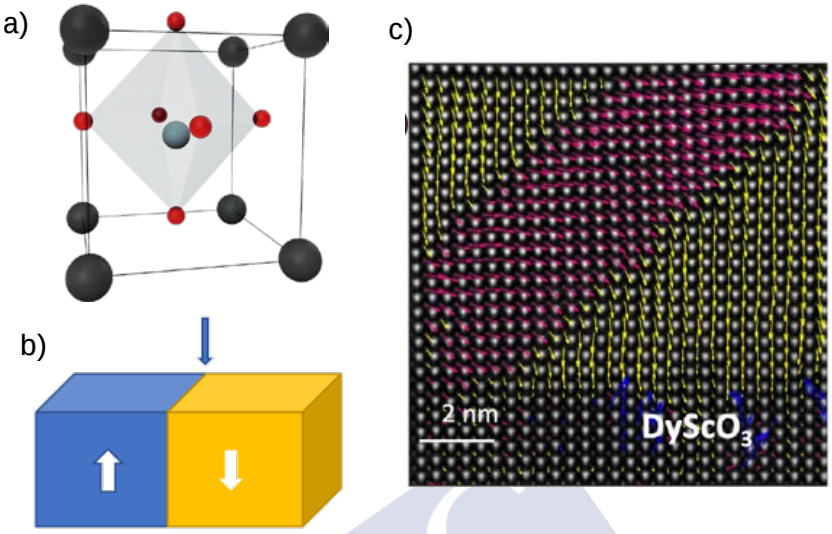


Figure 1.11. a) $PbTiO_3$ structure. Red, light grey and dark grey atoms are O, Ti and Pb, respectively. The displacement of the Ti atom with respect of the O octahedra can be clearly seen. b) Scheme of two domains separated by a 180º domain wall (marked by the blue arrow) c) HRTEM image of a 90º domain wall in a $PbTiO_3$ thin film on top of $DyScO_3$. (Reprinted with permission from* Nano Lett. *2019, 19, 11, 7901−7907. Copyright 2021 American Chemical Society.) The arrows represent the atomic scale polarization from the Ti displacement. It can be seen how the polarization goes from pointing down on the top-left corner, to then to the right and again to the left. Each of these changes in direction correspond to a domain wall.[65]

Just as in ferromagnetic materials, the electric dipoles arrange in different directions throughout a material, forming domains, which are separated by domain walls (DWs) (Figure 1.11 b and c). DWs are typically a few unit cells long, through which the change in polarization is gradual,[65–68] and have been thoroughly studied for the possible applications they may enable.[69,70] These DWs are also ferroelastic in some cases. Ferroelastic materials are those that present a spontaneous strain, which can be modified by the application of a stress. Hence,

ferroelectric-ferroelastic DWs can move across the material,[71–73] and can be modified at will with an external electric field,[68] applying a load, or through epitaxial tension.[74] Since the DWs are a boundary between two distinct parts of a material in which the structure is slightly different, they could be a source of phonon scattering in ferroelectric-ferroelastic materials.

The use of DW movement and reconfiguration by external fields is being thoroughly studied to achieve a thermal transistor. Theoretically, special interest has been shown by the group of Prof. Jorge Íñiguez, Dr. Riccardo Rurali and collaborators.[75–78] In particular they showed how DWs introduce a resistance to the phonon transport, which is not equal for all phonon frequencies; as well as how electric fields and strain affect the thermal conductivity in $PbTiO_3$. This results will be further discussed in Chapter 5.

On the other hand, within a single domain, the nature of the ferroelectric distorsion in $PbTiO_3$ causes an anisotropy in the thermal conductivity:[77] the difference in the structure along the direction of the displacement or perpendicular to it causes the thermal conductivity to be different in both directions. Furthermore, it can also be modified by strain imposed by a substrate when the material is deposited as a thin film.

Regarding experimental results, Foley *et al.*[79] achieved a reproducible switching of the thermal conductivity of a polycrystalline

free-standing PZT (lead zirconate titanate, $PbZr_xTi_{1-x}O_3$) thin film between 1.65 and 1.4 W/mK, through the application of an electric field across it. This result is in accordance with previous experimental[80–82] and theoretical results,[75–78,83] according to which the thermal conductivity would be increased by eliminating DWs through the application of an electric field.

However, previous findings from the same group,[84] showed a decrease of the thermal conductivity by 11% in a PZT thin film under the effect of an electric field.

They suggested that an increase (decrease)of the DW density after the application of an external field, in the case of the film (free-standing film).[79]

Very importantly, these authors did not take into consideration the crucial role that point defects (or grain boundaries in polycrystalline films) may be playing for the correct interpretation of the results.[31,79,84–87] Phonon scattering by atomic imperfections may be an important source of thermal resistance and may also act as pinning centers for DWs, reducing the effect of an electric field over their normal movement. In chapters 4 and 5 of this thesis the effect of atomic defects and grain boundaries in the thermal conductivity of ferroelectric $BaTiO_3$ and $PbTiO_3$ will be carefully analyzed.

2. EXPERIMENTAL TECHNIQUES

The work performed in this thesis is focused on the thermal characterization of thin films. The method for the fabrication of the films and some specific characterization techniques relevant to them will be explained in the dedicated chapter. However, the main techniques used in all the chapters, namely X-ray based techniques, and thermal conductivity measurements using the 3ω method will be explained, briefly, in this chapter.

2.1. X-RAY METHODS

In the growth of thin films, their crystalline structure and quality are of paramount importance. Some of the most widespread techniques used to study them are based on X-ray diffraction and reflectometry, and an explanation of the ones used in this thesis will be hereby given.[88]

All the measurements presented in this thesis were performed with a PANalytical Empyrean 4 circle diffractometer, equipped with a PIXCel^{3D} detector and a Ge (220) double bounce monochromator, schematized in Figure 2.1. It uses a copper source; therefore, the

wavelength of the radiation is 1.540598 Å (Cu $K_{\alpha 1}$). The monochromator allows to measure very thin peaks, by eliminating the $K_{\alpha 2}$ wavelength coming from the Cu source, and it can also be trimmed by slits as thin as 1/32 of a degree.

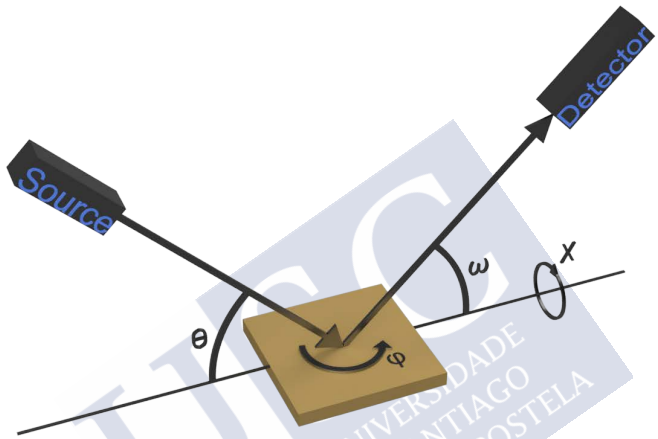


Figure 2.1. Schematic of the angles accessible in the diffractometer used in this thesis.

The X-ray based techniques used in this work are mainly X-ray diffraction (measurements in which θ=ω), X-ray reflectometry (in which θ=ω is also kept, but performed at very low angles) and reciprocal space mapping (in which both θ and ω are changed around a certain peak to explore a surface of the Ewald sphere[89]).

X-ray diffraction (XRD) is widely used to obtain information about the crystalline structure of all kinds of materials, from metal oxides to biological components, like proteins.[90] The interaction between radiation and a crystalline material, characterized by a

periodical order of planes of atoms with a certain separation between them (interplanar spacing, d) leads to constructive interference at certain angles θ, defined by Bragg's law. This is dependent on the wavelength λ of the radiation used, which must be in the scale of d.

In the case of a thin film, the lattice parameter can be calculated using Brag's law from usual θ/2θ diffractograms. Since in this work the substrates are oriented in the (001) direction, the lattice parameter obtained is the out-of-plane one, as the symmetric θ=ω geometry only permits to fulfill Bragg's law for horizontal planes.

There will be different kinds of films in this thesis, from polycrystalline, to epitaxial multilayers, and they do not have the same requirements, as the width of the peaks may require optics with higher resolution to be able to observe them clearly. For polycrystalline films wide peaks will be obtained, while for multilayers several interference peaks arise (Figure 2.2). The widening in polycrystalline films is caused by the slightly different orientations of the grains present in them, while epitaxial films that keep the structure of the substrate in plane do not exhibit this widening. This difference implies the need for high-resolution equipment, so that the peaks can be individually resolved.

An example of the pattern that arises in multilayers can be seen in Figure 2.2 a). This superlattice is formed by 8 repetitions of the pair $SrTiO_3/LaCoO_3$, with 5 nm of thickness in each layer (nominal period 10 nm). The X-ray beam reflects on the different interfaces of the

multilayer, giving rise to constructive interferences at some angles that are related to the thickness of each layer:

$$t = \frac{\lambda m}{2(sin(\theta_m) - sin(\theta))} \quad \textbf{(2.1)}$$

Where t is the thickness of the repeating unit in the superlattice, λ the wavelength, m the order of the peak (at position θ_m) in respect to the center one, which appears at the position θ.

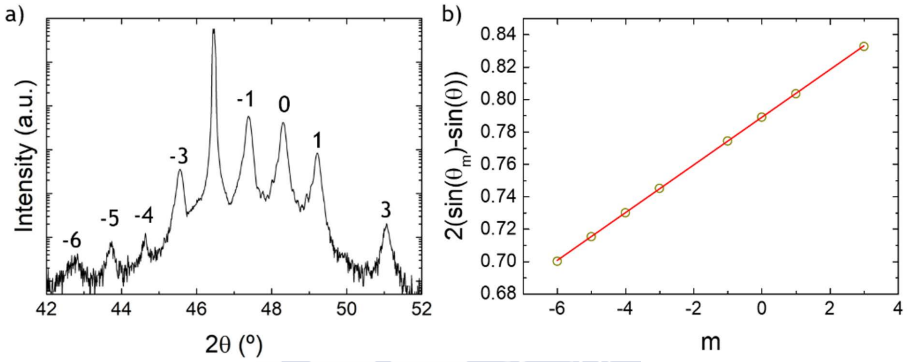


Figure 2.2. a) XRD pattern for a $SrTiO_3/LaCoO_3$ superlattice with 8 repetitions of the pair, with a thickness of 10 nm for each repetition (total thickness 80 nm) deposited on $SrTiO_3$. The order of the peaks (m) is written on top of each peak, except for the substrate. b) Fit to equation (2.1) of the positions of the peaks in a). The resulting thickness is 10.4 nm.

For the case of the multilayer in Figure 2.2 a) the period obtained is of 10.4 nm, close to the intended one of 10 nm (5 nm of each material). The fit to the equation can be seen in Figure 2.2 b): dividing the slope by the wavelength, the thickness of the period is obtained. In the case of a single layer, these peaks, called Laue fringes, are related to the thickness of the film that has the same structure, hence indicating a high crystalline quality.

Furthermore, XRD measurements of the superlattices can be simulated using CADEM software, written in Matlab by Komar and Jakob.[91] This program builds the material atomic plane by atomic plane, to then calculate its diffraction pattern using one dimensional kinematic diffraction theory. In summary, the code calculates the position of the peaks, using Bragg's law and an analog of equation (2.1). It also calculates the intensity of the different peaks, using the Lorentz, polarization, absorption, and structure factors.[88] For $LaCoO_3$ the relevant data was obtained from the literature,[92–95] as it was not already implemented in the code.

In perovskites (ABO_3), the unit cell is approximated by two different planes, of composition AO and BO_2, and the program takes it into account by using specific scattering factors for each atomic plane. Furthermore, it allows to add some intermixing of the materials to simulate the roughness of the interfaces, by modifying a chosen number of unit cells in which the scattering factors and lattice parameter are the average between the two materials. Two examples of the obtained pattern compared to the actual XRD data for two multilayers is shown in Figure 2.4. It can be seen how the positions of the peaks are accurately described by using the thickness of each layer obtained from X-ray reflectometry or transmission electron microscopy (TEM) when available, even though some peaks appear in the calculated pattern that do not appear in the real pattern or vice-versa. This may arise from different grains in the film that the program does not consider,

differences in the interfaces between the layers that are not being correctly accounted for or is not accounted for correctly in the intermixing, as reflected by Komar and Jakob.[91]

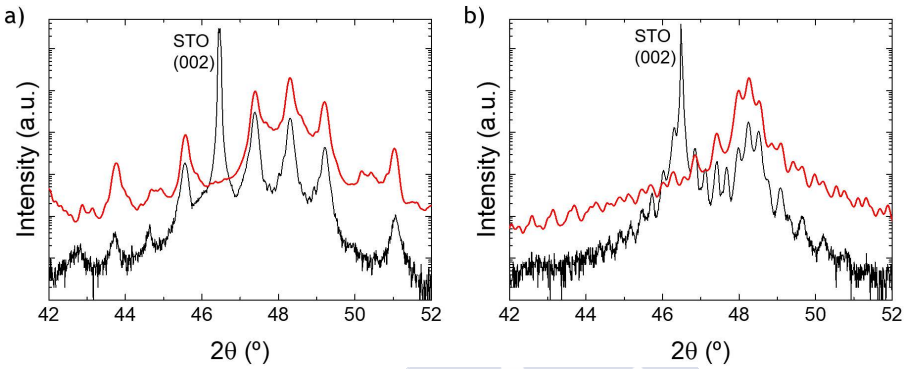


Figure 2.3. XRD patterns (black) and simulation using CADEM (red) for the $SrTiO_3/LaCoO_3$ superlattices formed by a) 8 repetitions of the pair with 5 nm of each material per repetition, and b) 3 repetitions of the pair with 15 nm of each material per repetition. The CADEM simulation is shifted upwards for clarity. The most intense peak in the real data corresponds to the substrate and is not included in the simulation.

X-ray Reflectometry (XRR) was used to measure the thickness, which is a particularly significative parameter in thin films. At low incident angles and with a θ/2θ configuration, X-rays are reflected both on the surface of the film and on the interface between film and substrate, leading to constructive and destructive interferences. This gives rise to a series of fringes, called Kiessig oscillations, the period of which is inversely proportional to the thickness of the layer:

$$\theta_m^2 = \theta_c^2 + \left(\frac{\lambda}{2t}\right)^2 m^2 \qquad \textbf{(2.2)}$$

Where m is the order of the peak and t is the thickness of the layer. This happens above a certain critical angle θ_c which depends on the density of the material; below the critical angle all the radiation is reflected. In the case of superlattices, the constructive interference can happen not only through the whole superlattice, but also between the different interfaces of the sample. If the internal interfaces are separated by an equal distance, there will be a series of maxima related to this thickness. These maxima give information about the superlattice period and can be related to an expression similar to the one for a single layer (Equation 2.2), exchanging the thickness of the layer for the period of the superlattice.

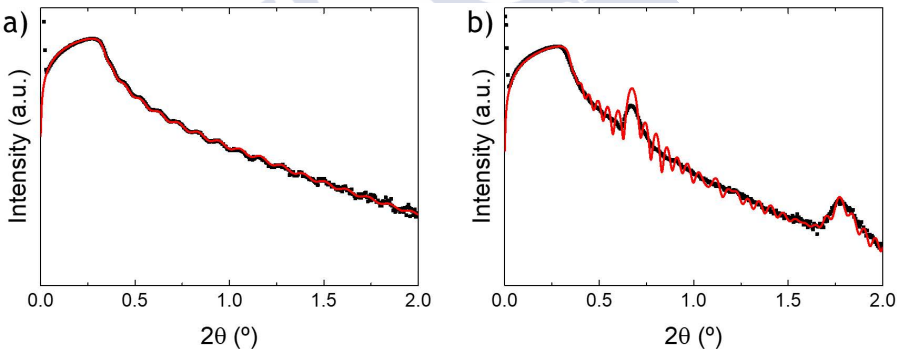


Figure 2.4. XRR measurement (black) and simulation using PANalytical software (red) of a) a 37.9 nm thick film of $BaTiO_3$ on top of $SrTiO_3$, with a surface roughness of 0.39 nm; and b) a $SrTiO_3/LaCoO_3$ multilayer, with an average thickness of 3.8(4) nm for each of the 20 layers.

These measurements also give information about the roughness of the interfaces: higher roughness decreases the intensity of the oscillations, in the same way as a rougher mirror would scatter light. The difference in refractive index of the two materials is essential,

because if they are too close there would not be any refraction between the two, so no oscillations would be observed. Different software is available for the treatment of this data, offering the possibility to run simulations, obtaining information about film thickness, surface and interface roughness, and film density. In this thesis X'Pert Reflectivity and AMASS, from PANalytical were used to fit the experimental XRR data.[96]

In Figure 2.4 the experimental data and simulation for two samples is presented. In the case of the superlattice the two main oscillations are far apart, since they are caused by a main shorter distance, the thickness of each of the layers.

Reciprocal Space Mapping (RSM) was used in this work to study the effect of epitaxial strain imposed by the substrate on the film. In this configuration, a certain asymmetric reflection of interest is studied by scanning the reciprocal space around it by changing both θ and ω. In this way it is possible to obtain information about the in-plane and out of plane lattice parameters of both substrate and film. From the positions of both angles mentioned the reciprocal space vectors can be calculated as:

$$Q_x = \frac{4\pi}{\lambda}\sin(\theta)\sin(\theta - \omega) \qquad \textbf{(2.3)}$$

$$Q_z = \frac{4\pi}{\lambda}\sin(\theta)\cos(\theta - \omega) \qquad \textbf{(2.4)}$$

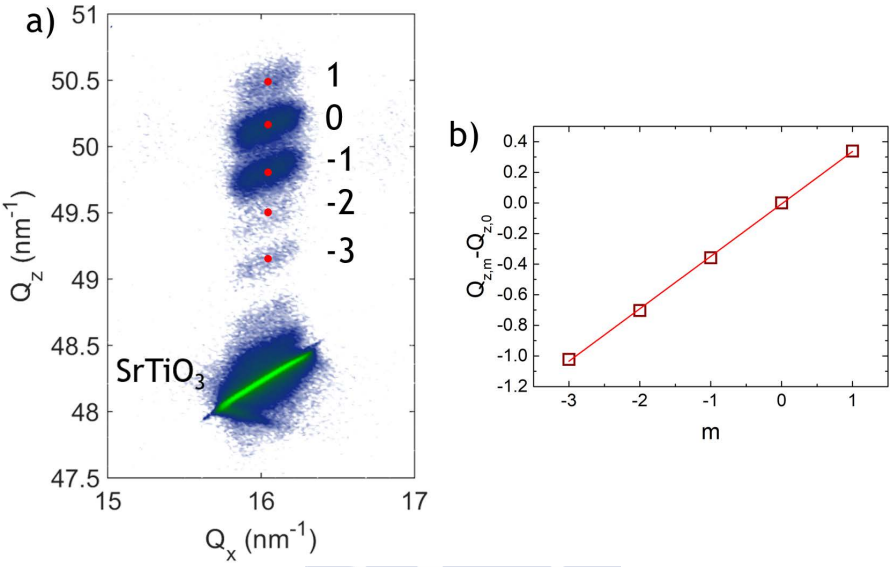


Figure 2.5. a) RSM around the (103) peak of $SrTiO_3$ of a $SrTiO_3/LaCoO_3$ superlattice with 5 repetitions of the pair, with a thickness of 16 nm for each repetition (total thickness 80 nm) deposited on $SrTiO_3$. The order of the peaks is given next to them, and the positions taken to calculate the thickness are marked with red dots b) Fit to equation (2.5) of the positions of the peaks in a). The average thickness of each layer obtained is 8.6 nm, close to the nominal 8 nm.

Reciprocal Space Maps allow to observe the strain state of the film: if the film is growing completely strained, the center of its peak in Q_x will be the same as for the substrate. If on the contrary it is different, a relaxation is taking place.

The superlattices will also exhibit multiple peaks in the reciprocal space maps (Figure 2.5 a), and they can be related to its period once again by using the position of the main peak, $Q_{z,0}$, and the secondary peaks of order m, $Q_{z,m}$:

$$t = \frac{2ml}{Q_{z,m} - Q_{z,0}} \quad \textbf{(2.5)}$$

where l is the Miller index of the (hkl) reflection that was measured.

Figure 2.5 b) shows the fit to equation (2.5) from the Q_z from the superlattice shown in Figure 2.5 a). The R^2 is 0.9995, showing that the peaks are well spaced, and this can be used to calculate the period thickness, which in this case is 17.2 nm.

2.2. THE 3ω METHOD

Thermal conductivity is the main interest of this thesis, and thus the **3ω method** is key in the whole project. This method was developed by Cahill[97,98] and it is based on the use of a resistor deposited on top of the sample to study, which acts, simultaneously, as a heater and a thermometer. An alternate current (of frequency ω) flows through it, leading to a temperature rise by Joule heating. The temperature distribution can be expressed as follows in cylindrical coordinates:[99]

$$\frac{1}{D}\frac{\partial T_{(r,T)}}{\partial t} - \left[\frac{1}{r}\frac{\partial}{\partial r}\left(r\frac{\partial T_{(r,T)}}{\partial r}\right) + \frac{1}{r^2}\frac{\partial^2 T_{(r,T)}}{\partial \theta^2} + \frac{\partial^2 T_{(r,T)}}{\partial z^2}\right] = \frac{q_{(t)}}{\kappa} \quad \textbf{(2.6)}$$

Where D and κ are the thermal diffusivity and conductivity, respectively. If the resistor is considered infinitely long and narrow, at a depth r ($l \gg r \gg w$, being l the length and w the width of the resistor) the heat propagation can be considered cylindrical. In this case the temperature function is independent of θ and z:

$$\frac{1}{D}\frac{\partial T_{(r,T)}}{\partial t} - \left[\frac{1}{r}\frac{\partial T_{(r,T)}}{\partial r} + \frac{\partial^2 T_{(r,T)}}{\partial \theta^2}\right] = \frac{q_{(t)}}{\kappa} \qquad \textbf{(2.7)}$$

The solution of this equation is proportional to the zeroth-order modified Bessel function K_0:

$$\Delta T_{(r)} = \frac{P}{\pi l \kappa} K_0\left(\frac{r}{\delta}\right) \qquad \textbf{(2.8)}$$

Where P is the power dissipated through the resistance and δ is the penetration depth of the temperature wave:

$$\delta = \sqrt{\frac{D}{2i\omega}} \qquad \textbf{(2.9)}$$

In the limit where $r \ll \delta$, the Bessel function can be approximated to:

$$K_0\left(\frac{r}{\delta}\right) \approx -\ln\left(\frac{r}{2\delta}\right) - \gamma \qquad \textbf{(2.10)}$$

Where γ is the Euler-Mascheroni constant. By introducing this approximation in equation (2.8), we arrive at the following expression for the temperature oscillation:

$$\Delta T_{(r)} \approx \frac{P}{\pi l \kappa}\left[\ln(2) - \gamma + \frac{1}{2}\left(\frac{D}{r^2}\right) - \frac{1}{2}\ln(2\omega) - \frac{i\pi}{4}\right] \qquad \textbf{(2.11)}$$

Which is the solution for an infinitely narrow line. But since the resistor has a finite width, it can be approximated as a convolution of many infinitely narrow lines along its width w. Using a normalized rectangle function:

$$f_{2(x)} = \frac{rect\left(\frac{x}{w}\right)}{w} \qquad \textbf{(2.12)}$$

To perform the convolution of this function and equation (2.8) it is convenient to move to the Fourier space, where the convolution of two functions is the product of their Fourier transforms. The Fourier transform of equation (2.8) is:

$$f_{1(k_x)} = \frac{P}{2\pi l\kappa}\int_0^\infty K_0\left(\frac{|x|}{\delta}\right)\cos(k_x x)\,dx =$$

$$\frac{P}{2\pi l\kappa}\int_0^\infty\left[\int_0^\infty \frac{\cos\left(\frac{|x|t'}{\delta}\right)}{\sqrt{t'^2+1}}dt'\right]\cos(k_x x)\,dx = \frac{P}{2\pi l\kappa\sqrt{\left(k_x^2+\left(\frac{1}{\delta}\right)^2\right)}} \qquad \textbf{(2.13)}$$

And the transform of equation (2.12) is:

$$f_{2(k_x)} = \int_0^\infty f_{2(x)}\cos(k_x x)\,dx = \frac{\sin\left(\frac{k_x w}{2}\right)}{k_x w/2} = sinc\left(\frac{k_x w}{2}\right) \textbf{(2.14)}$$

Applying the convolution of these two functions and making the inverse Fourier transform, the temperature distribution created by the strip is expressed as:

$$\Delta T_{(x)} = \frac{P}{2\pi l\kappa}\int_0^\infty \frac{sinc\left(\frac{k_x w}{2}\right)\cos(k_x x)}{\sqrt{\left(k_x^2+\left(\frac{1}{\delta}\right)^2\right)}}dk_x \qquad \textbf{(2.15)}$$

Averaging it the mean temperature measured by the resistor is obtained:

$$\Delta T = \frac{2}{w}\int_0^{w/2} \Delta T_{resistance(x)} dx = \frac{P}{\pi l \kappa}\int_0^{\infty} \frac{sinc^2\left(\frac{k_x w}{2}\right)}{\sqrt{\left(k_x^2+\left(\frac{1}{\delta}\right)^2\right)}} dk_x \qquad \textbf{(2.16)}$$

Even though the integral of this equation is unsolvable analytically, when the penetration depth is much smaller than the width of the resistor the $sinc$ function can be approximated to 1, and the upper limit of the integral can be reduced to the inverse of the half width of the resistor, leading to:

$$\Delta T \approx \frac{P}{\pi l \kappa}\int_0^{\frac{2}{w}} \frac{1}{\sqrt{\left(k_x^2+\left(\frac{1}{\delta}\right)^2\right)}} dk_x = \frac{P}{\pi l \kappa} ln\left[\sqrt{1+\left(\frac{2\delta}{w}\right)^2}+\frac{2\delta}{b}\right] \approx$$

$$\frac{P}{\pi l \kappa}\left[\frac{1}{2}\ln\left(\frac{4D}{w^2}\right)-\frac{1}{2}\ln(2\omega)+\ln(2)-\frac{i\pi}{4}\right] \qquad \textbf{(2.17)}$$

The only difference between equations (2.11) and (2.17) is the Euler-Mascheroni constant. Therefore, it is possible to express the solution of the temperature oscillations as a function of a constant η that will depend on the material.[100]

$$\Delta T \approx \frac{P}{\pi l \kappa}\left[\frac{1}{2}\ln\left(\frac{4D}{w^2}\right)-\frac{1}{2}\ln(2\omega)+\ln(2)+\eta-\frac{i\pi}{4}\right] \qquad \textbf{(2.18)}$$

Now the problem rests on the measurement of this temperature increase. If through any resistance flows an AC current of frequency ω, there will be self-heating by Joule effect at two times that frequency:

$$Q = I^2 R = \frac{I_0^2}{2}\sin^2(\omega t)\, R = \frac{I_0^2 R}{2}[1-\cos(2\omega t)] = P[1-\cos(2\omega t)] \qquad \textbf{(2.19)}$$

The constant component of the heat will lead to a rise in temperature that will stabilize ($\Delta T_{DC} = P/G$, being G the thermal conductance). The sinusoidal heating will depend on the apparent thermal conductance G_i that depends on the frequency and the geometry of the resistor, and can be out of phase from the heating wave:

$$\Delta T_{2\omega} = \Delta T_{2\omega,x} + i\Delta T_{2\omega,y} = \frac{P}{G_i} \quad \textbf{(2.20)}$$

In total, once the DC component is stabilized, the heating will be:

$$\Delta T = \Delta T_{DC} + \Delta T_{2\omega} \cos(2\omega t + \phi) \quad \textbf{(2.21)}$$

With this change in temperature there will be associated a variation in the resistance at the same frequency, 2ω, as the resistance is not independent of temperature ($\mathrm{dR}/dT \neq 0$). Applying Ohm's law taking into account that the resistance has a component that is a function of 2ω and the current is a function of ω, the voltage will have a component at 3ω, which will be directly related to the heating of the resistor:

$$V = I_0 \sin(\omega t)\, R = I_0 \sin(\omega t)\left[R_0 + \frac{dR}{dT}\Delta T \cos(2\omega t + \phi)\right] =$$
$$I_0 R_0 \sin(\omega t) + I_0 \frac{dR}{dT}\frac{\Delta T}{2}\sin(\omega t + \phi) - I_0 \frac{dR}{dT}\frac{\Delta T}{2}\sin(3\omega t + \phi) \quad \textbf{(2.22)}$$

Showing that measuring the third harmonic of the voltage ($V_{3\omega}$) we have a measure of the heating of the sample, and therefore of its thermal conductance:

$$V_{3\omega} = \frac{I_0}{2}\frac{dR}{dT}\Delta T \quad \textbf{(2.23)}$$

Taking this into account, as well as equation (2.18), from the slope (m) of $V_{3\omega}/V_{1\omega}$vs $\ln(2\omega)$ the thermal conductivity can be calculated as:

$$\kappa = \frac{I_0^2}{4\pi l m}\frac{dR}{dT} \qquad \textbf{(2.24)}$$

In the case when there is a thin film between the resistor and the substrate a thermal resistance in series is added to the system. This is possible since the thin film's thickness is much smaller than the thermal penetration depth and its thermal conductivity, κ_{film}, is smaller than that of the substrate.[101] This leads to a frequency independent term in the heating, that has the form:

$$\Delta T_{film} = \frac{P \cdot t}{w \cdot l \cdot \kappa_{film}} \qquad \textbf{(2.25)}$$

Where t is the thickness of the film. This can be seen in Figure 2.6 b) where a measurement of both substrate and film + substrate is shown.

The setup used for the measurement of the thermal conductivity in this work is comprised by a Keithley 6100 AC current source, a Stanford Research Systems SR830 lock in amplifier, and a homemade circuit for the elimination of the voltage at the first harmonic. The sample is placed inside a closed cycle He cryostat, allowing to measure the thermal conductivity from low temperatures (10 K) up to ambient temperature. The circuit for the elimination of the voltage at the first harmonic is necessary since the voltage at the third harmonic is much smaller than the one at the first harmonic, typically around 3 orders of

magnitude. The lock-in amplifier only allows inputs up to 1V, which would lead to too small signals at the third harmonic, especially with substrates that have a higher thermal conductivity, which leads to a smaller signal.

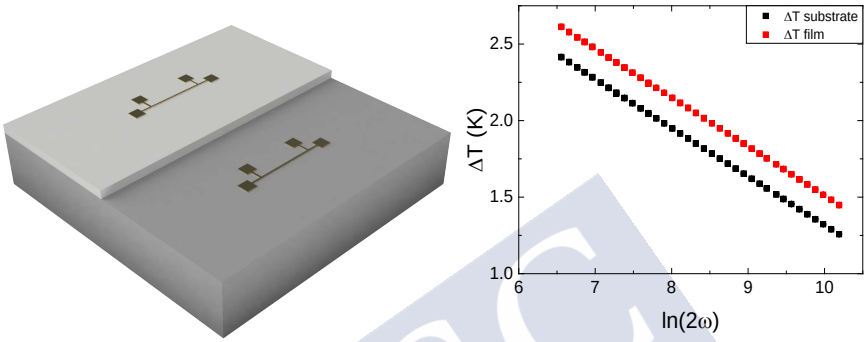


Figure 2.6. a) Schematic of the resistances deposited on the film and substrate. b) Measurement of the heating of a resistance deposited on top of an $SrTiO_3$ substrate (black) and another on top of a $BaTiO_3$ thin film deposited on the same substrate measured at 200 K. It can be seen they are parallel, so equation (2.25) is applicable to obtain the thermal conductivity in the film from the offset between the two.

The circuit designed (Figure 2.7) consists of three differential amplifiers and a set of resistors together with a variable resistor with PTC (positive temperature coefficient) approximately zero. One of the amplifiers is connected to the two terminals of the resistor on the sample between which the voltage must

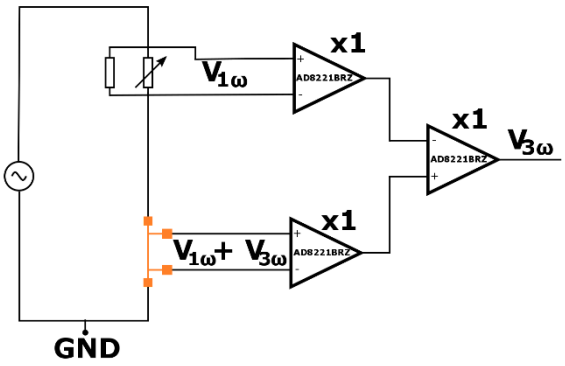


Figure 2.7. Scheme of the first harmonic cancellation circuit.

be measured (orange resistor in the scheme). A different amplifier, connected to the set of resistors and the variable resistor, will measure the voltage drop across them. Since the resistance of these elements does not change with temperature, they have no voltage at the third harmonic, related to temperature changes. Thus, when they are selected to be equal to the one in the sample, the voltage signal they have is equal to the first harmonic produced by the sample. This signal can be subtracted from the one from the resistor on the sample, leaving only the third harmonic voltage to measure, the one of interest.

The resistors deposited on the samples are comprised of 10 nm of Cr for adhesion and 100 nm of Pt or Au, with 1 mm of length between the center contacts and 10 μm wide. The deposition was done with a Gatan Precision Etching Coating System, which allows for the sequential use of various metals. It is equipped with a quartz crystal scale to measure the deposited thickness of the materials. The patterning of the resistors is made by a standard photolithography process and lift-off.

2.2.1. Analysis of the possible sources of error

There are a few considerations to be made when using this method. First, as said before, the thermal conductivity of the film and the substrate are required to be different enough, so that a thermal contrast can be measured. An example of the effect of the substrate thermal conductivity can be seen on Figure 2.8, where the measurement of an

80 nm thick film of $SrTiO_3$ deposited on the same material has no contrast with the substrate, even if the thermal conductivity of the film is expected to be lower than the substrate's, due to higher concentration of defects typical of thin films. However, when a film with the same thickness is deposited on top of magnesium oxide, which has a higher thermal conductivity, the thermal contrast is high enough so that the thermal conductivity of the film can be measured. For this reason the use of some substrates, for example LSAT, $(LaAlO_3)_{0.3}(Sr_2TaAlO_6)_{0.7}$, with a thermal conductivity of 4.8 W/mK[31], and rare earth scandates such as $GdScO_3$, that have a low thermal conductivity due to their high concentrations of defects, cannot be used in this project.

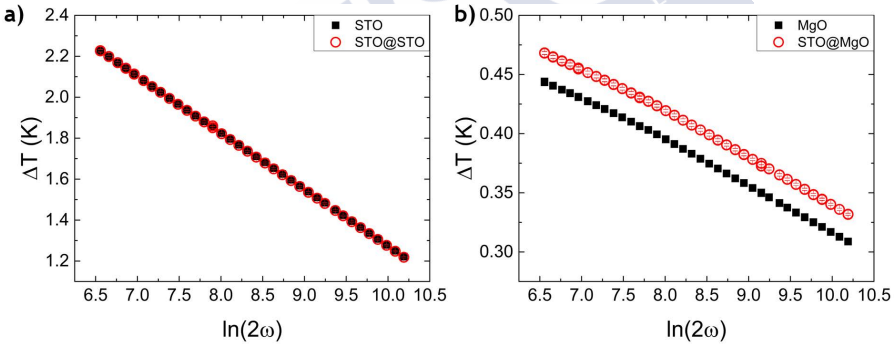


Figure 2.8. Temperature increase caused by dissipating 25 mW at 150 K on the bare substrate and on an 80 nm thick $SrTiO_3$ film deposited on: a) $SrTiO_3$ b) MgO.

Another important factor to consider is the influence of the power dissipated through the resistor. If the power used is too low, the signal would be too small, especially when using substrates with a high thermal conductivity, such as MgO. In fact, with substrates such as Al_2O_3, experiments becomes increasingly hard at low temperatures,

where it reaches thermal conductivities as high as 1000 w/mK.[102] The use of several powers may be useful to identify problems in certain samples. In Figure 2.9 the effect that power has in real measurements can be seen. $SrTiO_3$ has its thermal conductivity maximum at around 100 K, and using a low power has an impact on the measured value for the $PbTiO_3$ film, shown in Figure 2.9 a). However, when the thermal conductivity of the film is low, using an excessively high power may lead to overheating and an abnormally large thermal conductivity. This is what happens in Figure 2.9 a), where at low temperatures an increase in power causes a high increase in the value of κ measured.

It can also be seen that for the bilayer shown in Figure 2.9 b) lower powers may lead to an underestimation of the actual value of the thermal conductivity. The amplifiers used in the first harmonic cancellation circuit have limits to the input voltages, which leads to another limitation of the possible powers measured. In the case of the $BaTiO_3$ presented in Figure 2.9 b), the limitation of the amplifiers did not allow to use higher powers. In these cases, one must choose a value using also the dependence with temperature of the thermal conductivity of the film again, which in this cased showed that the value that best fitted the behavior of κ vs T was the one measured at 20 mW.

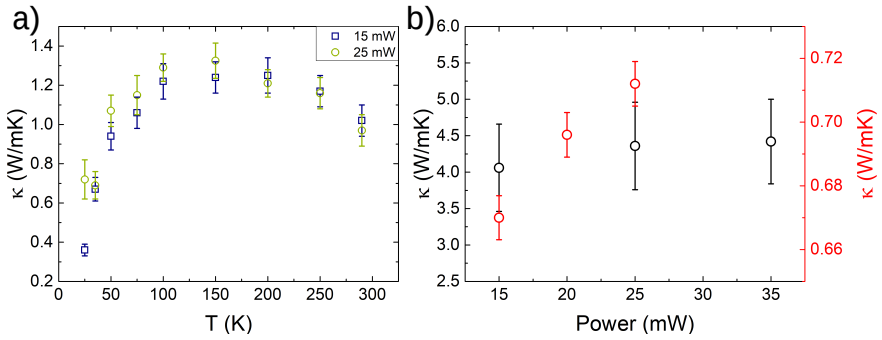


Figure 2.9. a) Thermal conductivity of a $PbTiO_3$ thin film grown on a $SrTiO_3$ substrate measured with 15 and 25 mW. b) Thermal conductivity of a $SrTiO_3$ and $LaCoO_3$ bilayer on top of a $SrTiO_3$ substrate at 150 K (left axis, black) and a $BaTiO_3$ film on a $SrTiO_3$ substrate at 300 K (right axis, red) as a function of the dissipated power on the resistance.

Therefore, measuring the thermal conductivity of thin films is not straight forward and one should place special care on the measurements themselves and the interpretation. In this work samples were usually measured with at least two powers in some of the temperatures to make sure that there was no dependence with power. In case that there was a change, more powers were used to obtain a correct value. All samples that are compared in the thesis are measured with the same power, to avoid differences caused by factors external to the samples themselves.

3. THERMAL CONDUCTIVITY OF $SrTiO_3/LaCoO_3$ SUPERLATTICES

3.1. OBJECTIVES OF THE CHAPTER, CONTEXT AND DISCUSSION OF PREVIOUS RESULTS

In this chapter I will discuss the results of the thermal conductivity of a set of multilayers composed of strontium titanate ($SrTiO_3$, STO) and lanthanum cobaltate ($LaCoO_3$, LCO), with different periodicities and total thickness. The goal of this part of my thesis was to study the contribution of coherent (wave-like) phonons and incoherent (particle-like) phonons, as the period of the superlattice, and the total superlattice thickness, changes.

As discussed in the introduction, in the framework of Boltzmann transport theory, the boundary effect is introduced in $\tau^{-1} = v/\phi$ (see equation (1.10) in the Debye approximation to the thermal conductivity). In this approximation, domains of size L impede the propagation of phonons of longer mean free paths, reducing the thermal conductivity. This is the situation found in thin-films and polycrystalline samples and superlattices (SLs).[103–107]

Consider a SL formed by the repetition of two different materials, with equal thickness, $L=L_1=L_2$, in which some heat is dissipated perpendicular to the interfaces.

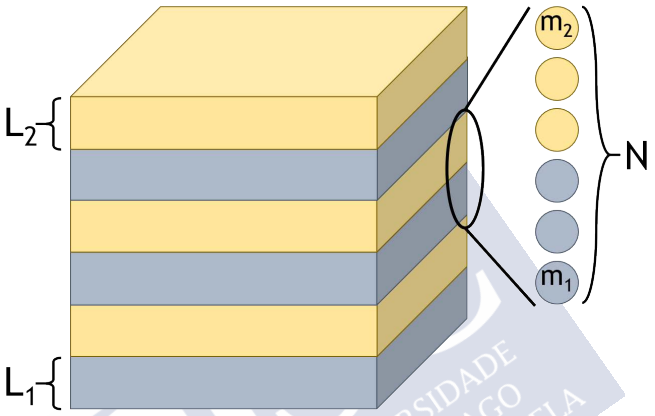


Figure 3.1. Scheme of a superlattice formed by two materials, with masses m_1 and m_2 and thickness L_1 and L_2. The periodicity is defined by the repetition unit N, in this case formed by 3+3 units (unit cells, atoms, etc) of each material.

In this case, the perpendicular thermal conductivity can be calculated from the (in series) thermal resistance of the two materials, plus the effect of the interfaces:

$$R_{SL} = \frac{2nL}{k_{SL}} = \frac{nL_1}{\kappa_1} + \frac{nL_2}{\kappa_2} + 2nR_i \qquad \textbf{(3.1)}$$

for n repetitions of L_1 and L_2. The interface thermal resistance, R_i, called "*Kaptiza* resistance", produces a discontinuous drop of temperature at the interface (see Figure 3.2). This can be modeled through a length, $L_k=R_i\kappa^0$, called "*Kaptiza* length", which is the

equivalent thickness of an interface with the bulk thermal conductivity κ^0, producing the same temperature change.

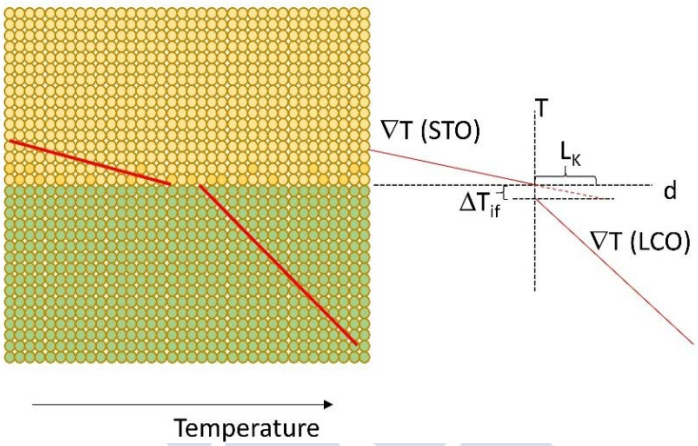


Figure 3.2. Scheme of the 1D temperature profile across an interface in a SL, under a heat flux. The thermal resistance of the interface, the Kapitza resistance, produces a temperature discontinuity at the boundary. The effect of the interface resistance can be modeled through the effect of an interface length, the Kaptiza length, L_K, as the product of the interfacial resistance and the intrinsic thermal conductivity of the bulk: $L_K = R_i \kappa^0$.

Following equation (3.1), increasing the interface density in a SLs (reducing L for the same total thickness) produces a continuous reduction of the thermal conductivity of the system.

On the other hand, when the phonon mean free path is larger than the domain size ($\lambda >> L$), phonons progressively become insensitive to these interfaces, and instead undergo multiple reflections at the surface of the sample, without losing phase coherence, forming new phonon bands due to interference effects.[108] In this wave-like or coherent

regime, band folding reduces the phonon velocity and forbids the propagation of certain phonon frequencies.[50]

Simkin and Mahan,[14] calculated the phonon dispersion of a SL, which is approximated as an atomic chain of N atoms with different masses: N/2 of m_1 and N/2 of m_2, representing the different layers, with identical spring constants. The phonon band dispersion for the SL can be calculated using the following equation:

$$cos(kN) = cos\left(\frac{k_1 N}{2}\right) cos\left(\frac{k_2 N}{2}\right) - \frac{1-cos(k_1)\,cos(k_2)}{sin(k_1)\,sin(k_2)} sin\left(\frac{k_1 N}{2}\right) sin\left(\frac{k_2 N}{2}\right) \quad \textbf{(3.2)}$$

Where $\cos(k_1) = 1 - \omega^2/2$ and $\cos(k_2) = 1 - \omega^2/(2\alpha)$, and $\alpha = m_2/m_1$ is the mass ratio.

We have simulated the phonon band structure for multilayers of STO and other oxides, using this approximation (equation 3.2). The results, Figure 3.3, show how increasing N increases band-folding, and reduces the average phonon velocity. Note that the thermal conductivity for a constant mean free path is proportional to the range of frequencies out of the gap: $\kappa \propto \frac{k_B l}{2\pi}(\omega_{max} - gap)$. So, the final result is a κ decreasing as L increases, at least as long as the layer thickness is shorter than the phonon mean free path. Beyond this limit, the particle model should apply.

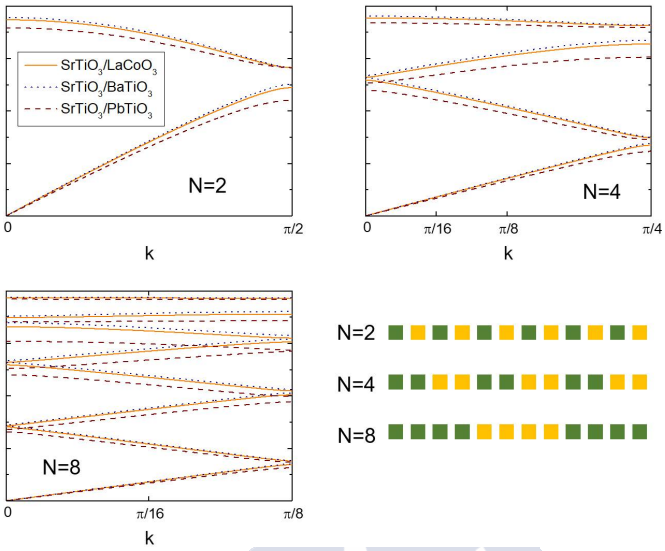


Figure 3.3. Phonon band structure calculated using the Simkin and Mahan model using the average mass per atom for different superlattices using $SrTiO_3$ and other oxide (shown) for N=2, 4, and 8. The equations from the paper by Simkin and Mahan were implemented in a Matlab code.

Thus, there should be a minimum in the cross-plane thermal conductivity of the SLs, as the wave interference effects decrease, and diffusive thermal transport of small wavelength phonons (equation 3.1) becomes dominant (see Figure 3.4).

The observation of this effect requires a large acoustic mismatch between both materials in the SL. However, a calculation of the effect of the average atomic mass of the layers, α, (Figure 3.5), shows that a larger mass difference leads to larger gaps in the phonon dispersion, which also produces a lower thermal conductivity. Thus, although a larger acoustic mismatch may reduce the number of periods needed to

observe the minimum, the increase of κ at small layer thickness may lead to a very shallow minimum, difficult to observe.

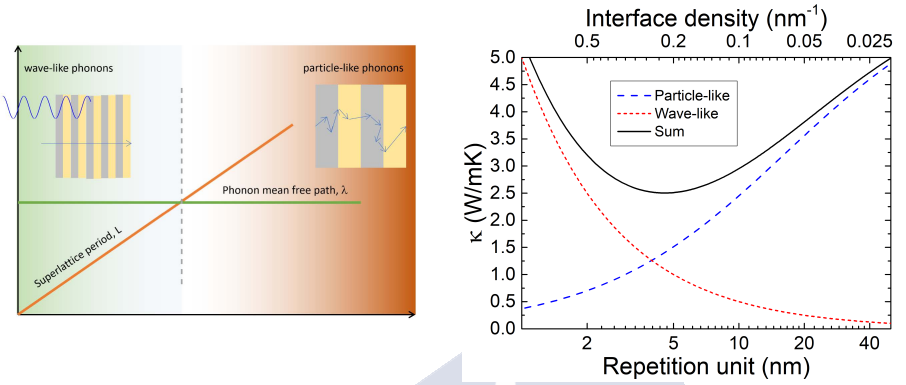


Figure 3.4. (Left) Schematic representation of the crossover between wave and particle-like phonon regimes in a SL, according to the model by Simkin and Mahan. As discussed in the text, there is a crossover between both regimes when the phonon mean free path is comparable to the superlattice period. Above (below) that point, incoherent (coherent) particle-like (wave-like) phonons dominate the thermal conductivity of the SL, manifested as a minimum in k(L). (Right) Thermal conductivity versus superlattice period for particle model, wave model, and a sum of both, which shows a minimum.

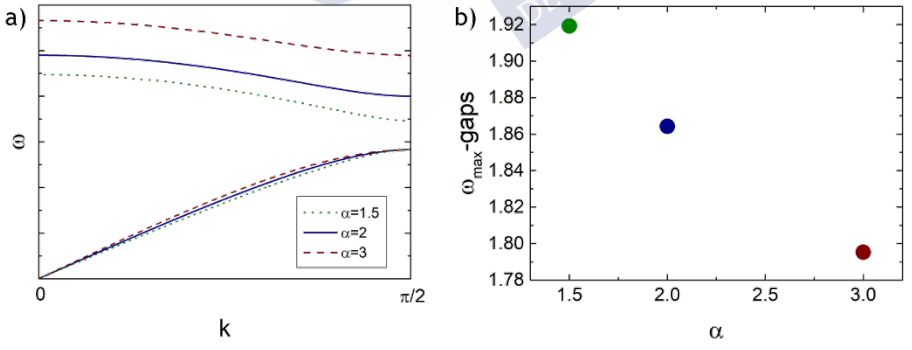


Figure 3.5. a) Phonon bands for three SLs with α=1.5, 2, 3 and N=2. b) $\omega_{max} - gaps$ for the three cases, showing that a higher mass difference leads to a smaller range of phonons available.

From the experimental point of view, a minimum at κ(L) was reported by Chakraborty *et al*.[109] in Si-Ge SLs at L≈ 7 nm.

Venkatasubramanian[110] also observed a similar behavior in Bi_2Te_3/Sb_2Te_3 superlattices (κ minimum at L≈ 5 nm). This is, in principle, surprising, given the short λ≈1 nm calculated for Bi_2Te_3.[111] Other results in similar SLs found no evidence of the minimum at κ(L), casting doubts on the intrinsic nature of this result.[112] For instance, Cheaito *et al*,[113] did not observe the minimum κ(L), despite λ>100 nm in GaAs/AlAs.[114] Instead, they observed a continuous decrease of the thermal conductivity as L decreases.

Regarding oxide multilayers, a very shallow minimum at L=2-3 nm was reported by Ravichandran *et al.*[12] in SLs of $SrTiO_3/CaTiO_3$ and $SrTiO_3/BaTiO_3$. The similar mass between $SrTiO_3$ and $CaTiO_3$ suggest that this may not be the optimum material combination choice. For the case of $BaTiO_3$, it is a ferroelectric material which could introduce extrinsic effects in the thermal conductivity, which could change with thickness.[115,116]

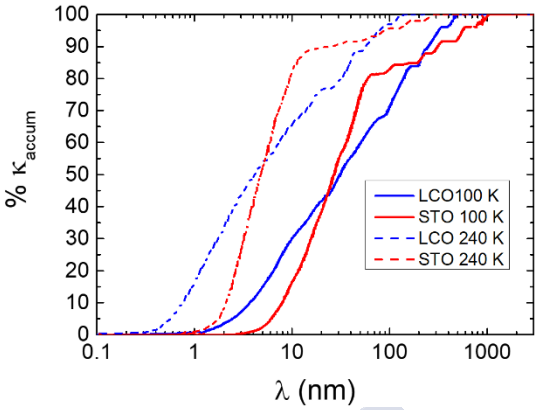


Figure 3.6. Cumulative thermal conductivity for $SrTiO_3$ and $LaCoO_3$, calculated ab initio. Data provided by A. O. Fumega. Details of the calculation can be found in Ref. [36]***.***

The calculated cumulative thermal conductivity of $SrTiO_3$ (Figure 3.6) shows that the mean free path of phonons that contribute most to the thermal conductivity, changes rapidly with temperature. Thus, a decrease of temperature must produce a marked increase in the depth of the minimum (as observed by these authors), and a marked increase of the position of the minimum in κ(L). However, this displacement was not reported in some of these articles. This, along with the only modest increase at very low L reported experimentally in oxide superlattices, suggests that this effect could be due to alloy-like formation, and not to the formation of coherent minibands.[113]

For instance, Katsufuyi *et al*. observed a linear increase of κ(L) in $SrTiO_3/SrVO_3$ SLs, from L≈4-100 nm.[117] Despite the similarities in structure and clean interfaces, no sign of κ(L) minimum or flattening is

observed at low L; instead, a constant interfacial resistance $\approx 2 \times 10^{-9}$ Km^2/W was observed in the whole range of repetition units.

On a different approach, Luckyanova *et al.*[114] measured the thermal conductivity of semiconductor SLs of GaAs/AlAs, changing the total thickness, *t*, but keeping the periodicity constant, at L=24 nm. In this case, if the thermal conductivity increases upon increasing the total thickness, it means that there are coherent phonons propagating through the whole SLs. On the other hand, if the thermal conductivity does not vary, it means that most of the thermal transport is done by incoherent phonons, which still have the same concentration of scattering points, as the interface density is constant.

These authors observed a linear increase of κ(T) with *t* at low temperatures, which is associated with coherent phonon propagation over a wide frequency range, across the internal interfaces of the SL. These results contradict an early study by Capinski *et al.*,[118] in which the thermal conductivity of the superlattices was found to be determined by the density of interfaces, irrespective of the total thickness. A subsequent article by Luckyanova *et al.*[119] in which they measured GaAs/AlAs SLs of L=6 nm, showed a much smaller κ than the superlattices with L=24 nm, for similar values of the total thickness. This suggests that a large portion of phonons contributing to κ(T) are effectively scattered by internal interfaces (incoherent phonons). Moreover, at low temperatures, the thermal conductivity of their SLs shows a maximum, due to phonon-wave localization.

Experiments by Cheaito *et al.*[113] on GaAs/AlAs SLs of different thickness and periods confirmed the contribution of both incoherent and coherent phonons.

Therefore, all these experiments suggests that there is indeed a fraction of phonons that behave as coherent waves, and another fraction that transport heat diffusively (particle-like), and that the ratio of both depends on temperature and other details of the SL.

In this chapter I report a systematic study of different $SrTiO_3$/$LaCoO_3$ (STO/LCO) SLs, varying the total thickness t, and the lattice period, L, as well as the periodicity of the structures. We analyze the possible presence of a minimum in $\kappa(L)$ and its meaning.

The choice of materials was based on having different enough masses and lattice constants, but that still grow well on top of each other, to have the best crystalline structure possible, and well-defined interfaces. Another factor considered for this choice was that the phonons that transport heat in both materials have similar mean free paths. The calculated cumulative thermal conductivity shown in Figure 3.6, shows that this is the case for STO and LCO. The difference in their lattice parameters is small enough, (d_{STO}=4.81 g/cm^3, a=3.905 Å; d_{LCO}=7.25 g/cm^3, a=3.80 Å), their average mass ratio m/atom(STO)=1; m/atom(LCO)=1.34, and acoustic impedance mismatch ≈ 1.1 (Z=dv,[120] where d is density and v velocity) make them a good system for this study.

Furthermore, calculations based in the model by Simkin and Mahan (Figure 3.3) show that band-folding effects are expected to be comparable or even slightly larger than in STO/BTO superlattices. Although calculations show that band-folding could be optimized for STO/$PbTiO_3$ superlattices, the ferroelectricity of the $PbTiO_3$ could introduce extrinsic effects over the thermal conductivity. Thus, $LaCoO_3$ and $SrTiO_3$ seem an optimal match for studying the contribution of coherent/incoherent phonon transport in oxide SLs. Finally, as will be discussed next, the magnetic character of strained LCO will offer important advantages to study the possible interdiffusion in oxide SLs.

3.2. Fabrication of the $SrTiO_3/LaCoO_3$ superlattices

The samples studied in this chapter were fabricated by Pulsed Laser Deposition (PLD),[121–123] in which a high energy pulsed laser impacts on a target of a certain material, placed inside a high vacuum chamber with a controlled atmosphere. The impact of the laser produces the ablation of the material, forming a plasma containing the atoms of the target material, which travel inside the chamber, and arrive at a substrate positioned in front of the target (10 cm away in our chamber). A scheme for the system can be seen in Figure 3.7.

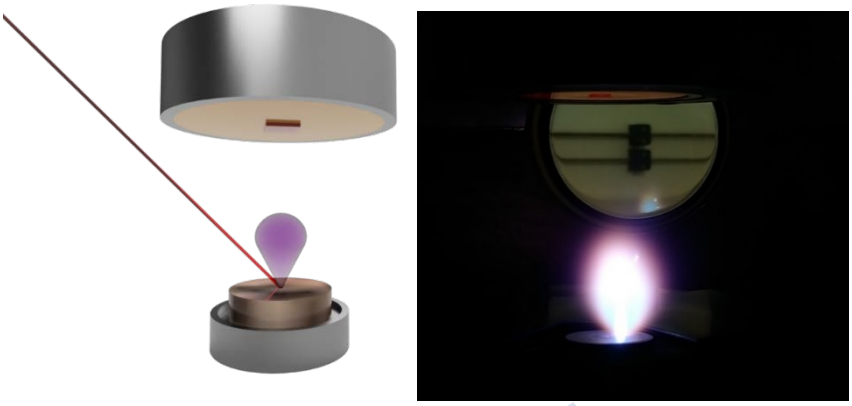


Figure 3.7. Schematic representation of the ablation process in the PLD chamber, and actual picture of the laser hitting a STO target. The ablation plume is directed towards the substrate, on top. The picture shows a reflection of the substrate on the view port of the chamber.

STO is one of the most studied and used perovskites for PLD growth, as its lattice parameter is suitable for the deposition of many other materials on top of it. Bulk STO has a cubic structure with lattice parameter 3.905 Å, and undergoes a phase transition to a tetragonal structure around 105 K.[124,125] Haeni *et al.*[126] used epitaxial stress to suppress this tetragonal distortion and stabilize a ferroelectric state below 270 K, driven by a soft-phonon instability.[127,128]. Other studies highlighted the critical role played by Sr^{2+} defects in stabilizing a relaxor-ferroelectric behavior in strained STO thin films.[129,130] The presence of domains with electrical polarization pointing along different directions could be an additional source of phonon scattering, particularly at the smaller thicknesses.[65]

On the other hand, many of the recent interest in this material has come from the 2D-electron gas that has been proposed to exist in the

interface between STO and $LaAlO_3$.[131] However, different studies suggest that the origin of this state could be linked to the formation of ionized oxygen vacancies in this material.[32,33,132] Thus, we have carefully optimized the deposition method to reduce as much as possible the presence of O^{2-} and Sr^{2+} vacancies in the STO films.

On the other hand, LCO is an orthorhombic perovskite at room temperature that can be deposited on STO, as its pseudocubic lattice parameter in bulk is 3.80 Å (2.6% strain).[133,134] Under this epitaxial tension, LCO develops a ferromagnetic order below 85 K,[135,136] which some authors linked also to the presence of oxygen vacancies.[137–139]

Thus, again, we have carefully optimized the deposition conditions to reduce as much as possible the presence of O^{2-} vacancies in LCO films.

As I will show now, it is possible to grow epitaxial LCO/STO superlattices with a very good crystallinity, and good interfaces, in a reproducible manner.

The laser used for the PLD growth is a frequency-quadrupled Nd:YAG laser with a wavelength of 266 nm and maximum energy of 100 mJ. In this case the energy of the laser to grow the LCO and STO films was ≈ 42 mJ (which, with the spot size in our setup gives a fluence of 2.3 J/cm^2). The substrate was kept at 725°C during deposition, and with an oxygen pressure of 200 mTorr. After deposition, the samples were cooled at 5°C/min in the same atmosphere. The growth rate (calibrated via ex-situ X-ray reflectivity analysis, for each material)

with these conditions was 0.024 Å/pulse for STO and 0.027 Å/pulse for LCO. During deposition, an STO or LCO target was impacted by the laser alternatively, to obtain the desired number of layers for the different samples. The SLs were deposited on (001)-oriented $SrTiO_3$ single crystals, used as received. The first layer of the SLs was always LCO, and the top layer was always STO.

Next, we had to decide the best range of thicknesses to be grown. For that, we made a first approximation to the effect of the different scattering mechanisms, considering their contribution to the Debye model using equations (1.7)-(1.10) as detailed in the introduction.

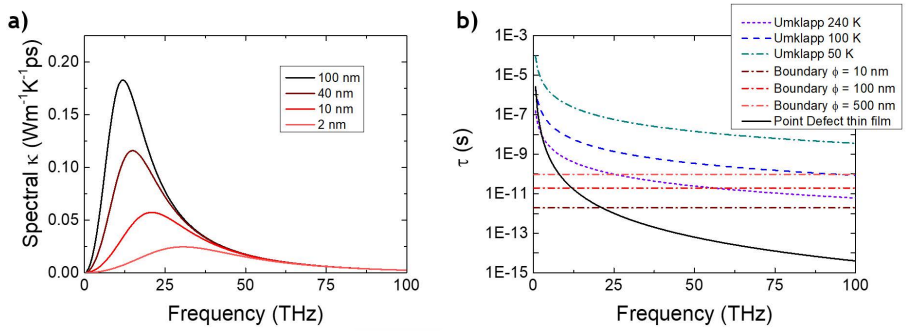


Figure 3.8. a) Spectral thermal conductivity calculated through the Debye model for LCO film at 100 K with different thicknesses (indicated). b) Relaxation times for different scattering mechanisms considered in the Debye model (eq. 1.7).

The spectral thermal conductivity, that is, the contribution of different phonon frequencies to the total thermal conductivity, can be obtained from the integrand of the Debye thermal conductivity (equation 1.7). We fitted κ(T) to the Debye model of the thermal conductivity of a sample of 80 nm deposited on top of STO, and the Umklapp and boundary scattering were calculated with data from the

literature.[140] The results of the calculated spectral contribution to κ for LCO (very similar for STO) are shown in Figure 3.8. The calculation shows that the reduction of the film thickness produces an important suppression of the low frequency phonons, below ≈35 THz. This effect is particularly appreciable below 10 nm.

Table 3.1. List of samples fabricated for this study, the thickness of each layer forming the SLs and the total thickness are indicated.

Sample name	Layer thickness L (nm)	Total SL thickness t (nm)
(2×40)	2	80
(4×20)	4	80
(4×40)	4	160
(5×16)	5	80
(5×24)	5	120
(8×10)	8	80
(10×8)	10	80
(10×10)	10	100
(15×6)	15	90
(15×6):ap	13-17 aperiodic	107
(20×4)	20	80
(20×6)	20	120
(40×2)	40	80

From the inspection of the relaxation time calculated for the different contributions to phonon scattering (Figure 3.8 b), it can be concluded that boundary scattering dominates the low frequency phonon spectrum for thicknesses below ≈10 nm in a wide frequency range. Thus, we have fabricated the samples with a total thickness of

from t=80-160 nm, and with a single layer repetition thickness of L=2-40 nm.

Under these premises, the samples prepared for this chapter are summarized in Table 3.1.

3.3. STRUCTURAL CHARACTERIZATION OF THE SUPERLATTICES

The samples were first characterized by XRR and XRD. Figure 3.9 shows the experimental XRR and the corresponding fitting, for various SLs. The simulation contains the main fringes in all SLs, which are determined by the thickness of the repeating unit, i.e. the period of the superlattice, using equation (2.2).

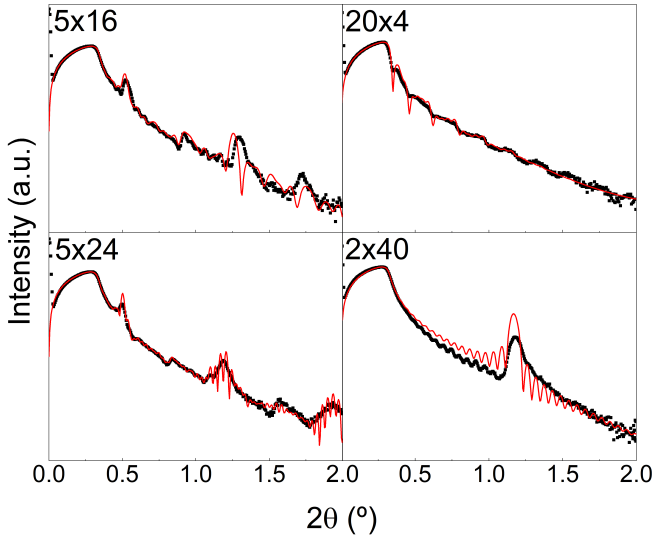


Figure 3.9. XRR data (black) and simulation using X'Pert Reflectivity (red) for the samples specified.

The average roughness obtained from the fittings was in the order of 0.8 nm for the thicker samples, and 0.3 nm for the thinner ones.

The SLs peaks are also observed around the main Bragg reflections of the oxides in their diffractograms. In Figure 3.10 I show the XRD patterns for the 80 nm thick SLs, with different periods, prepared for this work. The whole XRD pattern was fitted by the software CADEM[91]; the fitting parameters used were the thickness of the periods (using that obtained from XRR as an starting guess), the lattice parameters of STO and LCO, and the thickness of the interphase mixing layer. This parameter was kept at around 0.8 nm for the thicker samples, and at one unit cell in the thinnest ones, to be consistent with the roughness obtained from XRR. The result for one of the SLs is shown in Figure 3.10 b).

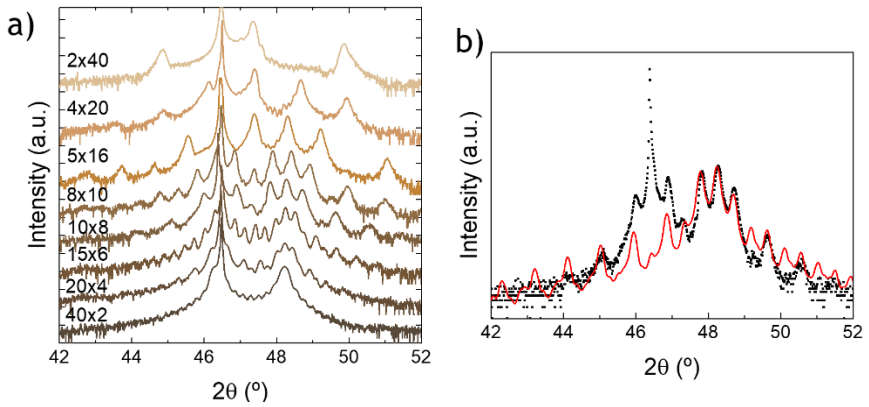


Figure 3.10. a) XRD pattern of the SLs around the (002) peak of the (001)-STO substrate. The total thickness of each SL is 80 nm; the periodicity is indicated. b) Experimental XRD pattern (black dots) and simulation using the CADEM code (red line), for the sample (10×8) SL.

Furthermore, the period thickness for each superlattice was obtained by fitting the peaks to equation (2.1). There is a very good agreement with the thickness obtained from XRR. The results for the samples (5x16) and (20x4) are shown in Figure 3.11.

RSM around the (103) peak for the different SLs (Figure 3.12) reveal the satellite peaks along the Q_z axis, which unequivocally confirms a periodic structure along the out-of-plane direction of the SL. As observed, the spacing between these satellites decreases as the number of layers in the SL decreases, i.e., the thickness of each layer, L, increases. The average layer spacing was thus calculated using equation (2.5).

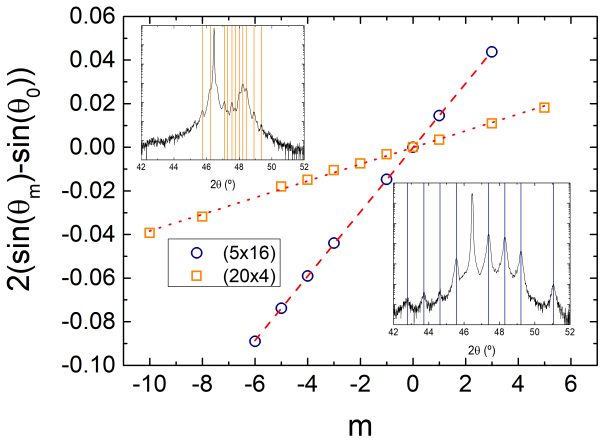


Figure 3.11. Fit to equation (2.1) of the positions of the maxima of the XRD patterns (marked in the insets) for the samples (5x16) (bottom right inset) and (20x4) (top left inset).

It is also important to observe that all the SLs are fully strained from the RSM data: the Q_x value is the same for all the peaks and coincident with that of the substrate, meaning that the in-plane lattice

parameter of the films in the superlattice is kept constant throughout the whole thickness and coincident with that of the substrate.

The information that can be obtained from the X-ray measurements is summed up in Table 3.2. The out of plane lattice parameter for the STO layer matches that of the bulk, as the peak appears overlapped by the substrate peak in the bilayer. In the case of the SLs the peaks are related to the superstructure and not directly to the lattice parameter of each layer. It is worth noting that the samples have a low roughness that increases slightly upon increasing the thickness of each layer.

Table 3.2. Data obtained from the analysis of the X-ray analysis of the samples.

Sample name	LCO Lattice parameter (Å)	Average thickness XRD (nm)	Average thickness XRR (nm)	Average rugosity XRR (nm)
(2x40)	3.78	1.9	1.96	0.54
(4x20)	3.77	3.8	3.84	0.82
(4x40)	3.77	3.8	3.90	0.51
(5x16)	3.772	5.45	5.26	0.73
(5x24)	3.77	5.7	5.6	0.9
(8x10)	3.772	9	7.82	1.1
(10x8)	3.78	10.5	10.4	0.74
(15x6)	3.772	17.5	15.2	1.4
(15x6):ap	3.769	*	14.6	1.4
(20x4)	3.771	20.9	21.5	1.3
(20x7)	3.771	19.6	19.5	1.5
(40x2)	3.771	40.2	46.1	0.95

**** The thickness for this sample cannot be obtained from XRD, as there is no periodicity.***

The thickness of each lattice in the SLs obtained through different X-ray techniques as well as from electron microscopy are summarized in Figure 3.13. The good correlation between the intended and nominal

period thickness demonstrates the accuracy of the ex-situ calibration of the growth rate.

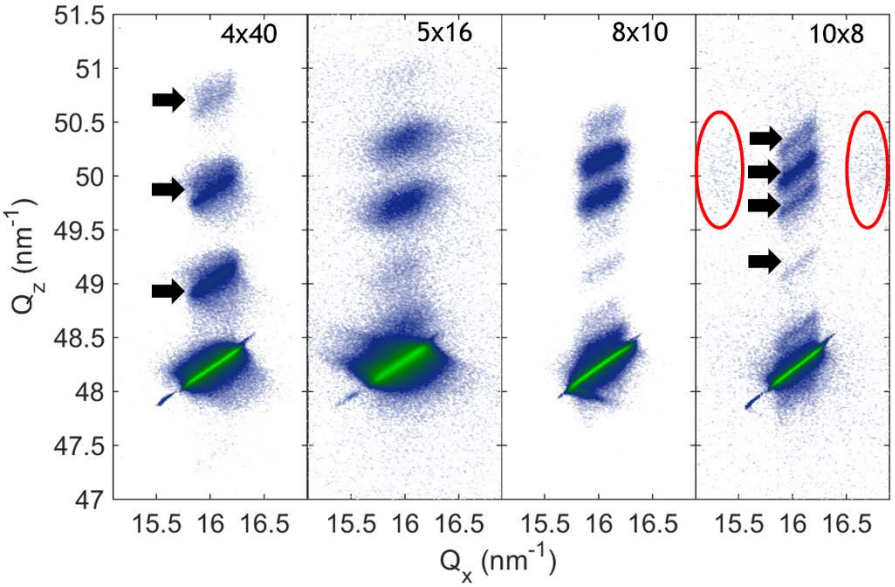


Figure 3.12. RSM around the (103) peak of STO for the indicated samples. The periodic peaks are marked with black arrows in samples (4x40) and (10x8).

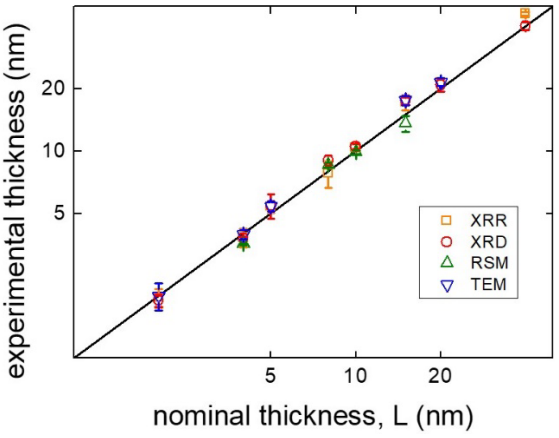


Figure 3.13. Thickness of each layer composing the SLs, obtained from different methods, versus the nominal thickness.

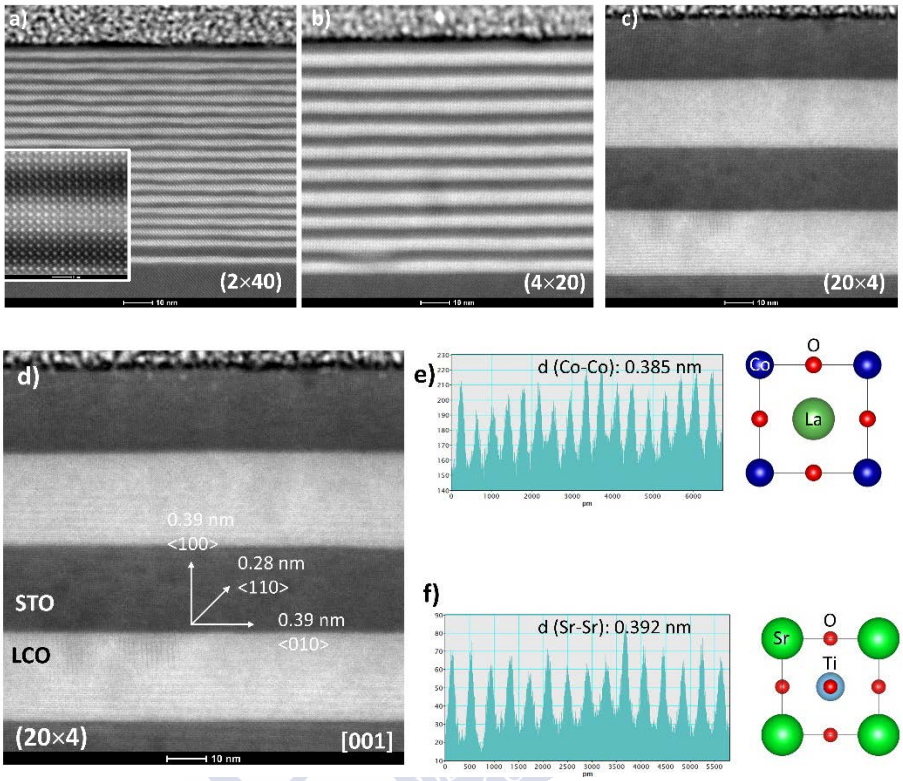


Figure 3.14. a-d) Cross section HAADF-STEM images of several SLs, with the period indicated on each panel. The scale (white bar) is 10 nm is every picture, except in the inset to a), which is 1nm. This inset is a higher-resolution image of the interfaces, showing the abrupt change between the layers, of about one unit cell. Panels e) and f) show the EDX-line scan analysis parallel to the plane of the sample, in a layer of LCO and STO, respectively. The size of the unit cell was obtained from this analysis.

The quality of the internal interfaces in the SL is a fundamental parameter for the intepretation of the results of the thermal conductivity. We have prepared several cross-section lamellae of our samples in order to check the quality of the interfaces by high resolution Electron Microscopy. We payed particular attention to the existence of atomic

interdifussion, imperfections associated to the layer growth, or any other factor that could influence the thermal conductivity of the SLs.

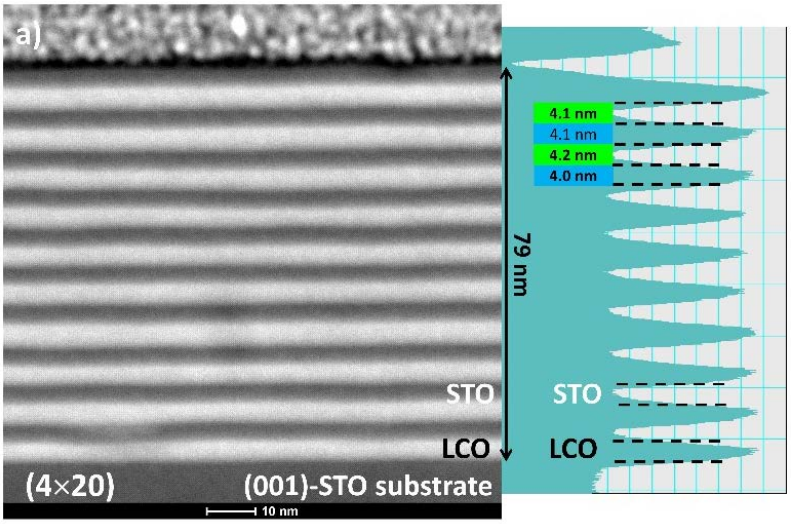


Figure 3.15. Cross section HAADF-STEM image of the (4×20) SL and EDX analysis, showing the regularity of the layer thickness. The total thickness of the SL is ≈79 nm, giving an average of 3.95 nm per layer, very close to the intended 4 nm per layer.

In Figures 3.14-3.16 the results of the electron microscopy analysis are sumarized. The pictures show several images of cross-section SLs obtained in HAADF-STEM (High Angle Annular Dark Field-Scanning Transmission Electron Microscopy) mode, and EDX analysis, both line-scans and elemental maps. The in-plane lattice parameters obtained from the EDX metal-metal distance are 3.92 Å for STO, and 3.85 Å for LCO, showing a partial relaxation of the eptiaxial tension in LCO.

The high resoluiton STEM show very well defined interfaces, with minium intermixing, as shown also in the EDX analysis of Figure 3.16. The width of the interfases, defined as the region where the intensity of

the EDX peaks decays at half its maximum value, is less than a nanometer, i.e. extends around a unit cell along each layer. From these data, we have not found any sign of increase intermixing or rugosity of the interfaces as the size of the layers changes.

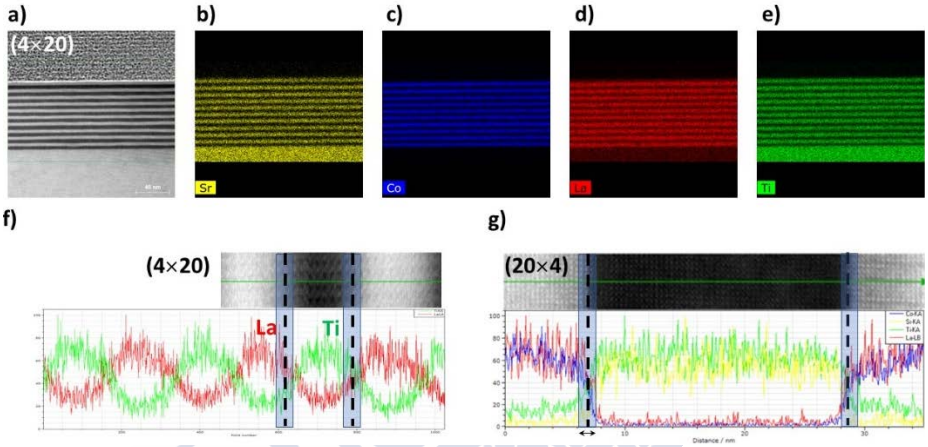


Figure 3.16. a-e) Elemental maps obtained from EDX analysis of a cross section lamella, in this case corresponding to the (4×20) SL. f) Line scan analysis at the La and Ti EDX lines of the (4×20) SL. g) Line scans of the cations in STO and LCO of the (20×4) SL.

Therefore, from the X-ray diffraction and high-resolution electron microscopy analysis we conclude that the LCO/STO SLs are of good crystallinity, and with clean enough interfaces as to perform the study of thermal transport detailed in the introduction of this chapter.

3.4. THERMAL CONDUCTIVITY OF THE SUPERLATTICES

The cross-plane κ(T) of the SLs was measured from 25 to 290 K by the 3ω method; the results are shown in Figure 3.17 for the SLs with total

thickness t≈80 nm. In all SLs, κ(T) first increases up to ≈150-200 K, before reaching a plateau, and then decrease slightly until room temperature.

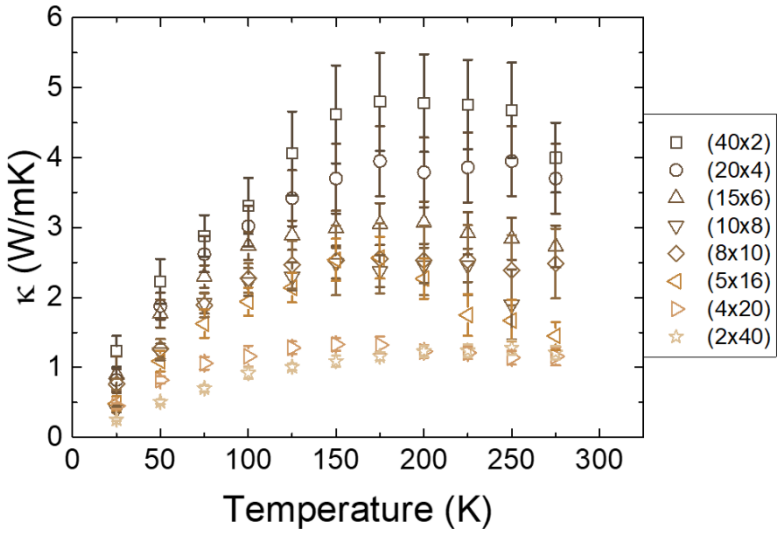


Figure 3.17. Temperature dependence of the thermal conductivity of the different SLs with t=80 nm (see Table 3.1).

The increase of interface density leads to a decrease on the thermal conductivity, although the trend is not monotonous. The accuracy of the measurement increases at lower temperatures, due to the increasing contrast with the substrate (the thermal conductivity of STO is maximum at around 100 K).[31] However, we wanted to avoid any possible influence of the structural distortion in STO, and the magnetism in LCO. Thus, in Figure 3.18 we present the cross-plane thermal conductivity at 150 K vs 2L (this behavior does not change much between 100-250 K).

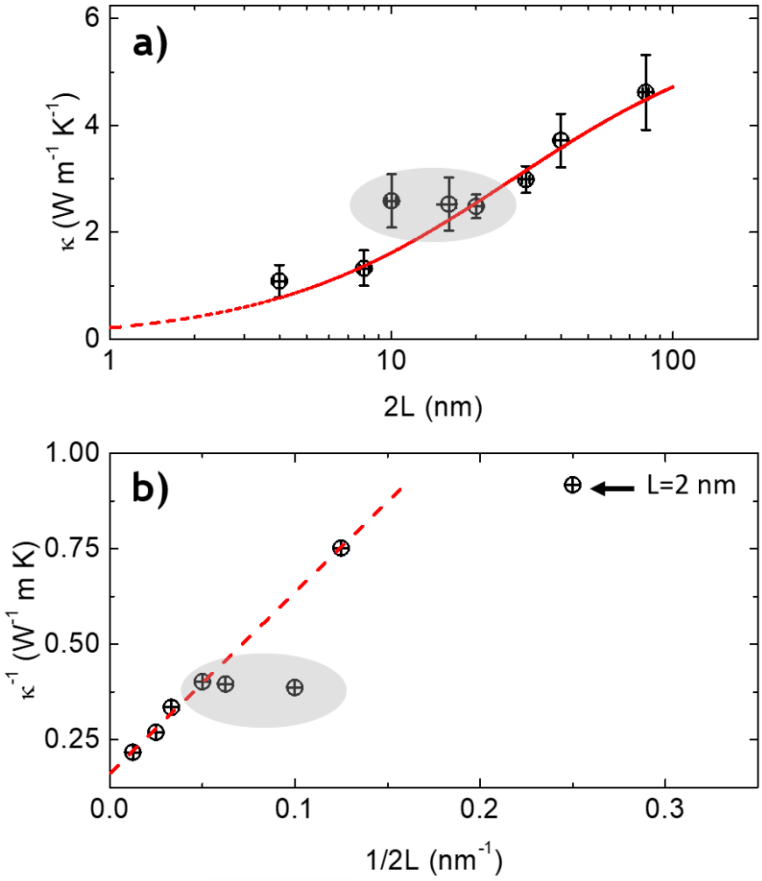


Figure 3.18. a) Dependence of the thermal conductivity of the SLs with the period, 2L, and the fitting to equation (3.1). The data in the shadowed region deviate from the general trend. b) Linearized version of equation (3.1), and linear fitting. The dots inside de grey region, as well as the L=2 (marked with an arrow), were excluded from the fitting.

As discussed before, phonons with $\lambda<2L$ behave like particles, being dispersed by the internal interfaces of the SL. Hence, the effect of the interface boundary resistance can be captured by a simple model incorporating the Kapitza resistance, R_i, into the Fourier's law of heat conduction across the SL:[103,104]

$$\frac{k}{k_0} = \frac{1}{1+\frac{2R_i k_0}{d}} \quad \textbf{(3.3)}$$

where κ_0 and R_i are the thermal conductivity of the bulk, free of interfaces, and the interfacial thermal resistance, respectively; the repetition unit is d (=2L in our notation). The inverse of this equation predicts a liner relationship between 1/κ and 1/d; however, as shown in (Figure 3.15 b), the data corresponding to L=10-5 nm, as well as the L=2 nm, deviate from this behavior. Excluding these points from the fitting, gives $\kappa_0 \approx 6.25(8)$ W m^{-1}K^{-1}, close to the average of STO and LCO at this temperature, and a Kapitza resistance $R_i \approx 4.7(2)\times10^{-9}$ W^{-1} m^{2}K, similar to other oxoperovskite artificial interfaces, grain boundaries or ferroelastic domain walls.[65,117,141]

From these results, the Kapitza length, $L_K = R_i\ \kappa_0 \approx 24$ nm, which becomes comparable, or even larger, to the period length for SLs with L ≤10 nm.

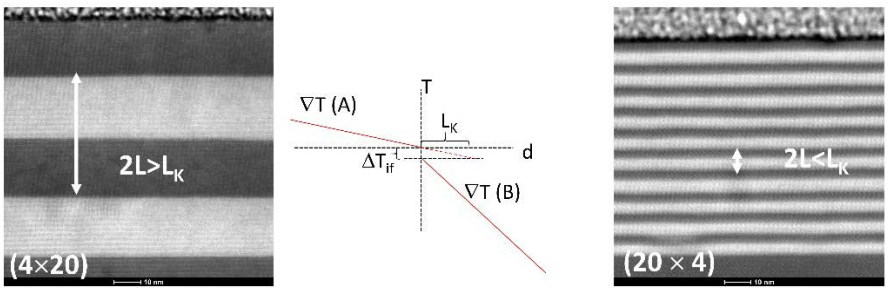


Figure 3.19. The meaning of the Kapitza length, L_K, and its relationship to the SL period, d=2L, in equation (3.1).

Below this limit of periodicity, the applicability of equation (3.3) to the SLs is difficult to justify. This could be the reason of the discrepancy between the experimental data below L=10 nm (d=20 nm) and the fitting, shown in Figure 3.18.

Instead, in this regime, most of the phonons will achieve the condition of $\lambda>2L$, so that they become less and less sensitive to the periodicity of the structure. In this case, a wave-like treatment is more appropriate and κ is determined by wave interference and boundary scattering at the external interfaces of the film.

An additional set of samples, with larger thickness of t=140-160 was synthesized, one with L=20 ($2L>L_K$), and another one with L=4 ($2L<L_K$). The results, in Figure 3.20, show that the relative variation of κ with t is similar in both SLs. That suggests that, irrespective of L, there is a portion of phonons whose mean free path is limited by the total thickness of the SL and must be better treated as coherent waves.

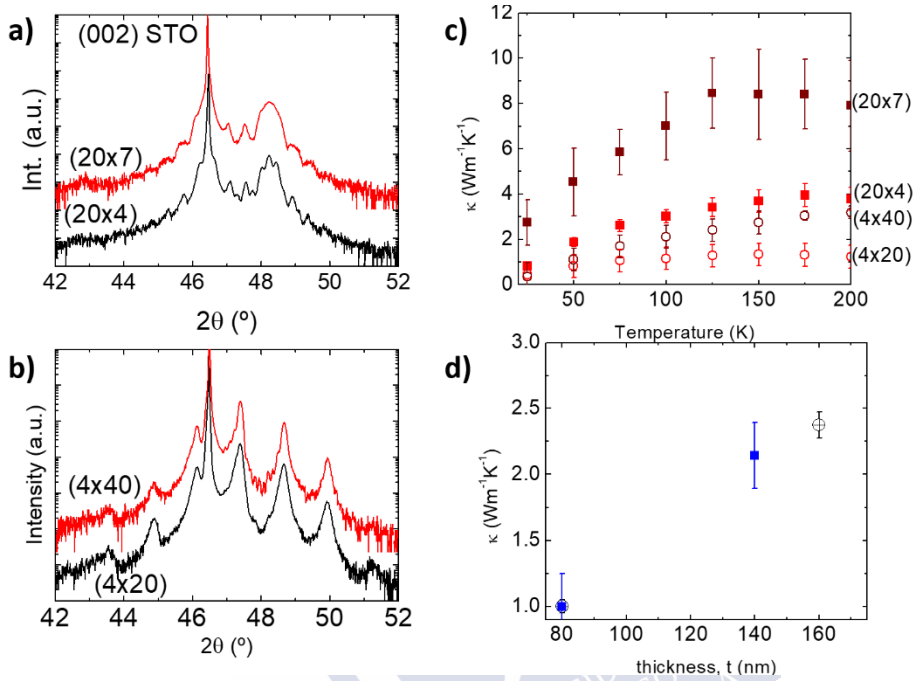


Figure 3.20. a), b) XRD of the SLs with L=20 and L=4, with different total thicknesses. The period of the SL is maintained, as demonstrated by the almost identical XRD patterns. c) Temperature dependence of the thermal conductivity for two sets of superlattices, with the same periodicity but different total thickness, t. d) the κ(150K) for the two SLs.

On the other hand, wave-like phonons should be very much affected by a change in the periodicity of the SL,[142,143] while particle-like phonons should remain insensitive to this, as long as L is larger than λ. Thus, to further investigate the contribution of coherent phonons in the SLs with L≥10 nm, we have performed the following experiments: we have synthesized a SL with 3 repetitions of (STO/LCO) of d=26, 32, and 29 nm. This sample is like a L=15 nm (d=30 nm) SL but introducing some intentional variation of the thickness of each layer, in order to affect the

periodicity of the SL. A cross section analysis of this aperiodic SL, (15×6):ap, is shown in Figure 3.21.

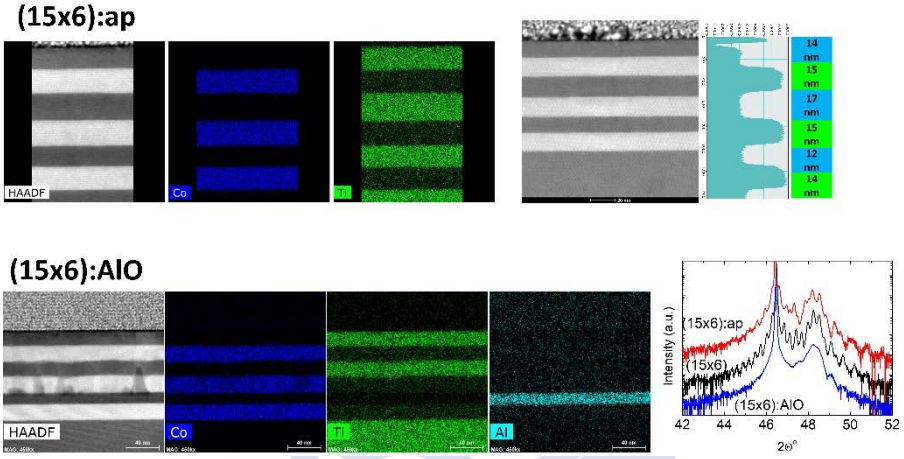


Figure 3.21. High resolution HAADF and EDX analysis of cross section lamellae of (15×6):ap and (15×6):AlO SLs. The XRD of both SLs, along with the normal (15×6) SL is shown in the bottom right panel. The loss of periodicity is clearly reflected in the disappearance of many of the SL peaks.

Another sample was fabricated with regular (15×6) distribution, but the first layer of STO was substituted by $Sr_3Al_2O_6$. This is an oxide with a lattice parameter of 15.84 Å, (≈4×STO), density 4.12 g/cm^3 (≈0.9×STO), and with a very similar lattice structure to STO, hence allowing epitaxial growth of several perovskite oxides on top of it.[144,145] The cross section analysis of this SL, (15×6):AlO, is also shown in Figure 3.21

The results of the thermal conductivity are shown in Figure 3.22: the alteration of periodicity reduces κ(150 K) by more than 30%. The spatial variation decreases the ratio of constructive to destructive

phonon interferences. The reduction is similar to the case of introducing a slightly different material in the middle of the SL.

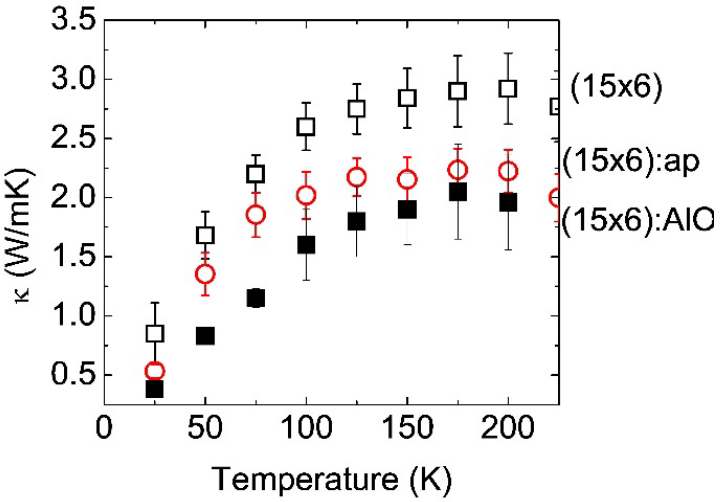


Figure 3.22. Temperature dependence of κ for several SL close to (15×6). Even a tiny loss of periodicity reduces the thermal conductivity very notably; see text for discussion.

Note that (15×6):ap is even slightly thicker than the regular (15×6). Thus, the reduction of κ achieved in the aperiodic SLs confirms the localization of coherent phonons also in the SLs with large period thickness (i.e. in the linear regime of equation (3.3); Figure 3.18 b). Similar reduction was reported in aperiodic structures SLs of semiconducting Si/Ge and GaAs/AlAs,[142,143] suggesting a general behavior in which both particle and wave-like coherent phonons contribute to the thermal conductivity of SLs, for all values of L.

What is thus the origin of the minimum observed in κ(L) by other authors? Or the nature of phonons in the SLs with thinner L, which deviate from the trend in Figure 3.18?

At a fixed temperature (150 K), the smaller the L, the larger the number of phonons fulfilling λ>L. But the fraction of coherent phonons, and hence their contribution to the thermal conductivity, will be also influenced by the rugosity of the interfaces, η. The condition λ>L is required for preserving phase over multiple wave reflections at several interfaces, but phonon wavelength, l, must be also larger than η, so that they undergo specular reflection. A specularity parameter, p, was defined by Ziman to account for the fraction of phonons that undergo specular reflection:[4]

$$p = e^{-16\pi^2\eta^2/l^2}$$

To give an idea of the relevance of rugosity, for STO, at low temperatures, l≈5-10 nm[36]; a root mean square rugosity of one unit cell η=0.3 nm results in p≈0.5-0.9. Thus, the relative contribution of coherent phonons to the thermal conductivity decreases not only as L increases, but also as η does.

Ju *et al.*[142] showed that Si/Ge interfaces with some interatomic mixing increase phonon transmission, and hence the thermal conductivity. Although longer-wavelength phonons are insensitive to the small length scale mixing at the interfaces, shorter wavelength phonons are. Their simulations show that interfaces with maximum

thermal conductance are formed by regions that are not atomically flat, but that interpenetrate each other.

Langenberg et al.[146] demonstrated that, below a critical thickness, the relaxation of epitaxial tensile train in $SrMnO_3$ is no longer determined by formation of dislocations and stacking, but by the spontaneous creation of atomic vacancies. This critical thickness can be calculated from the Matthews and Blakeslee equation, on the basis of a series of structural parameters of the film which can be measured experimentally.[147] Assuming similar parameters to STO (a perovskite oxide with similar Poisson ratio),[148] the critical thickness for LCO on STO is of $t_c \approx 4.5$ nm.

Thus, it is plausible that some interdiffusion occurs at the interface of the thinner layers, impacting the value of the rugosity and interfacial thermal resistance, R_i. Note that, rearranging equation (3.3)

$$\frac{1}{k} = \frac{1}{\kappa_0} + \frac{R_i}{L} \qquad \textbf{(3.4)}$$

Then, if R_i decreased as L does (at low L), more and more phonons could travel ballistically across the structure, increasing the thermal conductivity. This would result in a minimum at the thermal conductivity as a function of L.

Alternatively, this effect can be captured by defining a dimensionless parameter, x, which relates the rugosity and the thickness of each layer:

$$x = \frac{(1-\eta)}{L}$$

As more phonons will behave ballistically as x increases, the total thermal conductivity as a function of the periodicity, 2L, can be then obtained from the weighted fraction of coherent (ballistic) phonons, and incoherent phonons; following equation **(**3.3):

$$\frac{1}{\kappa} = x\frac{1}{\kappa_0} + (1-x)\left(\frac{1}{\kappa_0} + \frac{R_i}{L}\right) \quad \textbf{(3.5)}$$

Although this is a very crude approximation (note that it diverges at L→0), it gives an idea of the relevant parameters contributing to κ(L) of a SL. The κ(L) calculated for different values of the rugosity is shown in Figure 3.23.

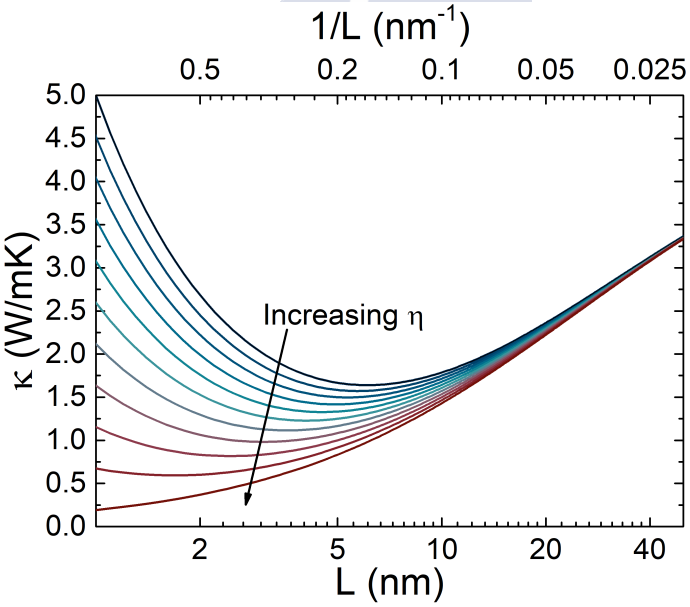


Figure 3.23. Representation of equation (3.5) using different rugosities from 0 to 1 nm. It can be seen how the minimum shifts to smaller repetition units of the superlattice and eventually disappears.

Taking $x = 1/L$, and κ_0=5 W/mK (an average value for oxides such as $SrTiO_3$, $PbTiO_3$, $LaCoO_3$ and others), and interface resistance

R_i=5·10^9 Km^2/W, in the range of the intergrain thermal resistance in oxides,[104,141,149] and superlattices,[150] the function κ(L) shows a minimum at L≈6 nm, that shifts to smaller values when the rugosity increases. Thus, increasing the rugosity of the interfaces, suppresses the minimum very rapidly, and drives the thermal conductivity a function that increases continuously with temperature.

On the other hand, note that increasing the parameter of rugosity does not affect κ(L) at large L, where incoherent phonon transport is dominant. The equation shows the existence of a minimum at the crossover between those regimes, its origin linked to a non-constant R_i with L.

Chen and Neagu[151] calculated the thermal conductivity for Si/Ge SLs using the Boltzmann transport equation for phonons that scatter specularly or diffusively in the interfaces of the SLs. At low L their model shows a greater thermal conductivity for specular scattering. The model presented here depicts an increase in the population of phonons that experiment specular scattering on decreasing L, which would render similar results.

Regarding our experimental data, equation (3.5) reproduces the κ(150K, L) data of the SLs down to L=5 nm with a roughness $\eta \approx 0$, using κ_0 = 7.8 W/mK (between the bulk values of $SrTiO_3$ and $LaCoO_3$), and R_i = 3.57 10^{-9} Km^2/W. See Figure 3.24.

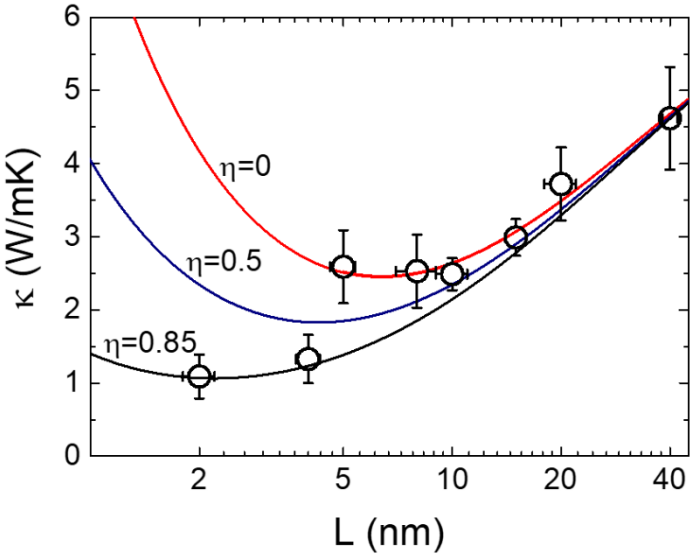


Figure 3.24. Fitting of experimental κ(150K) with equation (3.5), for different values of rugosity.

The fitting suggests that the plateau (or local minimum) of κ(L) at L=5-10 nm, and its lower magnitude below this L, is consistent with a rapid increase of the rugosity below this thickness range.

High-resolution electron microscopy analysis did not reveal any appreciable change in the rugosity or interdiffusion at the interfaces at L≤10 nm. For instance, the images shown in Figure 3.25 compare the results for two different superlattices, with L=2 nm and L=5 nm, and both show atomically abrupt interfaces, without appreciable mixing beyond a unit cell in any case.

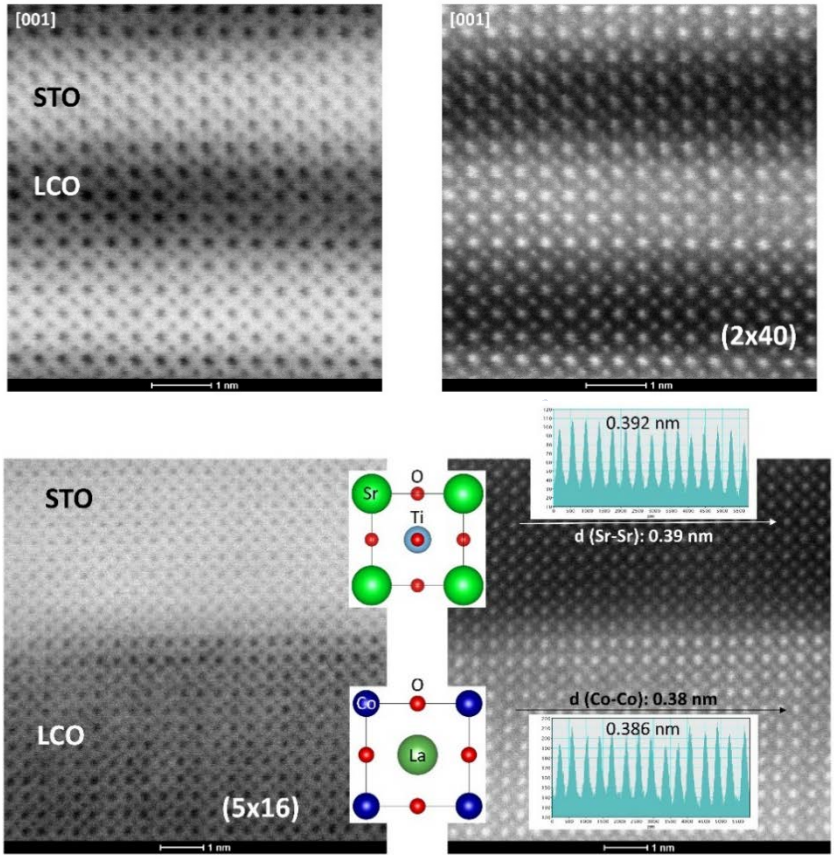


Figure 3.25. High resolution STEM (BF, left, and HAADF, right) images of the interfaces of (2×40), top, and (5×16), bottom, SLs. The interatomic distances obtained from line-scan EDX analysis are shown.

However, TEM analysis only probes a very limited region (nanometer size) of a much wider sample (mm size). In order to test the quality of the interfaces we measured their magnetic properties.

As mentioned in the introduction of this chapter, tensile strained LCO develops a magnetic order below a T_C=85 K, and a characteristic coercive field at low temperatures ≈ 1000 Oe.[136] Several magnetic

oxides of Sr-Co and Ti-Co are reported in the literature, that could give an indication of the formation of an alloy at the interface. For instance, $SrCoO_3$ is a ferromagnet with a much higher Curie Temperature (depending on the oxygen content and degree of strain it can be close to room temperature) with a smaller coercive field ≈ 100 Oe.[152–154] Other oxides, like Co_2TiO_4 and $CoTiO_3$, are also reported, although in this case with a smaller T_C than LCO.[155]

The magnetic properties of the SLs studied in this work are reported in Figure 3.26.

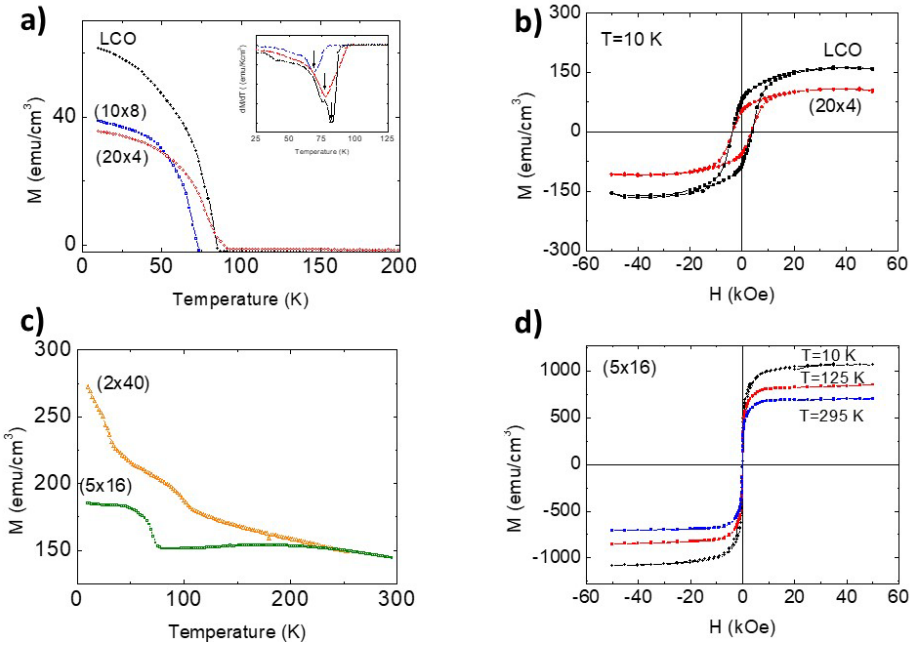


Figure 3.26. Temperature dependence of the magnetization (a,c), and hysteresis loops (b,d) of several LCO/STO SLs; a thin film of LCO on STO is also shown, for comparison. There is a clear change in the trend for L<10 nm.

The SLs with thicker films, i.e. L ≥10, show the same behavior as the LCO film, with a slight decrease of T_C (see the inset to Figure 3.26 a) and saturation magnetization. However, the magnetic phase changes completely at L≤10, with a new phase developing at higher temperatures (a low coercive field is visible at room temperature in the (5×16) SL; Figure 3.26 d). Note, however, that the ferromagnetic signal of strained LCO still develops at low temperature, even at the L=2 nm SLs. These results confirm the existence of an interlayer region, whose composition cannot be determined from our data, but from the magnetic behavior must be a mixed phase of the type (Sr,La)(Co,Ti)O_x, with a mixed valence for Co and Ti. Following the calculations by Ju *et al.*,[142] this mixed interfaces could promote phonon transmission through a more gradual relaxation of epitaxial strain and acoustic mismatch. The L at which the magnetic behavior changes is also the same at which some very faint satellite peaks appear in the RSM of the SLs to the sides of the SL peak (see the red circles marked in sample (10x8) in Figure 3.12), which have been proposed to appear in LCO due to the formation of ferroelastic domains.[134] Another possibility for the satellite peaks is that they are caused by the oxygen vacancy pattern observed by Zhang *et al*.[156] In any case, the formation of the different phase below a certain thickness points to a different method of strain relaxation, which is consistent with the disappearance of the satellite peaks.

As discussed before, we calculated the critical thickness of t_c≈4.5 nm for LCO on STO.[147,148] This calculation agrees with Zhang *et al*.[156]

They also found a suppression of the characteristic ferromagnetic phase of strained LCO in LCO/STO SLs with LCO layers thinner than ≈6 nm.[157]

Our hypothesis is that growing STO on top of a layer of LCO thinner than t_c, will promote intermixing to alleviate the tensile stress (Sr^{2+} is larger than La^{3+}; compensation of oxygen vacancies by $Co^{3+} \rightarrow Co^{2+}$ also increase mean ionic distances). On the other hand, for layers thicker than t_c, intermixing is not so energetically favored, as the stress is already partially relaxed.

Thus, interfacial mixing should increase as L decreases in the SL, reducing also the interface thermal resistance and promoting phonon transmission.

It is very fortunate that STO and LCO show many mixed-composition oxides with such different magnetic properties, as they offer a unique opportunity to probe the quality of the interfaces in the whole sample, instead of in very limited portions, as it is usually done through high resolution electron microscopy and other imaging techniques. We can see how, in this case, a simple magnetic measurement may be more informative than a very complex technique as HR-TEM.

A similar mechanism may be operative in other oxide SLs, suggesting an alternative interpretation for the appearance of the minimum in the κ(L) plot, based on a R_i dependent on L, at low L.

3.5. CONCLUSIONS

The heat transport in periodic superlattices does not follow a trivial tendency. Through a combination of SLs with different periods and thicknesses (as well as with an aperiodic repetition of the layers) I showed in this chapter that coherent and incoherent phonons are always present in the SLs, at all periodicities.

The SLs used in this work are of excellent crystalline quality, with sharp interfaces between the constituent materials, as shown by high resolution Electron Microscopy, EDX and different XRD analyses. However, magnetic studies showed that the interfaces show some degree of intermixing, particularly at the thinnest level, probably associated to strain relaxation phenomena.

The observation of a minimum κ(L), or alternatively, a κ at low L larger than expected based on an incoherent, particle-like phonon transmission of heat, is most probably related to the effect of mixed interfaces over phonons with different wavelengths, leading to a R_i dependent on L, below a certain L. This is an aspect that should be further investigated in every SL, in order to obtain accurate conclusions about the effect of structure on the phonons responsible for heat transport in nanostructures.

4. THERMAL CONDUCTIVITY OF $BaTiO_3$. EFFECT OF STOICHIOMETRY AND SIZE

4.1. OBJECTIVES OF THE CHAPTER, CONTEXT AND DISCUSSION OF PREVIOUS RESULTS

In this chapter I will discuss the results obtained from a set of thin films of barium titanate ($BaTiO_3$, BTO) with varying cation concentrations. The goal of this chapter is to disentangle the effect of different point defects from that of ferroelectric domain walls, film thickness and grain size, in polycrystalline thin films.

BTO is the prototypic ferroelectric material, the first ternary oxide in which ferroelectricity was discovered, circa 1946.[158–160] There is a vast amount of information on its structural, dielectric and ferroelectric properties, not only in bulk but also in thin films.[72,161–164] However, there is a comparative lack of accurate information on its thermal conductivity, particularly, on the role played by the different scattering mechanisms in heat transport in this material.[165]

Mante and Volger reported the κ(T) of BTO single crystals from 500 K down to 2 K.[80,166] The authors observed a strong effect of ferroelectric domain walls (DWs) over phonon propagation, as well as an increase of κ(T) at low temperatures (< 40 K), upon application of an electric field due to a reduction in the density of DWs.[80]

From the values of κ(T) ≈4-10 W m^{-1} K^{-1} and C_{vm}≈60-100 J mol^{-1} K, (in the temperature interval 150 K -300 K),[167] the average phonon mean free path can be derived from the expression of kinetic theory, $k(T) = \frac{1}{3} C v \lambda$, using an average velocity ≈4500 m s^{-1}. This crude approximation gives a λ≈2-4 nm, much smaller than the mean ferroelectric domain size, even in nanometer thick films, where these domains scale down to ≈30-50 nm.[168,169] A possible explanation to the reduction of κ(T) observed by Mante and Volger is that λ grows very much at lower temperatures for a high density of phonons, becoming comparable to domain size.

However, Davitadze *et al.*[167] and Donovan *et al.*[165] reported a reduction of κ(T) of nanograined BTO films, at room temperature. The grains in their films are 40-80 nm in diameter; a contribution of such large mean-free path phonons at room temperature and above, is less likely.

An important clue to understand this behavior may be obtained from the work of Jezowski *et al.*[170]; these authors reported a strong

decrease of κ in nanoceramic materials, as grain size is reduced. Interestingly, they observed a glass-like $\kappa(T) \approx 1$ W m^{-1} K^{-1} at 100 K in "black" ceramics, composed of 30 nm grain BTO. The black color probably denotes oxygen (and other) vacancies, which make BTO conducting and are an important source of phonon scattering.

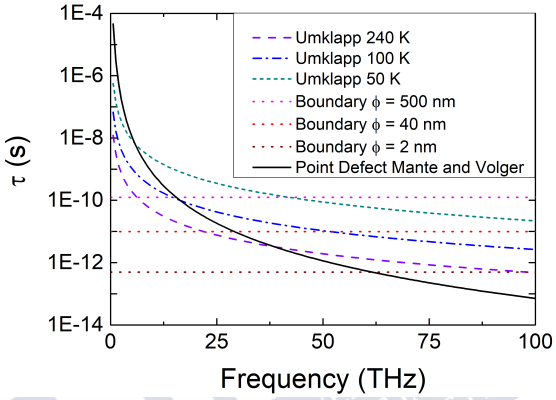


Figure 4.1. Frequency dependence of the relaxation time for the different scattering mechanisms, calculated for $BaTiO_3$ thin films. The Umklapp contribution was calculated with data from the literature (Ref. 171-173), and the point defect scattering was obtained by fitting the data from Mante and Volger (Ref. 80) to the Debye model. Above 50 THz, the dominating parameter is the point defect scattering; below this frequency, the dominant mechanism of phonon scattering depends on the size and temperature of the system.

Atomic defects tend to accumulate at grain boundaries in polycrystalline materials; this is particularly usual for oxide vacancies in perovskites, including BTO.[174–176] Thus, reducing grain size in ceramics or polycrystalline thin films may be a source of an increasing concentration of defects, which could diffuse from the boundary to the bulk (the smaller the crystal size, the larger the influence of the surface on the material), increasing the density of point defects as grain size

decreases. This could be a plausible hypothesis to explain the effect of grain size on the room temperature thermal conductivity of BTO thin films.

In the framework of the Debye model one can understand how the defects could affect the thermal conductivity of BTO. In Figure 4.1 the relaxation times for the different scattering mechanisms are calculated using equations (1.7)-(1.10) using data available in the literature.[80,171–173] This shows how point defect scattering may be dominant for ≥20-30 THz phonons in ≈40 nm thick films (see also Figure 4.2).

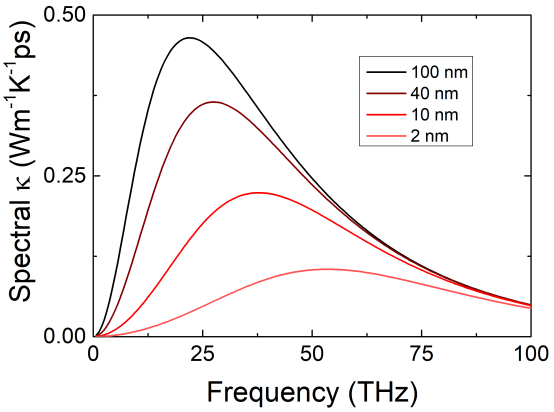


Figure 4.2. Spectral thermal conductivity for $BaTiO_3$ calculated with the Debye model at 100 K, for different boundary sizes (indicated in the legend) The point defect scattering used is the obtained from fitting the data from ref. 80 to the Debye model . Even for thin films with sizes of 40 nm (total film thickness or grain size in polycrystalline films), the contribution from >30 THz phonons is very important.

The information on the literature about the effect that cationic vacancies/defects have on the thermal conductivity of this material is

scarce, despite the use of different dopants in BTO for many of its applications.[158,164,177–179]

In this chapter I will discuss the effect of different types of vacancies on the thermal conductivity of polycrystalline thin films of BTO. I will discuss the effect of total film thickness, grain size, crystal orientation, and ferroelectricity, on the behavior of $\kappa(T)$ in this material.

4.2. Fabrication of $BaTiO_3$ thin films.

The thin films of BTO were fabricated by PLD, using the system described in the previous chapter. A BTO target was sintered from TiO_2 (99.8%) and $BaCO_3$ (99.98%). The powders were dried, weighted and mixed by hand in an agate mortar, before being pressed at 3 Tons in a 10 cm diameter pellet, and sintered at 1100ºC for 24 hours in air. The pellet formed was ground again in a mortar, pressed and sintered for 24 hours at 1300ºC in air.[180] The resulting target was hard, light brown, and showed pure $BaTiO_3$ phase in XRD,[181] as shown in Figure 4.3.

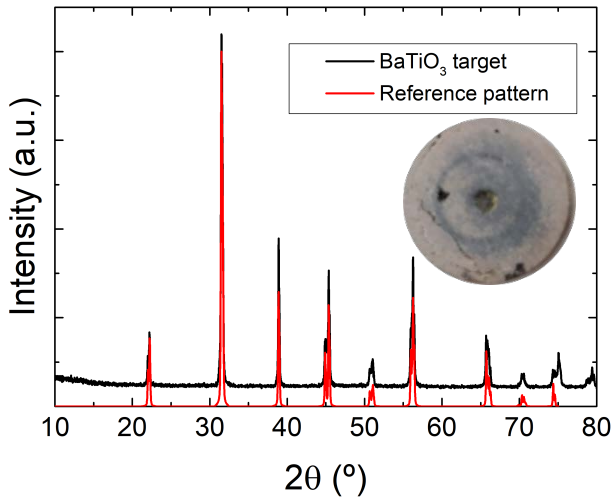


Figure 4.3 XRD pattern of the BaTiO3 substrate and reference pattern from ref. 26. A picture of the target after polishing is included as an inset. The darker area corresponds to the area impacted by the target.

The composition of the target was also analyzed by energy dispersive X-ray spectroscopy (EDX) in a scanning electron microscope (SEM), using a Zeiss EVO LS15 equipped with an Oxford Inca X-act analyzer. This technique allows to measure the energies of the X-rays that the sample emits after being irradiated with the electron beam. The irradiation promotes electrons of the sample to a higher energy orbital, which then relax to the ground state again by emitting a photon in the X-ray range. The frequency of these photons is characteristic for each element, hence the measurement of the energies of the emitted X-rays gives information about the elements comprising the sample.[182]

The results show a Ti/Ba ratio 1.06 (Figure 4.4), an indication that the stoichiometric cationic composition was achieved in the target.

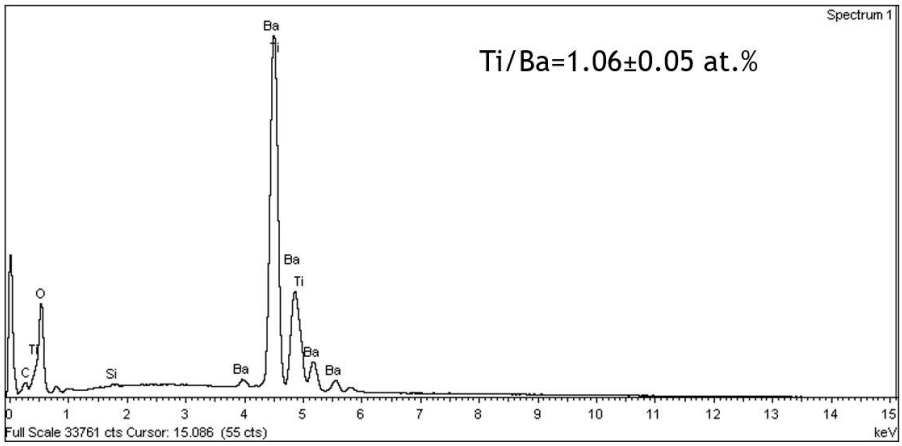


Figure 4.4. EDX spectrum of the $BaTiO_3$ target after the sintering process and polishing the surface. The Ti/Ba ratio obtained from the analysis is 1.06.

Kan and Shimikawa reported a strong effect of laser fluence on the final cationic stoichiometry of BTO films.[183] Thus, to produce a systematic variation in the density of cationic defects in our samples, we first prepared a set of films at 700ºC on (001)-STO, at an oxygen pressure of 100 mTorr, and with varying laser fluences between 0.6 and 2.3 J/cm^2.

We first fabricated a series of samples with a fixed thickness of 30 nm. This was used to study the effect of cationic concentration in the relaxation of epitaxial stress and crystallinity. The growth rate, calibrated ex-situ for each laser fluence, varies from 0.016 Å/shot for 0.6 J/cm^2, to 0.059 Å/shot for 2.3 J/cm^2.

Then, a subsequent set of samples using the same conditions, but with thicknesses of ≈80 nm, was grown to measure their thermal conductivity. Finally, an ≈80 nm film was also grown on top of $KTaO_3$, a cubic perovskite with a lattice parameter 3.99 Å (higher than STO), to study the effect of the strain on the concentration of defects, polycrystallinity, and thermal conductivity.

4.3. STRUCTURAL CHARACTERIZATION OF THE FILMS

The 30 nm-thick films present a combination of diffraction peaks in their out of plane XRD patterns, characteristic of more than one crystal orientation (Figure 4.5). A two-peak pattern was also observed by Kan and Shimikawa, for BTO on $GdScO_3$, from the presence of relaxed and strained layers.[183] Dubourdieu *et al*.[184] observed a combination of peaks arising from the different orientations of a BTO film grown on top of silicon with an STO buffer layer. They observed that the portion of the film in the vicinity of STO grows c-oriented, but after a thickness of less than 4 nm there is a partial relaxation and a mixture of both a/c-domains.

The blue and red lines in Figure 4.5 a) correspond to lattice distances of 4.041(3) Å and 4.006(2) Å respectively, close to the lattice parameters for bulk BTO c = 4.0335 Å, and a = b = 3.9945 Å .[181,185] As laser fluence increases, the peak signaling a-oriented domains grows in intensity. The partial relaxation of the films can be observed in the

RSM around an asymmetric reflection (Figure 4.5 b) which shows that the film is not completely strained in-plane with the substrate. The RSM should display two peaks, one related to the a-oriented domains and another to the c-oriented domains, however they are both wide, leading to the formation of the asymmetric broad peak.

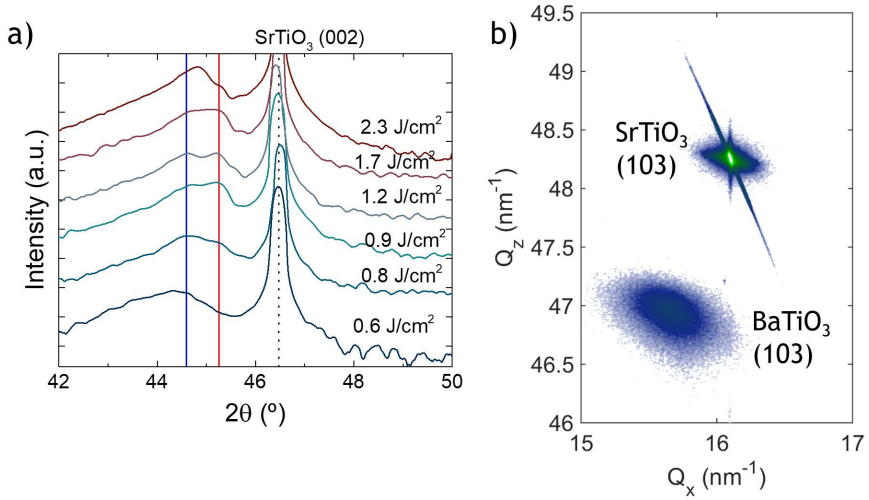


Figure 4.5. a) XRD patterns around the (002) $SrTiO_3$ peak (black dotted line), for the samples grown with the laser fluences specified. There are two different orientations combined in the films, with peak positions marked by the blue and red lines, corresponding to 4.041(3) Å and 4.006(2) Å lattice distances, respectively. b) RSM around the (103) peak of $SrTiO_3$ of the 30 nm thick sample grown with 2.3 J/cm^2. The film is partially relaxed, as the position in Q_x of the film signal is not aligned with the substrate.

Thus, the X-ray analysis is consistent with films of tetragonal BTO, with crystals out-of-plane-oriented along either their c-axis or a-axis, in different domains, whose relative population changes with the laser fluence.

The lattice distances obtained from the X-Ray analysis are shown in Figure 4.6. Both, for c-axis and a-axis oriented domains, the out of plane lattice parameter shortens on increasing the laser fluence, gradually approaching the bulk values.

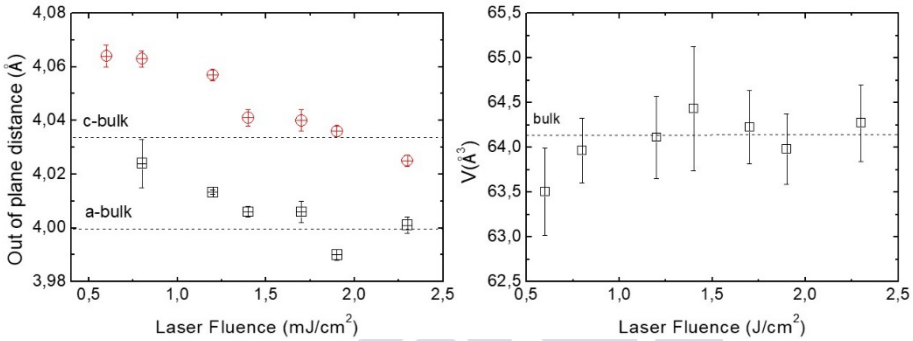


Figure 4.6. Out of plane lattice distances obtained from the fitting of the XRD pattern of each thin film. From the RSM data the volume of the unit cell is calculated using the more intense position of the peaks (right panel) and compared to the bulk.

To assess the effect of composition on the change of orientation observed by XRD, we measured the Ti/Ba ratio on the target by EDX after each deposition.[1] The results (Figure 4.7) show a preferential ablation of Ti (Ba) from the target as the laser fluence increases (decreases) above (below) a stoichiometric window (Ti/Ba≈1) between ≈1 and ≈1.5 J/cm^2. Moreover,the lattice parameters of the films (Figure 4.6) also show a plateau (i.e. they change the least) for the samples

[1] After each deposition the target was analyzed by EDX. Then, the target was polished and analyzed again, to ensure that that Ti/Ba =1 was recovered, before introducing it into the PLD chamber for a new deposition at a different laser fluence.

fabricated within this window, corroborating the fact that the BTO films are stoichiometric in this range of laser fluencies.

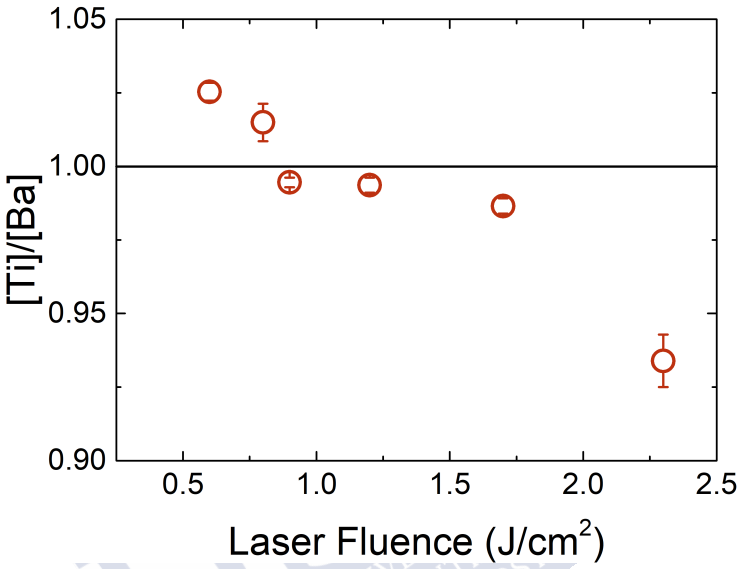


Figure 4.7. Ti/Ba ratio on the target after each deposition, as measured by EDX.

In principle, the opposite Ti/Ba ratio is expected in the samples, that is, Ti deficient films grow at lower fluences, whereas Ba deficient films grow at higher fluences. Although preferential scattering by the oxygen background could modify a fully stoichiometric target-to-sample transference, a transition from Ti-poor to Ti-rich with laser fluence was found previously by Keeble *et al.*[186] in $SrTiO_3$ films, suggesting that the laser fluence is the main control of the stoichiometry.

A set of thicker samples, around 80 nm, was also deposited. The XRD patterns for these films are shown in Figure 4.8 a); like the 30-nm

thick films, a combination of two different orientations (a two-peak structure) is observed. The lattice parameters extracted from the XRD are listed in Table 4.1. In this case, the distances are closer to the bulk, with a slight increase with increasing laser fluence, confirming a larger degree of relaxation as the thickness of the films increases.

Table 4.1. Thickness, roughness, and lattice parameters of the thicker films used for the thermal conductivity measurements. The distances listed as peak 1 and 2 correspond to the different orientations observed in the films.

Laser fluence (J/cm2)	Thickness (nm)	Roughness (nm)	Peak 1 (Å)	Peak 2 (Å)
0.6	81	4.9	3.999(4)	4.030(2)
0.8	79	4	4.000(2)	4.039(3)
1.2	84	5	4.001(2)	4.038(5)
1.4	72	2.9	4.007(4)	4.039(6)
1.7	72	2.9	4.008(1)	4.044(5)
1.9	80	5	4.024(1)	--
2.3	83	5	4.007(2)	4.048(4)

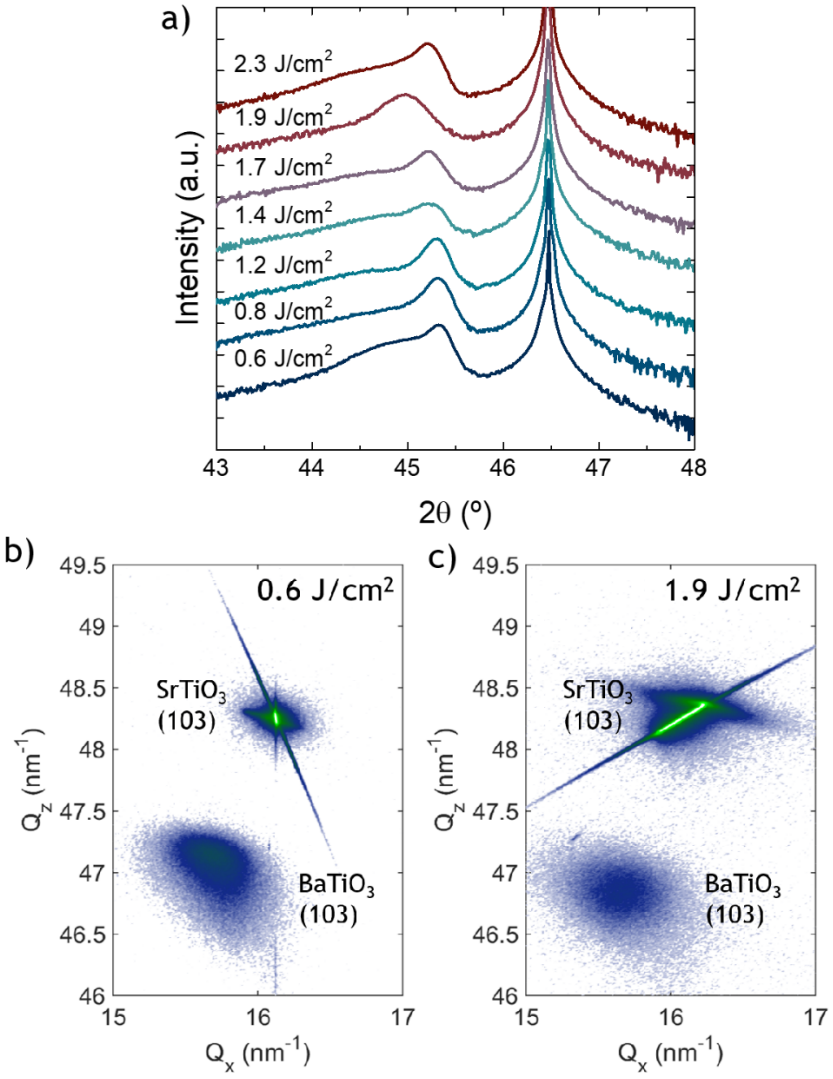


***Figure 4.8**. a) XRD patterns of the ≈80 nm thick samples grown with the laser fluence specified. The two peak structure is also visible, as in the thinner samples. b) and c): RSM for the samples specified around the (103) peak of the STO substrate. Both films appear relaxed with an area of the peak strained by the substrate.*

The surface roughness of the films obtained from XRR (Figure 4.9), also increases with laser fluence, particularly when out of the stoichiometric window, suggesting that the dispersion of grain sizes increases with increasing off-stoichiometry.

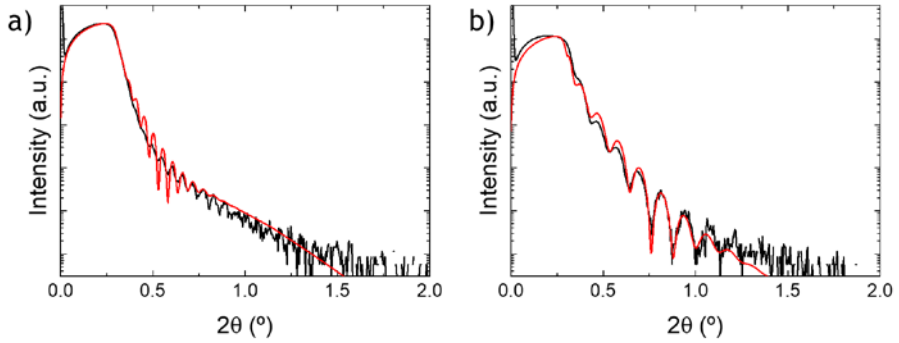


Figure 4.9. XRR data and fit for samples a) 72 nm thick, grown at 1.4 J/cm^2, and b) 34 nm thick, grown at 1.2 J/cm^2. The faster decrease of intensity in the thicker sample is due to the bigger surface roughness in this sample.

In the RSM it can also be observed how there is a peak that is relaxed with respect to the substrate, but it extends asymmetrically towards a part that is strained, which would be in the vicinity with the substrate. This can be seen in samples grown with different laser fluences, as shown in Figure 4.8 b) and c).

The microstructural and compositional analysis was performed from cross-section lamellae in a Jeol JEM-F200CF-HR transmission electron microscopy, equipped with spectrometer for EDX compositional analysis. The images and analysis of the TEM samples were obtained by Dr. José Manuel Vila Fungueiriño.

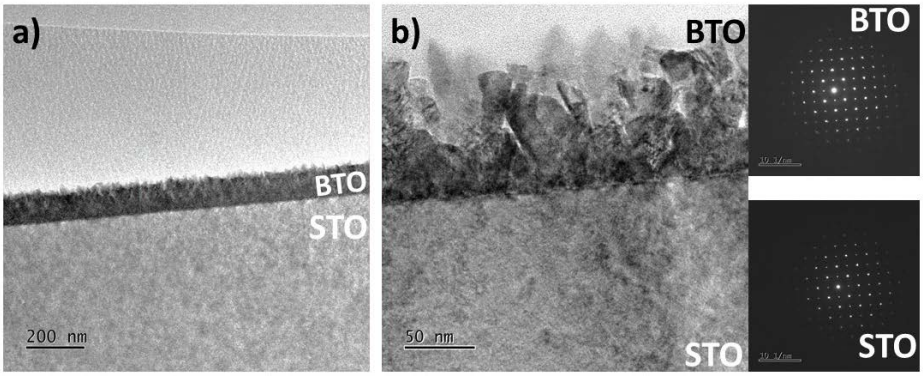


Figure 4.10. a) Low magnification STEM images of a cross section lamellae of the BTO thin film grown at 2.3 J/cm^2. b) higher magnification of the BTO layer, and Fourier transform patterns of the BTO layer and STO substrate.

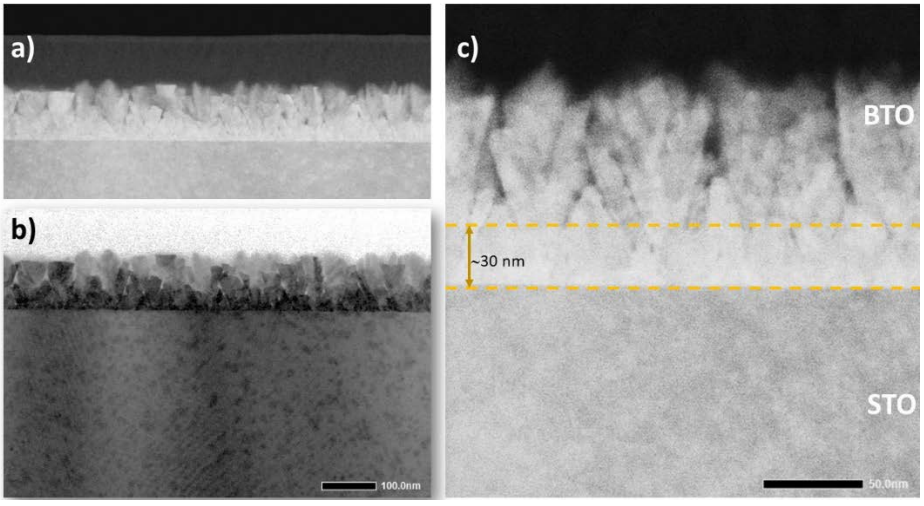


Figure 4.11. STEM images in bright (a) and dark (b) field modes of cross section lamellae of the BTO thin film grown at 2.3 J/cm^2. c) After a dense layer of 30 nm closer to the interface with the substrate, the growth in highly textured.

The TEM images shown in Figures 4.10 and 4.11 correspond to the films grown at the higher fluency, 2.3 J cm^{-2}. The thickness compares

well with the ones obtained from XRR and confirms that the calibration of growth rate for each energy was correct. The films present a dense layer of ≈30 nm close to the substrate, becoming more textured when moving towards the surface.

Similar results were obtained for the film grown at the lower fluence, 0.6 Jcm^{-2}. High resolution electron microscopy analysis shows a similar polycrystalline, highly textured film, with a dense epitaxial interface close to the substrate; see Figure 4.12. The blurred image of the atomic planes in the film (not in the substrate) in Figure 4.12 b) is caused by the distortion of the ferroelectric-ferroelastic domains. As the atoms in each atomic row are not exactly in the same position, there are deviations that lead to the blurred image as explained in Figure 4.12 e). This points out the ferroelectric nature of the films, even if the composition is far from the 1:1 Ba:Ti ratio, we will discuss this point further, vide infra. Furthermore, since the size of the ferroelectric domains scale with the size of the grains,[187,188] it is expected that the separation of the domain walls can be below 10 nm. The formation of ferroelectric-ferroelastic DWs is a typical relaxation mechanism for ferroelectric materials,[68,189–191] and therefore they are expected in the films to relieve the high strain imposed by the STO substrate.

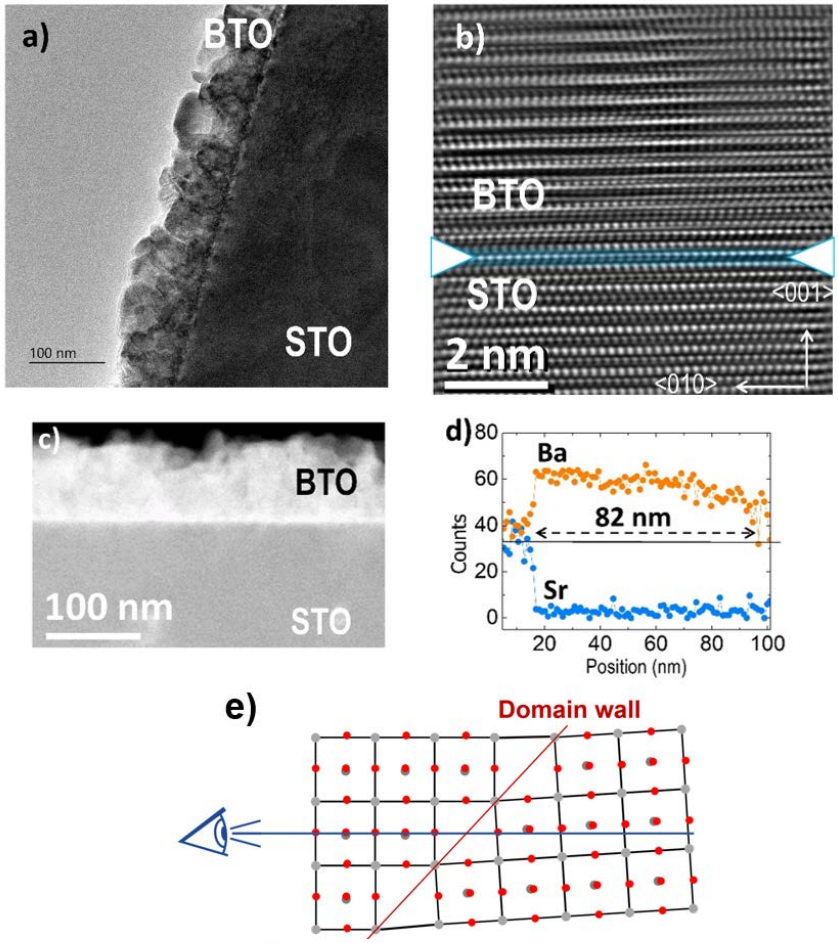


Figure 4.12. a), c) low magnification images of the film grown at 0.6 Jcm^{-2}. b) High resolution TEM image of the film, close to the interface with the STO substrate. d) EDX line-scan analysis of Ba and Sr along the film thickness. e) Scheme representing the cause of the blurring in image b), the domain wall and change in structure produces a blurring of the images in the BTO layer, even when the STO appears well defined, due to the displacement of the atoms, not keeping the atomic columns in their positions through the thickness of the lamella.

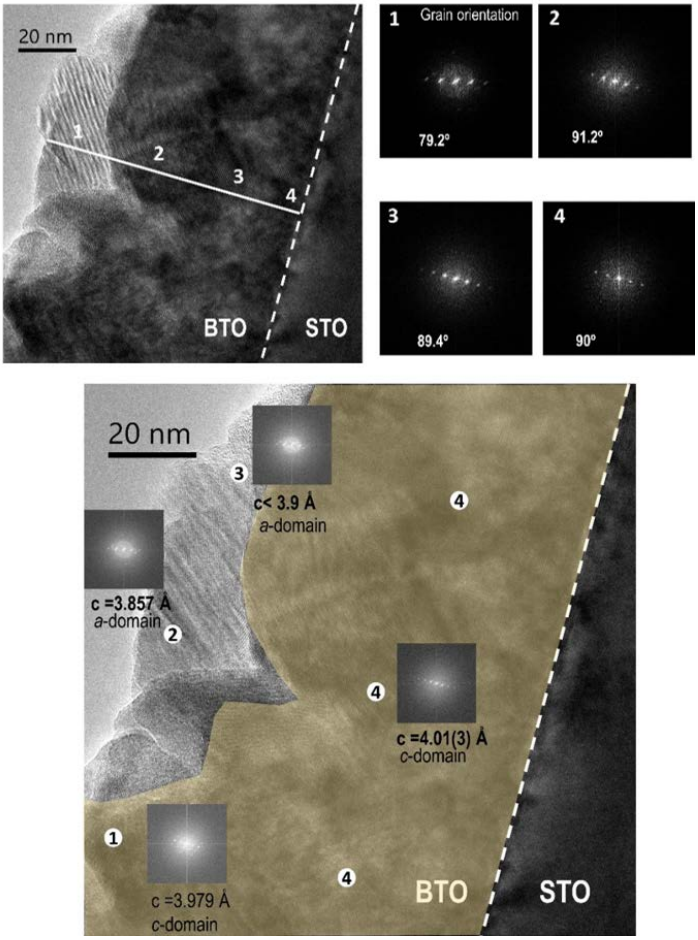


Figure 4.13. Top: High resolution TEM image of the lamellae of the film grown at 0.6 Jcm^{-2}, and Fourier Transform patterns obtained at different points along its length, as indicated. Departure from 90º denotes a deviation in the orientation of the BTO crystallites, i.e. increasing texturing of the film, moving away from the interface, towards the surface of the sample. Bottom: Different c-axis and a-axis oriented regions of the film, as identified from the Fourier transform at different points of the length and wide of the film.

A more detailed analysis of the microstructure of the film reveals the progressive change of orientation of the grains upon moving away from the interface. The analysis also shows that the dense layer closer

to the interface with the substrate is mainly c-axis oriented. On the other hand, close to the surface, the BTO layer is composed mainly by grains with the a-axis oriented perpendicular to the interface (Figure 4.13).

These results confirm our hypothesis from X-ray analysis, and are in agreement with the data by Dubourdieu *et al.*[192] for BTO grown in STO-buffered Si.

The Ti/Ba ratio was analyzed by EDX for both samples, as shown in Figure 4.14, for the sample at 2.3 Jcm^{-2}.

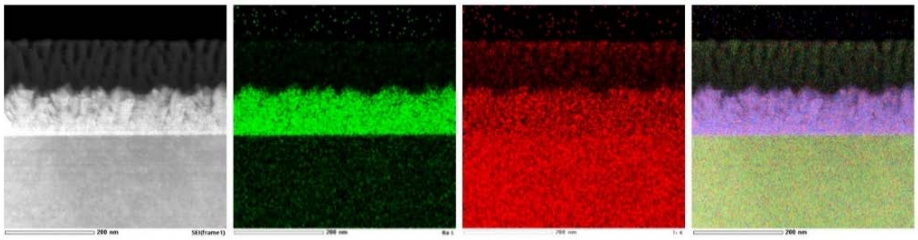


Figure 4.14. EDX analysis of sample grown with 2.3 J/cm^2. The EDX map for barium and for titanium is shown in green and red, respectively. The image af the right shows the superposition of both signals, showing the uniform distribution of the elements, without any sign of regions with precipitates or significant off-stoichiometries.

The Ti/Ba ratio in the films obtained from the EDX analysis is shown in Figure 4.15). We estimated the composition of the samples by interpolating between these extreme compositions, in order to obtain an approximate relationship between the Ti/Ba ratio in the films, and the laser fluence.

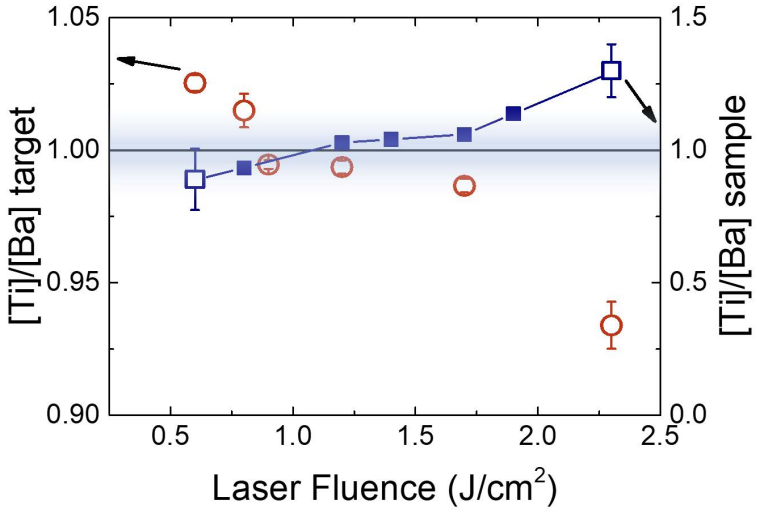


Figure 4.15. Experimental [Ti]/[Ba] ratio in the target (open circles), and in the two films measured by EDX (empty squares). The solid squares correspond to the interpolation, taking into account the relationship between the composition of the target and the films, for the two-extreme samples. The shadowed area signals a window where the films grow nearly stoichiometric.

Finally, before assessing the effect of composition on the thermal conductivity of the films, we must verify that the films remain ferroelectric (FE); a change in the ferroelectric character of the samples along the different [Ti]/[Ba] ratios explored in this work could be an additional effect over the thermal conductivity that could complicate our analysis and discussion of the results.

BTO stabilizes a tetragonal crystal phase at ≈5-120 ºC, presenting a FE polarization along the [001] axis.[158] Choi *et al.*[193] showed that the Curie temperature can be substantially enhanced in thin films due to epitaxial strain, and different works showed that the FE is maintained

at room temperature in thin films down to a few unit cell thicknesses. However, characterizing the FE state in such thin films is challenging.

Nonetheless, Tenne *et al.*[194] showed that UV-Raman spectroscopy is very sensitive to the polar modes of different oxide FE, and can be monitored even in thin films down to a few layers thick. Importantly for our discussion, they showed that the TO_3 mode of A_1 symmetry (Ti/O movement along [001]), appearing at ≈540 cm^{-1} in BTO films deposited on STO, is a fingerprint of FE polarization in this material.[195]

We have measured the UV-Raman spectra of three films, with [Ba]/[Ti] ratio 0.9, 1.05, and 1.3; the room temperature spectra are shown in Figure 4.16. The experiments were performed by the scientific services of the University of Barcelona, using a Dispersive spectrometer Jobin-Yvon LabRam HR 800, coupled to an optical microscope Olympus BXFM. The CCD detector was cooled at -70ºC, using a dispersive grating of 2400 lines/mm, and a HeCd laser with a wavelength of 325 nm. The laser power was kept at 0.5 mW in all the measurements.

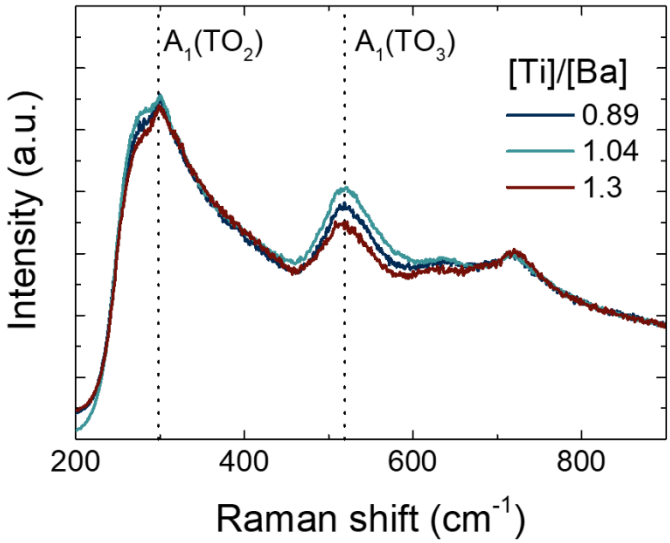


Figure 4.16. Room temperature UV-Raman spectra for three films. The data was normalized to the peak at 720 cm^{-2}, which comes from the STO substrate.

The peak at ≈298 cm^{-1} is characteristic of the tetragonal phase of BTO, and it appears on the three samples with similar intensity. Also, the $A_1(TO_3)$ ≈519 cm^{-1} is present in the three films analyzed. The intensity of this peak (after normalizing the spectra with respect to a peak from the STO substrate) is maximized in the most stoichiometric sample, probably due to the effect of vacancy-defects, but in any case, the difference does not seem significative. Thus, we can ensure that our films retain the polar state in the whole range of compositions studied in this chapter.

After this full characterization of the samples, we are ready to discuss the effect of composition on the thermal conductivity of the films.

4.4. THERMAL CONDUCTIVITY OF THE FILMS

The cross-plane thermal conductivity of the samples was measured from 25 to 290 K by the 3ω method. The results are shown in Figure 4.17.

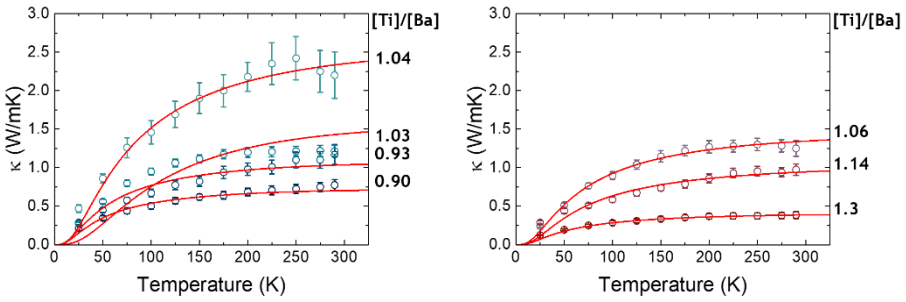


Figure 4.17. Thermal conductivity vs temperature for the films with different [Ti]/[Ba] ratio. The lines correspond to the fit to the Debye model, as explained in the text.

The thermal conductivity is higher in the most stoichiometric samples and decreases as the [Ti]/[Ba] ratio deviates from ≈ 1. This trend is better appreciated in Figure 4.18, where the value of κ at 250 K is plotted as a function of [Ti]/[Ba].

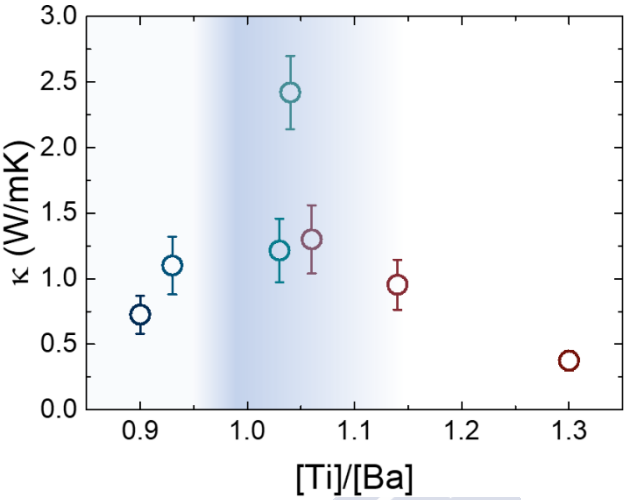


Figure 4.18. Thermal conductivity of the films, at 250 K, as a function of the [Ti]/[Ba] ratio. The shadowed area marks the nearly stoichiometric region.

To analyze the contribution of the different scattering mechanisms to κ(T), the data was fitted to the Debye model (equation 1.7) using the expression for the relaxation time discussed previously (equation 1.10):

$$\tau^{-1}(\omega) = A + B\omega^2 T e^{-\frac{\Theta_D}{\alpha T}} + C\omega^4 =$$

$$\frac{v}{\phi} + \frac{\hbar\gamma^2}{\overline{M}v^2\Theta_D}\omega^2 T e^{-\frac{\Theta_D}{\alpha T}} + \frac{3\delta^3}{\pi v^3}\sum_{i=1}^{N} x_i S_i^2 \omega^4$$

The Umklapp scattering parameter, $2.92 \times 10^{-19}\omega^2 T e^{\frac{-352}{T}}\, s^{-1}$, was calculated from data available in the literature Θ_D=429 K, γ=1.22, and *v*=4020 m/s.[171–173] For the concentration of defects, contained in the parameter *C* above, we used the data obtained from the EDX analysis. The point defect scattering parameter includes the Ba and Ti defects, using their masses and radii to calculate the value of the factor S_i that

appears in equation (1.10) using the expression presented in the equation (1.9). Aside from the cationic vacancies, 5% of oxygen vacancies was added in all the calculations.

The domain size, ϕ, in the boundary scattering term: $A=v/\phi$, was used as a fitting parameter. The values of B and C were allowed to vary ±20% from the initial parameters during the fitting. The results of these fittings are shown in Figure 4.17 and the resulting parameters in Figure 4.19.

The boundary size goes from $\phi\approx$10-12 nm in Ti-poor samples to $\phi\approx$4 nm in stoichiometric and Ti-rich samples. Grain sizes on the range of ≈15-20 nm range are visible in the TEM analysis discussed at the beginning of this chapter (Figures 4.10-4.14), so they could be the origin of this parameter.

The data in Figure 4.18 and Figure 4.19 suggest, then, that the main limiting factor of the $\kappa(T)$ in BTO is the presence of point defects.

Not that in Figure 4.1 we already showed that they are the limiting factor for the scattering of phonons above 25 THz in sizes on the range of 40 nm, which are responsible for a huge contribution to $\kappa(T)$ (see Figure 4.2).

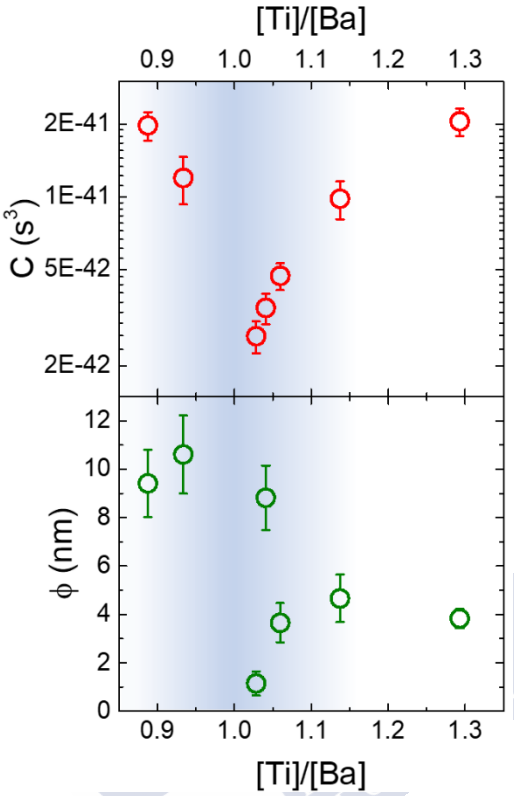


Figure 4.19. Point defect scattering (top) and domain size (bottom), obtained from the fit of the κ(T) of the films to the Debye model. The shadowed area marks the nearly stoichiometric region.

Finally, a sample was grown on top of (001)-$KTaO_3$ (KTO) at ≈0.8 J/cm^2. KTO is a cubic substrate with lattice parameter close to that of the BTO (3.99 Å). The strain for BTO on top of STO is -2.2%, while on KTO it is -0.11% Both the film deposited on top of STO and KTO with nearly the same laser fluences (≈0.8 J/cm^2) were characterized by atomic force microscopy (AFM).

AFM is a technique in which a very sharp tip on a cantilever is scanned through the surface of the sample. The attractive-repulsive interactions between the tip and the sample modify their distance, which causes the cantilever to bend. A photodiode is used to keep track of this modification of the sample-tip distance, and a feedback loop is used to keep it constant. There are different modes of AFM, regarding the tip-sample distance: contact (tip very close to the sample), non-contact (in which the tip is oscillating far from the sample) and tapping (in which the tip oscillates lightly "tapping" the sample in each oscillation). In this case contact mode was used, as we also tried to measure PFM (piezoelectric force microscopy, which will be further explained in the next chapter), but the small size of the domains expected with the small size of the grains in this samples makes it impossible to observe them with this technique, as the radius of the tip imposes a limitation on the smallest domain that can be observed with this technique (usually any domain bellow ≈15 nm is not visible). The AFM images (Figure 4.20) show a similar grain texture for both the sample grown on STO and KTO, with grain sizes in the range of 90 nm on STO and 70 nm on KTO. This suggests that the structure is similar for both samples.

However, in the XRD pattern of the sample deposited on KTO (inset in Figure 4.21) shows a very sharp peak, suggesting that there are no a-domains on the sample.

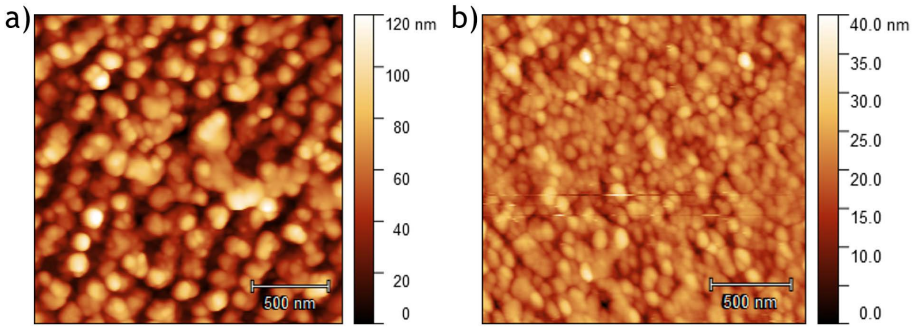


Figure 4.20. AFM topography images of the samples deposited on a) STO and b) KTO with approximately the same laser fluence. The size scale of the grains is around 90 nm for the sample on STO and 70 on KTO. This difference and the difference in density (which is seen on the broader scale seen on STO) is caused by the strain imposed by the substrate on the material.

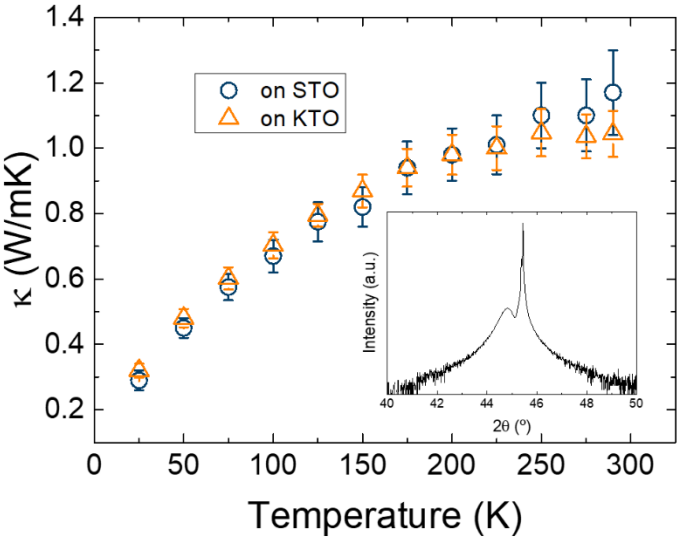


Figure 4.21. Thermal conductivity vs temperature for two BTO thin films frown on STO and on KTO with a laser fluence of 0.9 J/cm2, corresponding to [Ti]/[Ba]≈1.03. The inset shows the XRD pattern around the (002) KTO peak of the sample grown on KTO.

The thermal conductivity (Figure 4.21), however, is almost identical for samples on both substrates, suggesting that scattering at crystal domains is not an important source of control of κ(T) in BTO.

4.5. CONCLUSIONS

In this chapter we analyzed the results of κ(T) in a series of BTO thin films with a varying cationic concentration.

The change in stoichiometry introduced by the change in laser fluence does not lead to important changes in the polar nature of the films, as measured by Raman spectroscopy. HRTEM imaging shows signals compatible with the ferroelastic deformation across a domain wall through the path of the electron beam.

The interplay between cation vacancies, FE-DWs, and polycrystallinity of these films leads to a non-trivial dependence of the thermal conductivity of the films. There is a maximum in thermal conductivity close to the stoichiometric 1:1 ratio, with a decrease towards both sides.

Our data shows how it is important to take into account cationic defects during growth, as they are the main scatterers of phonons, at concentrations relevant for the κ(T) of the material. This should be taken into account when dealing with BTO for possible thermal conductivity-related applications.

USC
UNIVERSIDADE
DE SANTIAGO
DE COMPOSTELA

5. THERMAL CONDUCTIVITY OF $PbTiO_3$ THIN FILMS: EFFECT OF STOICHIOMETRY AND FERROELECTRIC DOMAIN WALLS

5.1. OBJECTIVES OF THE CHAPTER, CONTEXT AND DISCUSSION OF PREVIOUS RESULTS

In this chapter I describe the effect of cationic vacancies/substitutions and ferroelectric domain walls (DWs) on the thermal conductivity of $PbTiO_3$ (PTO) thin films. Unlike the case of BTO, this material can be grown as a single crystal on top of STO by molecular beam epitaxy (MBE); hence it is possible to disentangle the effect of the DWs and point defects on the thermal conductivity of a ferroelectric material, without having to consider the contribution from grain boundaries.[65]

PTO is a classic ferroelectric,[196] one of the undoped phases of the lead zirconate-titanate solid solution $(PbTiO_3)_x(PbZrO_3)_{1-x}$.[197–199] This family of compounds is extensively used for its piezoelectric properties, as it has a high piezoelectric response, with polarization as high as 0.4 C/m^2 in bulk for x=1.[200]

PTO is tetragonal at room temperature, with lattice parameters of a=b=3.904 Å and c=4.135 Å.[201] With increasing temperature, the tetragonality is gradually reduced, concomitant with the polarization, until the ferroelectric-to-paraelectric transition takes place (Curie Temperature ≈ 475°C).[202,203] The *a* and *b* lattice parameters are very close to those of STO (3.905 Å) at room temperature; however at the typical growth temperatures (around 600°C) PTO is either cubic or close to cubic (as it is either above the Curie temperature or close to). Note that the ferroelectric transition temperature increases with both tensile and compressive epitaxial strain.[202] Taking the pseudocubic lattice parameter of PTO (a_p ≈ 3.959 Å), the STO substrate exerts -1.36% compressive stress, making it an optimal substrate to grow this material purely *c*-oriented (the one in which the polarization is oriented) out of plane.[204]

Moreover, very important for the study planned in this thesis, bulk single crystal thermal conductivity of PTO is around 5 W/mK at room temperature,[205] which, with the decrease expected on thin films, will give values that can be accurately measured on STO substrates by the 3ω method.

On the other hand, there is a growing amount of evidences that show that the thermal conductivity of PTO can be controlled by electric and elastic stimulii.[75–79,84]

Theoretical work from the group of Jorge Íñiguez has shown how the thermal transport both parallel and perpendicular to the FE polarization can be affected by electric fields,[77,78] leading to an increase/decrease of κ with E, up to the coercive field. This is related to softening/hardening of phonon modes, modifying the phonon-phonon scattering relaxation time. For E applied perpendicular to the polarization, there is a decrease of κ caused by a symmetry breaking of the system due to the deformation induced in the lattice, leading to new phonon scattering mechanisms.[77] Furthermore, including a substrate that imposes a certain strain can greatly increase the *electrophononic* effect by at least an order of magnitude, leading to bigger changes in the thermal conductivity with the applied electric field.[78]

Theoretical calcultions of the thermal conductivity by M. Royo *et al*.[75] and Seijas-Bellido *et al*. [76] showed how a single 180º DW in PTO (separating domains with antiparallel polarizations) affects a wide range of phononic frequencies, from below ≈20 THz-to ≈30 THz. These authors calculated an increase of thermal resistance about 20% due to a single DW. Althoug this result depends on the range of sizes of the material explored with respect to the DW size, the results confirm extraordinary effect of DWs in the thermal conductivity of PTO.

On the experimental side, Foley *et al.*[79] and Ihlefeld *et al.*[84] showed that the thermal conductivity of PTO related materials can be modulated by an electric field.

In a previous work, we demonstrated how the different domain configurations imposed by varying the strain state in PTO thin films give rise to huge changes in the room temperature thermal conductivity of this material.[65] This change can be understood by using the equation (3.3), in which the effect of DWs in incorporated as a Kapitza resistance over the thermal conductivity of single-domain PTO (k_0):

$$\frac{k}{k_0} = \frac{1}{1 + \frac{2R_{DW}k_0}{d}}$$

From this expression an experimental R_{DW} of 5.0 ± 0.2×10^{-9} Km^{2}W^{-1} was calculated.

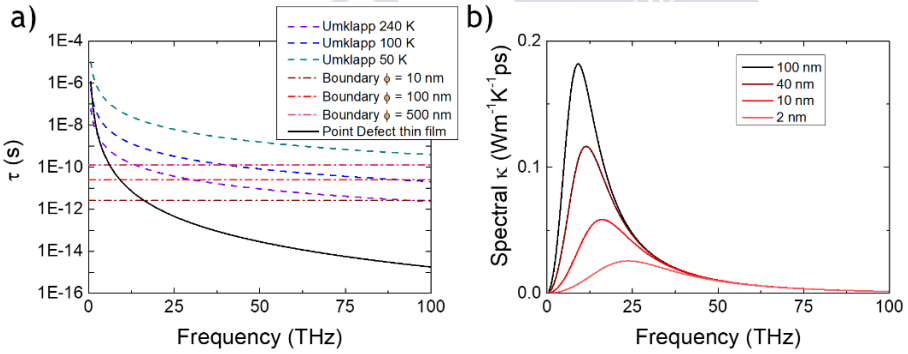


Figure 5.1. a) Relaxation times calculated for PTO for the different mechanisms present in the Debye model; the point defect parameter is the one obtained from the fitting of the stoichiometric sample shown in this chapter. b) Spectral thermal conductivity for different boundary sizes at 240 K; phonons of smaller frequencies are more affected, as expected from panel a.

However, the presence of cationic/anionic vacancies, substitutions, and other point defects affect the thermal conductivity, and what is more important for the present discussion, may act as DW pinning

centers, eliminating the possibility of reconfiguring their arrangement in the material.

The spectral contribution to κ(T) of PTO (calculated using equations 1.7-1.10) is shown in Figure 5.1 b); the large contribution of phonons below ≈25 THz, is rapidly suppressed by domain boundary scattering (particularly at ϕ<40 nm). Phonon transport should be restricted to phonons up to approximately 35 THz, as that is the highest frequency of acoustic phonons in PTO.[206] Thus, FE-DWs with average spacing in the range ϕ≈2-40 nm, may have a huge impact in the thermal conductivity of FE materials like PTO.[65,68] However, point defect becomes the dominant mechanism of scattering (the shortest relaxation time) for phonons of frequencies above ≈15 THz, at ϕ= 10 nm; thus the effect of vacancies affects κ(T) in a range of frequencies where boundary confinement is also important.

This simple calculation shows the difficulty of separating properly the contribution of FE-DWs and point defects, to the reduction of thermal conductivity of model ferroelectric materials, like PTO.

In this chapter I will study the thermal conductivity of a series of single-crystal PTO samples with an intentional grading of its compositions, covering a wide range from Pb-rich to Ti-rich. I will discuss the effect of atomic vacancies and substitutions in a FE sample and show the differences with respect to DW scattering contribution to the thermal conductivity of PTO.

5.2. FABRICATION OF THE $PbTiO_3$ FILMS

Differently from the other samples presented in this thesis, the films studied in this chapter were grown by reactive molecular beam epitaxy (MBE) by Dr. Eric Langenberg, as part of a project with the Laboratory of Prof. Darrell Schlom at Cornell University, USA.

MBE is a physical vacuum deposition technique capable of producing unparalleled high crystal-quality epitaxial films with very sharp interfaces due to the accurate control of the layer by layer growth at the atomic layer level.[207–211] In the reactive MBE, in addition, a mixture of oxygen and ozone is used as the oxidant species to grow multicomponent oxides.[207–211] The ultra-high vacuum of this technique ($\approx 10^{-9}$ Torr) ensures extremely low concentrations of impurities.[212] During the MBE growth process the different chemical elements that are to become the cations of the oxide film are independently evaporated from different sources, instead of using a laser to ablate a target containing the whole composition of the compound (the PLD case previously described). This is, each element is evaporated from a different crucible which is independently heated. In the case of our $PbTiO_3$ films, a conventional MBE effusion cell was used for Pb, while the Ti source was a Ti-Ball™ (Varian Associates, Vacuum Products Division).[213] Due to the low pressure in the vacuum chamber and the difficulty to oxidize Pb, distilled Ozone ($\approx$80% O_3 and 20% of O_2)[214] is used as the oxidant species. Note that ozone is much more oxidizing than oxygen and, thus, its use requires lower pressures to form the

desired oxide film. Using only O_2, as done with the highly energetic ablated species in the PLD process, would require too high pressures preventing the low energetic evaporated atoms in the MBE process from arriving to the heated substrate.

During growth, Pb and Ti were continuously codeposited (this is, the shutter of both sources are open simultaneously), achieving phase-pure $PbTiO_3$ in the growing film by adsorption control, where the desorption of the excess of Pb supplied is controlled automatically by thermodynamics[211]. This means that in the right distill O_3 pressure and substrate temperature window, monoatomic layers of PbO and TiO_2 automatically grow in an ordered succession. This phenomenon comes from the volatility of Pb and the preferential adsorption of the PbO layers on top of a TiO_2 layer instead of on top of another PbO layer. The growing film was continuously monitored by reflection high-energy electron diffraction (RHEED) to stay within the adsorption control growth window and, thus, to ensure the atomic layer by layer growth and the high-crystal quality.

Typically, the growth conditions were 9.0×10^{-6} Torr and 600°C for the distilled ozone pressure and the substrate temperature, respectively; and 1.7×10^{14} and 1.5×10^{13} atoms/(s·cm^2) for the lead and titanium fluxes, respectively.

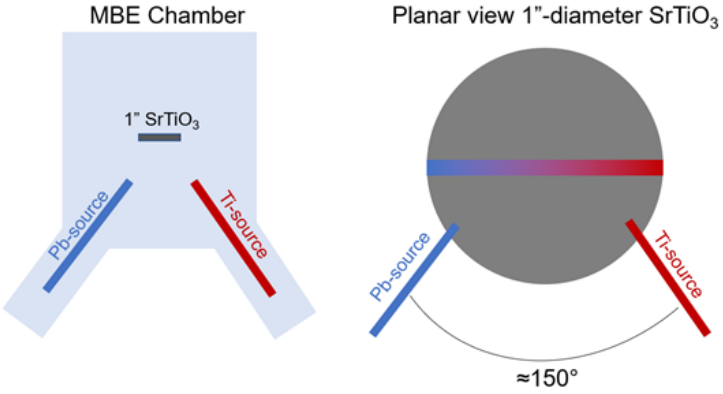


Figure 5.2. Scheme showing the disposition of the sources in the MBE chamber, as well as the direction of the cut in the wafer (the colored strip in the image on the left) used for the measurements presented in this chapter.

For the deposition of the samples of this chapter a $SrTiO_3$ wafer, 2.54 cm (1 inch) in diameter, was used. The substrate was kept fixed, without rotation during deposition, to intentionally avoid homogenization of the composition. Since the Pb and Ti sources are almost in opposite sides inside the chamber (approximately 150° apart, Figure 5.2) the absence of rotation means that towards one side and the opposite there will be a gradient in the concentrations of Pb and Ti, with a stoichiometric zone in the middle. The deposition rate was previously calibrated as 0.0079 nm/s, and the deposition was done to obtain 76 nm. A strip of the wafer was later cut into 7 pieces with different [Pb]/[Ti] ratios: three increasingly Pb rich, three increasingly Ti rich, and one stoichiometric.

5.3. STRUCTURAL CHARACTERIZATION OF THE FILMS

The compositional [Pb]/[Ti] ratio on the different pieces of $PbTiO_3$ was determined by Energy Dispersive Spectroscopy (EDX) analysis using an Environmental Scanning Electron Microscope (EVO LS15, ZEISS), with the INCA-X act detector (Oxford). We worked at low voltages (7 kV) to diminish the electron beam penetration into the substrate and, thus, maximizing the interaction with the film.

First, we acquired the spectrum and obtained the composition of Pb, Ti, and Sr. The signal from Sr comes from the $SrTiO_3$ substrate, as well as part of the Ti. Assuming a perfect stoichiometry in the substrate, and working always under identical conditions, we could thus calculate the [Pb]/[Ti] ratio of each film. We further assumed that the piece cut from the center of the wafer was stoichiometric and referred the other pieces to it, using the relative concentration of Ti in the samples ($[Ti]/[Ti]_{Stoich}$). The results are shown in Figure 5.3, as a function of the distance from the center of the wafer.

Most probably, the central piece was not completely stoichiometric either, as it will be discussed later, but it serves as a reference point for the discussion.

The departure from the stoichiometric [Ti]/[Pb]=1 ratio was further confirmed by structural characterization performed by X-ray diffraction (XRD).

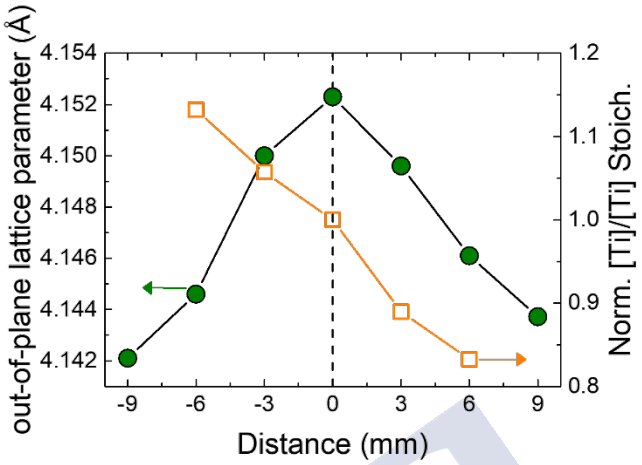


Figure 5.3. Lattice parameter from XRD and normalized [Ti]/[Ti]$_{Stoich}$ ratio for the samples cut at the distance specified away from the the center of the wafer.

The X-ray patterns of the samples are shown in Figure 5.4 a). The lattice parameters calculated from the X-ray diffractograms show a maximum for the sample in the center of the wafer, and an identical decrease to both sides (Figure 5.3). This behavior has been previously shown for other perovskite oxides, as vacancies are useful pathways for epitaxial strain relaxation,[215,216] and corroborates the departure from stoichiometry towards the edges of the wafer.

On the other hand, the Laue fringes around the Bragg peak of the films are indicators of their high crystalline quality, and coherent

growth through the whole thickness.[217,218]

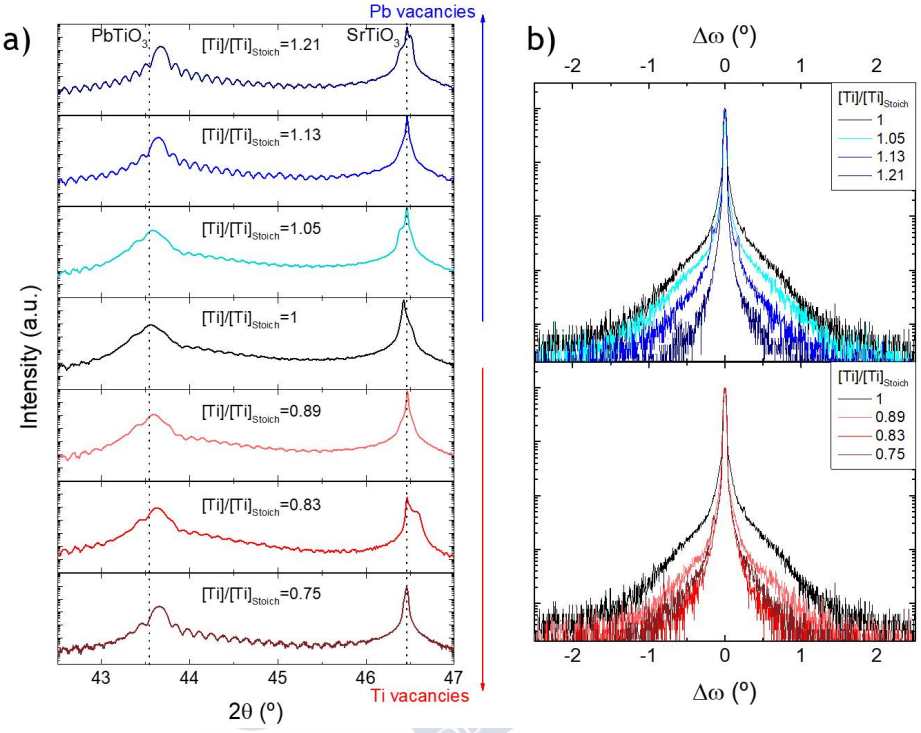


Figure 5.4. a) XRD patterns for the samples with the specified relative titanium concentration around the STO (002) peak and b) rocking curves around the (001) Brag peak of the $PbTiO_3$ with the relative Ti concentration specified in the legends. The width increases approaching $[Ti]/[Ti]_{Stoich}=1$.

The thickness of the films can be calculated from the fringes, using the equation (2.1):

$$t = \frac{\lambda m}{2(\sin(\theta_m) - \sin(\theta))}$$

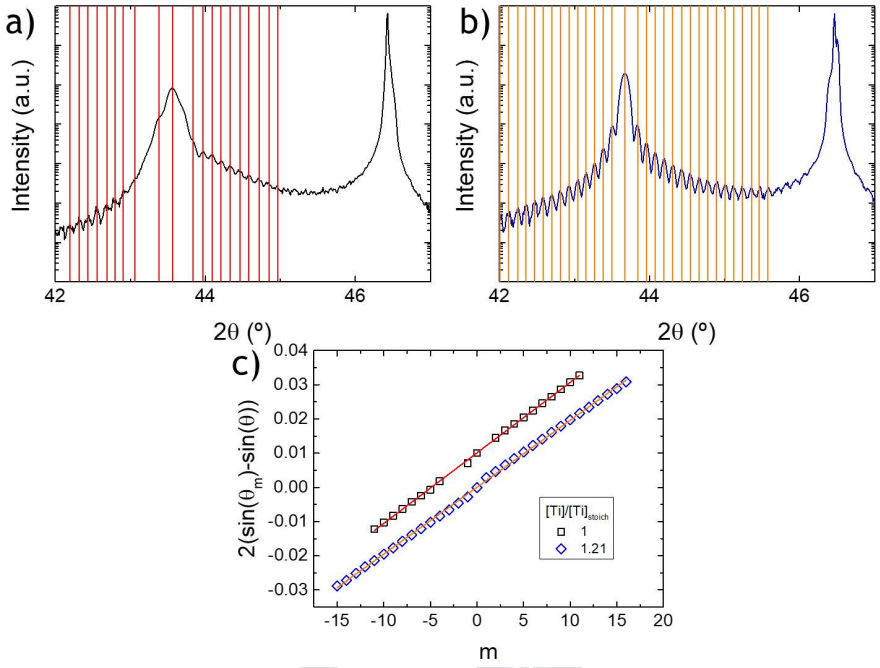


Figure 5.5. a) and b) XRD pattern around the STO (002) peak for the samples with relative titanium concentrations of 1 and 1.21 respectively. The positions of the Laue fringes are marked with vertical lines. c) Fit to equation (2.1) of the positions of the peaks of both samples (the data of sample with relative titanium concentration of 1 is shifted upwards by 0.01 for clarity). Both lines are almost parallel, indicating the thickness is very close for both films.

In Figure 5.5 the positions of the fringes as well as the fit are shown for two of the samples. The thicknesses obtained for all samples are listed in Table 5.1. The average thickness is 74.2±3.2 nm, but there is a clear thickening in the Ti-rich samples. As PbO does not adhere on itself, a lower Ti local pressure may lead to a smaller growth rate by

slowing the formation of the TiO_2 layer, being the limiting step in the growth process.

Table 5.1. List of thicknesses and out-of plane lattice parameters obtained from X-ray analysis.

$[Ti]/[Ti]_{Stoich}$	Thickness (nm)	o-o-p lattice par. (Å)
1.21	78.6±0.4	4.142
1.13	76.6±0.3	4.145
1.05	75.6±0.3	4.150
1	74.8±0.3	4.152
0.89	73.3±0.2	4.149
0.83	72.4±0.3	4.146
0.75	68.1±0.6	4.144

On the other hand, the Laue fringes are more apparent for the samples more distant from the center, i.e. when the films deviate from the stoichiometric ratio. This is certainly not the expected behavior as these oscillations relate to the long-range crystalline coherence of the crystal planes: thus, the larger the amount of point defects, the worst the crystal quality of the films.

Consistent with this observation, the rocking curves around the (001) peak (Figure 5.4 b) also show an unexpected trend, as the width increases as the $[Ti]/[Ti]_{Stoich}$ ratio approaches 1 (i.e. at the center of the wafer).

The RSMs taken around the 002 peak can give information about the domain configuration: a sharper peak indicates a lower concentration of DWs, as the changes in polarization up and down across the 180º DWs in these samples broaden the diffraction peak.[65] In Figure 5.6 the RSM for the different samples is shown, decreasing in width with increasing off-stoichiometry, indicating that there probably is a smaller concentration of DWs on departing from stoichiometry.

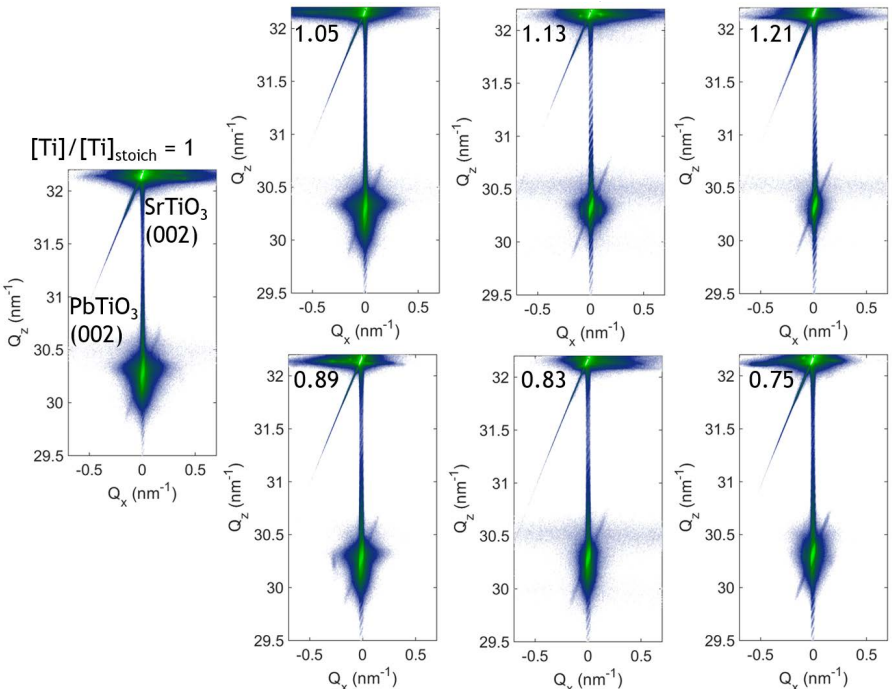


Figure 5.6. RSM around the STO (002) reflection for the samples with indicated [Ti]/[Ti]$_{Soich}$. Deviating from the stoichiometry leads to thinner diffraction peaks.

To investigate the ferroelectric domain structure in these thin films Piezoelectric Force Microscopy (PFM) in a dual ac resonance track

mode was used. PFM is a variation of Atomic Force Microscopy (AFM) in which an AC voltage is applied to the sample with the tip and keeps track of the expansion/contraction due to the piezoresonse of the material as a response to the AC voltage. The applied voltage on the tip causes the FE material to change its size according to the inverse piezoelectric effect. This allows to image the domain distribution of a ferroelectric material in the scale of nanometers. As in our samples only c-domains are present (i.e., with out-of-plane polarization), the out-of-plane piezoresponse displacements (z displacements) is the largest. That is why only the vertical piezoresponse is measured. The change in z is recorded by a lock-in amplifier due to the small magnitude. This vertical piezoresponse displacement can be either in phase or out of phase compared to the ac excitation field depending on the direction of the polarization. If the electric field is parallel to the polarization, the movement will be in phase, and if they are antiparallel, it will be out of phase, switched 180º (Figure 5.7). This allows to differentiate between domains pointing up or down. Furthermore, the DWs between one polarization and the other will not exhibit a piezoresponse, so the amplitude recorded for them is zero, allowing to map the distribution of DWs.

The measurements were performed using an Asylum MFP-3D Bio (Asylum Research) at the ICN2 facilities in Barcelona. The typical excitation voltage was in the range of V_{ac} = 1.5 - 3.0 V. PtIr conducting tips (PointProbe® Plus-Electrostatic Force Microscopy from

Nanosensors) were employed, with typical resonance frequencies around 350 kHz for the vertical piezoresponse.

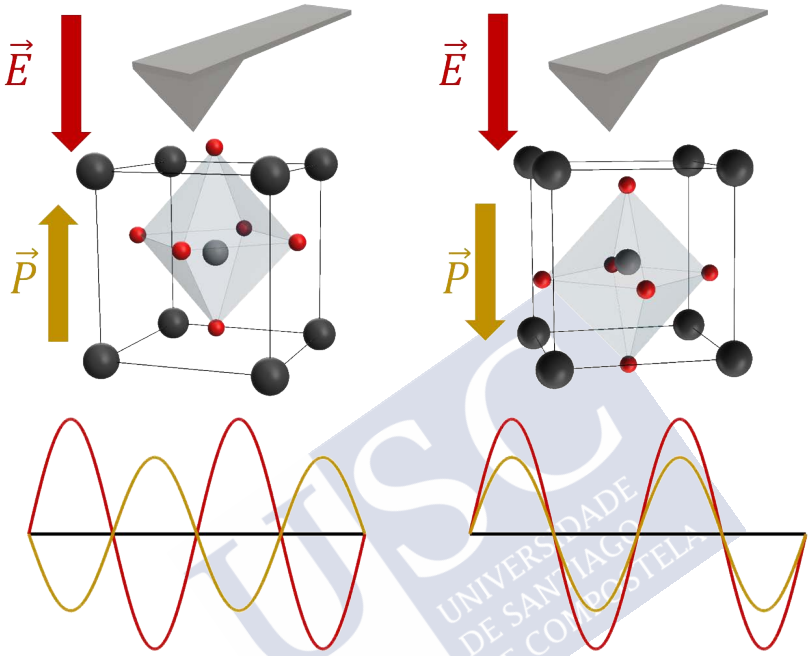


Figure 5.7. Scheme of the change in polarization induced by the field applied by the tip in the PFM. If the field (red line in the bottom panels) is antiparallel to the polarization, the deformation (yellow line in the bottom panels) will be out of phase, while if it is parallel, they will be in phase.

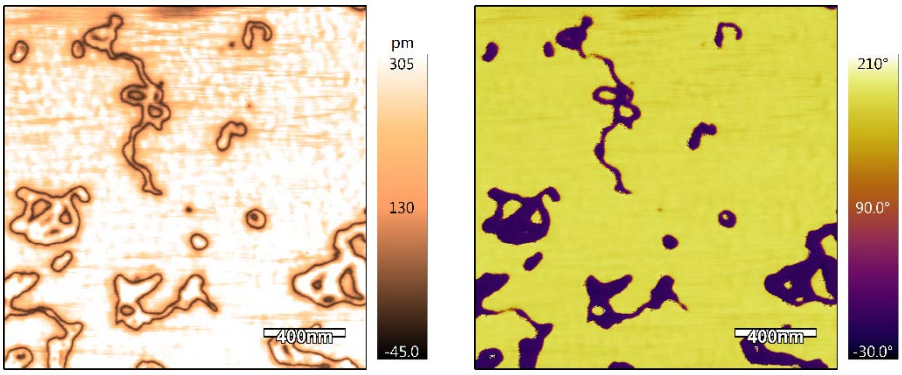


Figure 5.8. PFM amplitude (left) and phase (right) images of the stoichiometric sample. It can be seen how the DWs observed in the amplitude image correspond with the outlines between up and down polarization domains in the phase image.

Figure 5.8 shows the amplitude and phase images for the stoichiometric sample. A combination of up and down domains is visible, with DWs separating them. The phase PFM images in Figure 5.9 show that the concentration of DWs decreases as the samples deviate from stoichiometry. This is expected, as off-stoichiometry can heavily affect the ferroelectricity of these materials.[216] From this data it seems as the introduction of one or other kind of defect induces a particular polarization, up or down, instead of eliminating the ferroelectricity altogether. However, due to the absence of a bottom electrode it was not possible to change the polarization of any of the films to corroborate this idea.

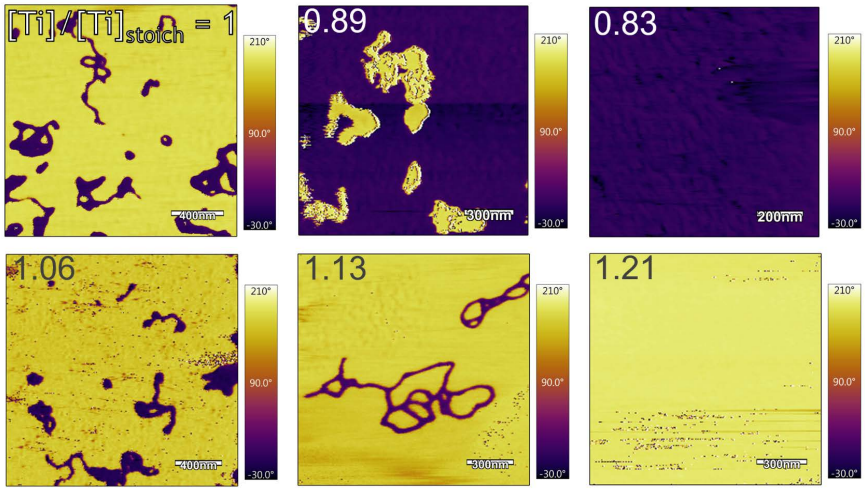


Figure 5.9. PFM phase images for the sample with the relative titanium concentration specified in the insets.

Therefore, to corroborate that the films with the highest concentration of defects are still polar, Raman spectroscopy was performed at the scientific services of the University of Barcelona, using a HeCd laser with a wavelength of 325 nm. The system is equipped with a dispersive spectrometer Jobin-Yvon LabRam HR 800, coupled to an optical microscope Olympus BXFM. The CCD detector was cooled at -70ºC, and the dispersive grating has 2400 lines/mm. The laser power used in the measurements was 0.5 mW.

Tavares *et al.*[219] measured the Raman spectra of different $La_xPb_{1-x}TiO_3$ ceramics with x from 0 to 0.3. They observe that upon increasing the concentration of La the peaks shift to lower positions, and their intensity decreases (the peaks are not visible for the highest La concentrations they used). This is caused by the loss of the polar phase

of PTO with the inclusion of La, consistent with the ferroelectric to paraelectric transition of PTO at high temperature. In the cubic paraelectric phase the Raman modes should disappear, while in the low temperature tetragonal ferroelectric phase the modes A_1 and E, which appear from the splitting of T_{1u} and T_{2u} modes in the tetragonal system, appear.[220] Therefore, we expect that the same would happen in the samples presented here if they lost the polar, and therefore ferroelectric, phase of PTO. However, the position of the A_1 and E modes barely changes (all are within error of the fit performed either to a Gaussian or a Lorentzian peak), and the intensity does not change at all, as visible in Figure 5.10. The conclusion is that the films are still polar within the stoichiometry ratios studied in this work.[220]

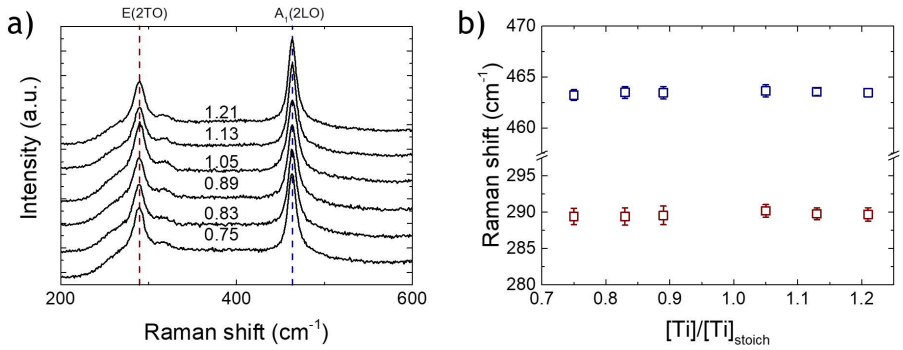


Figure 5.10. a) Raman spectra of the samples with the specified relative titanium concentration. b) the positions of the two marked peaks, E(2TO) and A_1(2LO) versus the relative titanium concentration.

Previously, a preferred orientation of c-domains was observed in stoichiometric PTO on STO.[65] This orientation is caused by the incomplete built-in field originating from the substrate.[221] The

explanation we propose for the exotic worm-like pattern observed in these samples is that some cationic inhomogeneities are present in the samples, as Pb and Ti diffuse from one end to the opposite during the growth. This would also imply that a higher concentration of Pb or Ti would favor the polarization to point up or down.

Consistent with this hypothesis, Weymann *et al.*[222] reported that growing thin films at different temperatures favored the up or down polarization. Specifically, high temperatures lead to polarization pointing up and low temperatures to polarization pointing down. This effect is due to a difference in the concentration of Pb in the films, with an excess of Pb at low temperatures (and deficit at high ones). In this case, excess of Pb produces a polarization pointing up, and its deficiency, down.

An alternative explanation could be that the furthermost samples from the center have completely lost the ferroelectric behavior and are non-polar. In any case, the amount of domain walls decreases with the introduction of defects, and faster decreasing the Ti concentration than by increasing it.

5.4. THERMAL CONDUCTIVITY OF THE FILMS

The thermal conductivity of the films at 250 K is plotted in Figure 5.11. In principle, as vacancies are defects that produce the scattering of phonons,[27–29] increasing the amount of Ti or Pb vacancies one would

expect a decrease in the thermal conductivity moving away from the stoichiometric region. However, the results show that the stoichiometric sample has a lower thermal conductivity than those with more vacancies. As discussed before, it has been shown that ferroelastic domain walls in ferroelectric materials produce the scattering of phonons.[45,75,76,80,82]

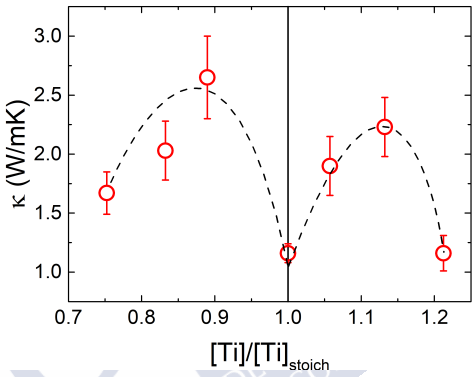


Figure 5.11. Thermal conductivity of the different samples at 250 K. The dotted line is a guide to the eye.

At low vacancy concentration (the stoichiometric sample), the defects do not have a big effect on the thermal conductivity, but the high density of domain walls causes a decrease in the thermal conductivity. However, on departing from the stoichiometry, the domain wall density decreases, as observed by PFM, increasing the thermal conductivity. Finally, in the most extreme cases, the concentration of defects increases to large enough values so that they reduce the thermal conductivity again.

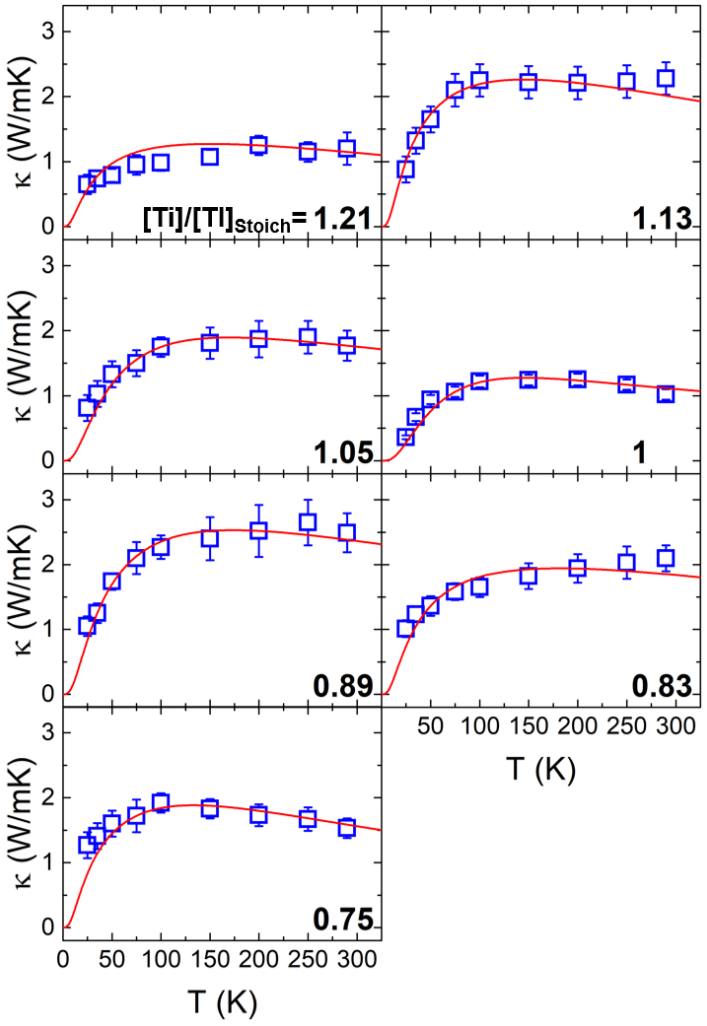


Figure 5.12. Thermal conductivity vs temperature for the samples with the relative Ti concentration specified in each panel, with fitting to the Debye model.

The Debye model allows us to understand how these two contributions affect the thermal conductivity in a more quantitative way.[223] The fits of κ(T) of the films to the Debye model (equations 1.7-1.10) is shown in Figure 5.12. In this analysis, the point defect

scattering and the boundary scattering contributions to the relaxation time (the first and third term in equation (1.10)) are the ones of interest:

$$\tau^{-1}(\omega) = \tau_B^{-1} + \tau_U^{-1} + \tau_D^{-1} = \frac{v}{\phi} + \frac{\hbar\gamma^2}{\overline{M}v^2\Theta_D}\omega^2 T e^{-\frac{\Theta_D}{\alpha T}} + \frac{3\delta^3}{\pi v^3}\sum_{i=1}^{N} x_i S_i^2 \omega^4$$

In the fittings, the starting values of the Umklapp term were calculated from data available in the literature[224,225] and allowed to vary (see Table 5.2). For the boundary scattering term, a maximum value of ϕ was set at the thickness of the films.

For the point defect scattering, the values were calculated from the data obtained by SEM-EDX by using the expression for S_i (equation 1.9):

$$S_i^2 = S_1^2 + (S_2 + S_3)^2$$
$$= \frac{a}{a+b+c}\left[\frac{1}{12}\left(\frac{M_A}{\bar{M}}\right)^2 + \frac{2}{3}\left(1 + \frac{2}{\sqrt{3}}Q + \frac{1}{3}Q^2\right)\gamma^2\left(\frac{R_A}{\bar{R}}\right)^2\right]$$
$$+ \frac{b}{a+b+c}\left[\frac{1}{12}\left(\frac{M_B}{\bar{M}}\right)^2 + \frac{2}{3}\left(1 + \frac{2}{\sqrt{3}}Q + \frac{1}{3}Q^2\right)\gamma^2\left(\frac{R_B}{\bar{R}}\right)^2\right]$$
$$+ \frac{c}{a+b+c}\left[\frac{1}{12}\left(\frac{M_C}{\bar{M}}\right)^2 + \frac{2}{3}\left(1 + \frac{2}{\sqrt{3}}Q + \frac{1}{3}Q^2\right)\gamma^2\left(\frac{R_C}{\bar{R}}\right)^2\right]$$

For the samples that are deficient in Ti, since Pb can present a 4+ valence, the possibility of Pb^{4+} occupying the Ti^{4+} positions was considered. The calculation for the cation defects in that case was done with the mass and radius of Pb^{4+} in octahedral configuration (0.775 Å),[226] a Q of 4.2, as the harmonicity of the neighboring bonds is not modified as there is still an atom, in opposition to having a vacancy, where the harmonicity is modified where Q takes a value of 3.2 according to Klemens.[27] For the Ti-rich samples the composition is

taken as having lead vacancies, therefore zero mass and radius defects, and 3.2 for Q. All the fittings were performed assuming a 5% of oxygen vacancies.

The results of the fittings are summarized in Figure 5.13 and Table 5.2.

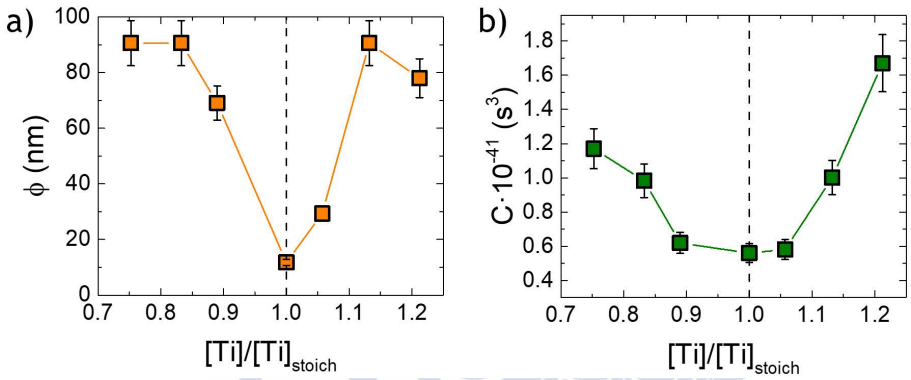


Figure 5.13. a) Casimir length and b) point defect scattering parameter from the Debye Model fit for the different samples. The Casimir length increases when departing from the stoichiometry due to the disappearance of the domain walls, while the point defect scattering increases.

Good fits to the experimental data can be obtained by changing the Umklapp term slightly around its initial value (Table 5.2) and with a point defect density that deviates only slightly from the initial calculation. The Umklapp term presents no clear trend, except for the sample with $[Ti]/[Ti]_{stoich}=1$, which has a higher value. However, the boundary scattering term ϕ shows a clear dependence upon the composition of the films, with the smallest $\phi \approx 10\text{-}15$ nm occurring for the stoichiometric film. The boundary size increases very rapidly with

departure from stoichiometry, until reaching the limiting value of the film thickness at ≈ 80 nm.

This behavior, together with the X-ray and PFM analysis discussed before, signals the strong effect of the gradual disappearance of the DWs on the κ(T) of $PbTiO_3$ thin films.

It is also important that the defect scattering parameter, *C*, does not vary much for small departures from stoichiometry, there is wide minimum between $[Ti]/[Ti]_{stoich}$≈0.9-1.1. This explains why, at low/moderate concentrations of point defects, DWs are the main phonon scatterers, playing the major role in determining κ of ferroelectric materials. Increasing the off-stoichiometry, results in a rapid increase of *C*, while ϕ remains approximately constant at ≈80 nm, and therefore point defect scattering determine the thermal conductivity of the $PbTiO_3$ films.

Table 5.2. Data used in equation (1.6) for the fit to the Debye model of the different samples for the boundary scattering (A), Umklapp scattering (B) and point defect scattering (C)

$[Ti]/[Ti]_{Stoich}$	A (s^{-1})	B ($s \cdot K^{-1}$)	C (s^3)
0.75	$4.3 \cdot 10^{10}$	$8.0 \cdot 10^{-18}$	$1.2 \cdot 10^{-41}$
0.83	$5.3 \cdot 10^{10}$	$3.0 \cdot 10^{-18}$	$9.8 \cdot 10^{-42}$
0.89	$6.5 \cdot 10^{10}$	$4.0 \cdot 10^{-18}$	$6.19 \cdot 10^{-42}$
1	$3.3 \cdot 10^{11}$	$2.4 \cdot 10^{-17}$	$5.6 \cdot 10^{-42}$
1.05	$1.3 \cdot 10^{11}$	$7.8 \cdot 10^{-18}$	$5.8 \cdot 10^{-42}$
1.13	$4.3 \cdot 10^{10}$	$4.0 \cdot 10^{-18}$	$1.0 \cdot 10^{-41}$
1.21	$5.0 \cdot 10^{10}$	$5.3 \cdot 10^{-18}$	$1.7 \cdot 10^{-41}$

The gradual transition between the dominance of both scattering mechanisms results in the maximum of κ at a moderate concentration of point defects.

5.5. CONCLUSIONS

The results presented in this chapter disentangle the effect of ferroelectric DWs and cationic vacancies in the thermal conductivity of PTO thin films. The introduction of either Pb or Ti deficiency leads to a decrease of DW concentration, while Raman spectroscopy confirmed the polar character of all the samples studied in this work.

A complete characterization of the samples, along with a fitting of the κ(T) through the Debye model, suggests a gradual transition between a regime in which the thermal conductivity is controlled by DW scattering, and another one in which defects are the main factor affecting κ.

Thus, only the most stoichiometric samples will be candidates for an active control of their thermal conductivity, through the application of an electric field that may change the DW configuration. This is an important aspect to consider in a material that is a promising candidate in the field of phononics for the fabrication of phonon valves.[65,76,79,84]

6. GENERAL CONCLUSIONS AND OUTLOOK

The aim of this thesis was to understand thermal transport in two cases that have drawn a lot of attention lately: superlattices and ferroelectric thin films. The main general conclusions obtained from this work are:

There is always a contribution of coherent, wave-like phonons and incoherent, particle-like phonons in oxide superlattices at every period. The contribution of both changes with the interface mixing, which introduces a thickness-dependent interfacial resistance. This may lead to the appearance of a minimum at $\kappa(L)$, not related to a globaltransition between both types of phonons, but being of an “extrinsic” nature.

The main extrinsic contribution limiting the thermal conductivity of a material are point defects (of different types) and the presence of interfaces. The latter are normally grain boundaries or the total thickness in the case of a thin film. In FE materials, our analysis (and previous data) show the domain walls may be an important source of phonon scattering.

Through the consideration of the characteristic relaxations associated to these phenomena, we have designed a strategy to disentangle the effect of these contributions to the κ(T) of two FE materials: $BaTiO_3$ and $PbTiO_3$. Our results show that point defects control the thermal conductivity in $BaTiO_3$, while FE-DWs are the main responsible of phonon scattering in stoichiometric $PbTiO_3$.

These results are very important in order to design materials with tunable κ(T). Our study allows an understanding of what the optimal composition and structure are, in order to obtain a ferroelectric system with a good performance as a reconfigurable thermal conductivity element.

USC UNIVERSIDADE DE SANTIAGO DE COMPOSTELA

RESUMO EN GALEGO

La revolución más recente que experimentou o mundo é a da electrónica. A maior causa desta revolución foi el control que se ten sobre os electróns dende a invención do transistor, polo que os seus inventores gañaron o premio Nobel en 1956.[1] O control sobre os fotóns, os cuantos da luz, permitiu o desenvolvemento da fotónica, que tamén axudou a acadar maiores evolucións no mundo da electrónica.

Por outro lado, o son xa fora unha das primeiras formas de comunicación do home e que tamén utilizan outras muchas especies animais, e contribuíu amplamente á evolución da nos especie a través das linguas. O estudio do son deu lugar a novas tecnoloxías como o sónar ou as ecografías. Sen embargo, non temos un control sobre a partícula responsable da transmisión do son e da calor en sólidos illantes: os fonóns. Os fonóns son as cuasipartículas (xa que se necesita un medio para definilas) relacionadas cos modos normais de vibración dos sólidos nos que os átomos que os forman vibran colectivamente.[4]

Para entender o transporte da calor podemos pensar na teoría cinética, na que o transporte de calor é proporcional á enerxía das

partículas, a súa velocidade e o seu camiño libre medio.[15] A enerxía dos fonóns pódese obter a partir da teoría de Debye con unha boa aproximación.[17] A velocidade dos fonóns pódese obter da súa dispersión, que está relacionada ca forza dos enlaces entre os átomos que os forman e as masas deles.[17] Por último, o camiño libre medio pódese ser substituído pola velocidade multiplicada polo tempo de relaxación durante o cal as partículas experimentan un proceso de dispersión. Os diferentes procesos de dispersión que poden sufrir os fonóns poden ser sumados a un total para así calcular a condutividade térmica del sistema.[23]

Existen tres mecanismos de dispersión: as interaccións fonón-fonón, a dispersión nos límites de gran do material, e la dispersión causada polas impurezas presentes na rede cristalina.

Modificar algún de estes parámetros levará a unha modificación da condutividade térmica de un material. As interaccións fonón-fonón son características do material e non poden ser modificadas. As fronteiras de gran e las impurezas poden ser controladas durante a fabricación do material e poden dar lugar a diferencias na condutividade térmica importantes, por exemplo, Berman mediu a condutividade térmica dun cristal de zafiro de 3 mm e alumina sinterizada a 40 K, obtendo valores de 5000 W/mK, y 100 W/mK, respectivamente,[26] o que mostra a diferencia entre un monocristal e un polvo cristalino. Walker e Pohl introduciron defectos puntuais en cristais de KCl ao crecer os cristales

introducindo pequenas cantidades de KI y NaCl, mantendo a estrutura, producindo diminucións na condutividade térmica de hasta un 60%.[21]

Este modelo de Debye permítenos polo tanto cuantificar canto se dispersan os fonóns polos distintos mecanismos, e polo tanto saber como podemos modificalos para conseguir o resultado que se desexe. Tamén nos da a posibilidade de coñecer fonóns de que frecuencias son responsables dunha maior parte do transporte térmico, así como observar que mecanismos afectan máis a que frecuencias en distintos materiais. Esta información pode ser moi útil. Os defectos puntuais, ao causar dispersión tipo Rayleigh, son proporcionais a ω^4, e por tanto terán un efecto maior para fonóns de frecuencias máis altas, mentras que las fronteiras de gran producen un efecto independente da frecuencia, polo que serán máis relevantes para fonóns de frecuencias máis baixas que non se ven tan afectados polos defectos puntuais.

A comunidade científica ten dedicado moitos esforzos a modificar a condutividade térmica de materiais segundo sexa necesario, por exemplo buscando unha redución en materiais termoeléctricos para así mellorar o seu rendimento.[53,54] En outros casos o que se necesita é un aumento da condutividade térmica, como sucede con polímeros nos que se introducen partículas con una maior condutividade para aumentar a do sistema total.[227]

Un tipo de sistema particularmente interesante son as superredes. Compostas por dous materiais intercalados, formando una estrutura por

capas, o seu comportamento non é tan sinxelo como cabería esperar. Se un pensa en cada intercara entre os dous materiais como un límite de gran, un podería esperar que canto máis fina sexa cada capa, e polo tanto máis xuntos estean as intercaras, máis baixa será a súa condutividade térmica. Isto é así cando o tamaño de cada capa es suficientemente grande como para que os fonóns sufran algún tipo de proceso de dispersión antes de recorrer toda a capa. Sen embargo, cando o camiño libre medio dos fonóns é similar o maior que o tamaño das capas formando a superrede, os fonóns poden viaxar de forma coherente a través da mesma, mostrando una condutividade térmica maior da que se esperaría. Este comportamento foi explicado por Simkin e Mahan[14] ao calcular a distribución de fonóns para una superrede. O modelo opuesto,[14,151] que ten en conta unicamente a natureza de partícula dos fonóns e a súa dispersión en cada intercara, utiliza unha resistencia fixa por cada intercara, polo tanto a condutividade térmica total vai diminuíndo cantas máis se atopen no material. Nesta tese proponse un modelo sinxelo que ten en conta que hai fonóns que non se ven afectados polas intercaras, pero outros que si o son, e define a fracción dos primeiros de forma inversamente proporcional ao espesor de cada capa, introducindo tamén unha rugosidade, que canto maior sexa menor será a cantidade de fonóns que poidan atravesar as fronteiras das intercaras coherentemente. Este modelo permite polo tanto axustar os datos del capítulo relativo a las superredes.

Os outros dous capítulos de resultados céntranse polo seu lado en dous materiais ferroeléctricos, xa que las paredes de dominio ferroeléctricas presentes nestes materiais dispersan os fonóns.[65,79,80,84] As paredes de dominio son reconfigurables, xa que igual que un material ferromagnético pode ser orientado cun campo magnético externo, no caso dun ferroeléctrico pódese facer con un campo eléctrico externo, afectando ás paredes de dominio. Isto permitiría conseguir un control activo sobre a condutividade térmica de forma reversible nun dispositivo.

TÉCNICAS EXPERIMENTAIS

Nesta tese usáronse dúas técnicas de fabricación de mostras: PLD (Pulsed Laser Deposition) para os casos das superredes e tamén das mostras de $BaTiO_3$, e mediante MBE (Molecular Beam Epitaxy) as mostras de $PbTiO_3$. Ambas permiten crecemento epitaxial dos materiais e teñen lugar dentro dunha cámara de alto baleiro, aínda que funcionan de forma diferente. No crecemento mediante PLD un láser pulsado de alta enerxía golpea un branco do material que se quere depositar, producindo a ablación do mesmo, formando un plasma ou pluma, facendo que parte chegue ao substrato onde se desexa deposita-la mostra. Nesta técnica úsanse presións de oxíxeno (O_2) relativamente altas (que poden alcanzar as centenas de mTorr), e altas temperaturas no substrato. Pola outra banda, no MBE[207–209] non é posible utilizar estas altas presións, xa que os materiais proveñen de fontes atómicas da

que se evaporan independentemente para chegar ao substrato.[213] No caso das mostras presentes nesta tese, para obter óxidos utilizouse ozono (O_3) destilado[214] para poder oxidar os materiais, xa que require unha presión moito menor que o uso de O_2, facilitando así que os átomos cheguen ata o substrato.

Tódalas mostras foron caracterizadas mediante técnicas de raios X.[88] Mediante reflectometría de raios X (XRR) pódese obter información referente ao espesor das capas, así como a súa rugosidade e densidade. Coñecer o espesor das mostras é moi importante para as medidas de condutividade térmica, xa que úsase no seu cálculo, polo cal unha boa calibración do espesor durante o crecemento e a posterior medida son moi importantes. Para coñecer a estrutura das capas depositadas utilizouse difracción de raios X (XRD) que permite obter información sobre o parámetro de rede fora del plano nas capas finas, así como mapas de espazo recíproco (RSM) que permiten obter tamén información sobre a estrutura no plano das mostras e polo tanto o seu estado de tensión polo substrato.

A medida da condutividade térmica de todas as mostras realizouse usando o método 3ω. Para isto, unha resistencia de 10 μm de ancho, 1 mm de largo e 100 nm de Pt ou Au con 10 nm de Cr para adhesión depositase tanto sobre a capa fina como sobre o substrato. A través das resistencias faise pasar unha corrente AC de frecuencia ω mediante unha fonte Keithley 6100, e mídese o terceiro harmónico da voltaxe que causa na resistencia cun lock-in de Stanford Research Systems modelo

SR830. Ao pasar a corrente pola resistencia, esta quéntase polo efecto Joule, que tamén será alterno, cunha frecuencia 2ω. Este quentamento fai que a resistencia varíe a esa mesma frecuencia, xa que o seu valor non é independente da temperatura. Debido a que a corrente ten frecuencia ω y que la resistencia ten una compoñente 2ω, hai unha compoñente da voltaxe directamente relacionada co cambio en temperatura de frecuencia 3ω. Polo tanto, ao medires esta voltaxe 3ω ao variar a frecuencia da corrente se obtense un quentamento que é lineal fronte a ln(2ω). Da pendente de esta recta pódese obter a condutividade térmica do substrato directamente coñecendo o cambio de resistencia ca temperatura. As medidas feitas sobre o substrato e sobre a mostra ca mesma potencia teñen un desprazamento vertical independente da frecuencia, que é causado pola capa fina, e polo tanto coñecendo o espesor da capa fina e as dimensións da resistencia, pódese obter a súa condutividade térmica.

RESULTADOS E CONCLUSIÓNS

Superredes de $LaCoO_3$ y $SrTiO_3$

Neste capítulo estudiáronse unha serie de mostras de aproximadamente 80 nm de espesor total formadas por repeticións de STO ($SrTiO_3$) y LCO ($LaCoO_3$) (de espesor L=2-40 nm) fabricadas sobre substratos de STO con orientación (001). A intención do capítulo era comprobar como varía a condutividade térmica con estes cambios, así como o

efecto de aumentar o espesor total ao manter o espesor de cada capa constante.

A caracterización mediante raios X mostrou unha gran calidade de tódalas mostras, mostrando picos de superestrutura relacionados ca repetición da unidade (a suma dunha capa de STO e outra de LCO). Ademais de obter o espesor mediante XRR, os picos de superestrutura tamén permiten obtelo a partir dos datos de XRD e RSM, sendo comparables os resultados obtidos das distintas técnicas. Os picos son estreitos e ben definidos, mostrando novamente a alta calidade das capas. Os patróns de difracción foron tamén simulados mediante o código CADEM,[91] obtendo moi boas comparacións dos resultados reais cos simulados, demostrando que as estruturas obtidas son as desexadas.

Tamén se realizaron imaxes de microscopía electrónica de transmisión (TEM) para observar la estrutura das mostras. Tódalas medidas mostraron unhas intercaras ben definidas, así como una altísima calidade estrutural, con columnas atómicas que se manteñen a través do espesor total das mostras. As medidas de EDX ou EELS (técnicas que permiten obter información sobre a composición atómica da mostra en nanoescala) non presentan ningunha interdifusión catiónica entre os dous materiais, demostrando novamente a súa alta calidade estrutural.

A condutividade térmica das mostras de 80 nm de espesor total a 150 K ten una tendencia que non é trivial: diminúe ao diminuíren o

espesor das capas que as forman, mostrando un aplanamento entre 10 y 5 nm de espesor de cada capa, para despois volver a baixar novamente. Isto demostra que a poboación de fonóns que transportan calor de forma coherente ou incoherente está afectando ao transporte térmico en estas mostras. O feito de que a condutividade volva a baixar debería estar relacionado ca rugosidade das capas, sen embargo, os valores obtidos mediante XRR e o que se pode observar nas imaxes de TEM non indican que haxa cambios dunhas mostras a outras.

Ao realizar medidas magnéticas observase que para as mostras con $L \leq 10$ o comportamento é diferente a unha mostra de LCO de 80 nm, tendo un pequeno campo coercitivo a temperatura ambiente, e formando a fase magnética do LCO a máis baixa temperatura. Isto indica que hai unha fase intermedia entre as dúas capas, non observable mediante TEM, con un comportamento magnético distinto aos dous materiais por si mesmos. Esta fase intermedia sería maior canto menor sexa L, afectando así á condutividade térmica das superredes de menor L maioritariamente.

As mostras con un cambio no espesor total presentan unha condutividade térmica maior canto maior é o espesor total. Isto indica que hai fonóns que viaxan de xeito coherente a través da estrutura e están restrinxidos polo espesor de 80 nm, e polo tanto, ao aumentar o espesor total aumenta a condutividade térmica. Isto es así non soamente para as mostras de L pequeno, senon tamén para L=20.

Por último, introducir cambios na periodicidade afecta tamén á condutividade térmica das estruturas. Para comprobar isto fabricáronse tamén tres mostras formadas por 6 capas, una con 15 nm en todas elas, unha con 15 nm de media, pero variando entre 17 e 13 nm o espesor de cada unha, e outra con unha capa doutro material, $Sr_3Al_2O_6$, en vez de unha das capas de STO no medio da mostra. A condutividade diminúe ao introducir aperiodicidade nas mostras e máis aínda ca introdución dun material distinto na estrutura. Os fonóns coherentes veríanse afectados pola aperiodicidade diminuíndo a súa condutividade, mentres que os incoherentes non, de forma que esta variación mostra una vez más que hai fonóns coherentes en estas mostras.

Capas finas de $BaTiO_3$

Este capítulo dedicouse ao estudio do efecto dos cambios na estequiometría do $BaTiO_3$ (BTO) na súa condutividade térmica. Para elo, fabricáronse unha serie de capas finas mediante PLD variando a fluencia do láser sobre substratos de STO (001). O cambio da fluencia produce un cambio na relación dos catións que son ablacionados do branco, de forma que se pode controlar a relación Ti/Ba mediante este parámetro.

O efecto do cambio de enerxía estudiouse con unhas mostras de espesor en torno a 30 nm, realizando SEM-EDX despois de cada deposición para medir a relación Ti/Ba no branco, observándose unha

diminución ao aumentar la fluencia del láser, pulindo o branco entre deposicións para retomar a relación estequiométrica.

Seguidamente fabricáronse unhas mostras de 80 nm de espesor con distintas fluencias para as medidas de condutividade térmica. Os seus patróns de XRD teñen dous picos en cada reflexión, indicando unha mestura de orientacións nas mostras. Isto púidose observar tamén mediante TEM de dúas das mostras, nas que se observa unha capa veciña á superficie do substrato que crece epitaxialmente, e que ao aloxarse do substrato se observa unha relaxación que leva a distintas orientacións. As medidas de TEM-EDX nestas mostras demostran que a estequiometría nelas é a oposta á do branco despois da deposición, polo que se pode extrapolar para obter valores no resto das mostras fabricadas.

A condutividade térmica mostra unha clara tendencia ca relación Ti/Ba, cerca de 1 a condutividade térmica é máxima, en torno a 2.5 W/mK a 250 K, baixando ata 0.7 W/mK para Ti/Ba=0.9 y 0.4 W/mK para Ti/Ba=1.3.

A análise mediante o modelo de Debye demostra que los defectos puntuais son a maior causa de dispersión de fonóns en este material. Pequenas concentracións de defectos poden afectar a unha ampla poboación de fonóns, afectando así ácondutividade térmica do material. O parámetro de dispersión debido ao tamaño, no que se teñen en conta tanto os bordes de gran como las paredes de dominio ferroeléctricas que

se esperan neste material, ten valores baixos en tódalas mostras, sen embargo os defectos puntuais seguen tendo o maior control nas mostras, polo que este material debe ser fabricado con una moi baixa concentración de defectos para así poder ter una maior posibilidade de control sobre a súa condutividade térmica.

Capas finas de $PbTiO_3$

Este capítulo mostra un estudio similar ao anterior, no que se busca comprender o efecto da estequiometría nas paredes de dominio ferroeléctricas e la condutividade térmica do $PbTiO_3$ (PTO). Para realizar este estudo, depositouse mediante MBE sobre una oblea de STO (001) sen rotación, tendo as fontes de Ti e Pb separadas de forma que se dese lugar a un gradiente de concentracións a través dun diámetro da oblea, que despois foi cortada en 7 mostras.

A composición comprobouse mediante SEM-EDX, co resultado esperado, obtendo unha maior concentración de Ti canto máis cerca da fonte de Ti estivese esa mostra e de forma análoga para o Pb cara o outro extremo da oblea.

A análise de XRD tamén confirma isto, xa que a mostra no centro ten un parámetro de rede de 4.152 Å, que diminúe ao desprazarse do centro, coherente ca relaxación epitaxial a través de vacantes.[215,216] Tanto os XRD, como RSM e rocking-curves ao redor de picos (00l) mostran un estreitamento dos picos ao aloxarse de la relación estequiométrica. Este comportamento no es el esperado, la introdución

de defectos debería dar lugar a unha peor cristalinidade, e polo tanto picos más anchos.

A microscopía de forza de resposta piezoeléctrica (PFM) utilizouse para observar os dominios ferroeléctricos nas diferentes mostras. Esta técnica mostrou unha maior concentración de dominios con distinta orientación para a mostra estequiométrica, diminuíndo ao aumentar a concentración de Pb o Ti. Estas paredes de dominio son as que afectan aos picos nas técnicas de raios X, ensanchándoos, xa que a través de elas hai un cambio en la estrutura que afecta á dispersión dos raios X.

A condutividade térmica das mostras ten un mínimo para a mostra estequiométrica, aumenta ao desviarse da estequiometría para volver a diminuír ao seguir aumentándoa. Isto está causado polo gran efecto das paredes de dominio na mostra estequiométrica, a concentración das cales diminúe ao aumentar os defectos, pero non o suficiente como para baixar a condutividade térmica, de forma que hai dous máximos locais, para novamente diminuír cando a concentración de defectos é demasiado alta, aínda que xa no haxa paredes de dominio.

Os efectos de estes diferentes mecanismos de dispersión vense claramente na análise mediante o modelo de Debye, que precisa dun tamaño moito máis pequeno para a mostra estequiométrica en comparación cas outras, onde se aproxima paulatinamente ao espesor total das capas, usando os datos de EDX para calcular a difusión causada polos defectos e deixando o parámetro de Umklapp axustar,

sen unha clara tendencia, aínda que ten un máximo na mostra estequiométrica.

CONCLUSIÓNS XERAIS

O traballo de esta tese demostra por un lado a importancia de ter en conta fonóns coherentes nas superredes, xa que incluso con espesores totais e de cada capa elevados poden transportar calor a través da estrutura completa para espesores de máis de 100 nm. Demostramos como a tamaños baixos a contribución de fonóns coherentes aumenta, aínda que cambios na estrutura poden levar a modificar novamente a súa contribución.

En relación cos materiais ferroeléctricos, demóstrase que é importante ter en conta o efecto que os defectos catiónicos poden ter sobre a condutividade térmica e sobre as propiedades ferroeléctricas de eles mesmos, á hora de deseñar dispositivos baseados neles ca idea de controlar a condutividade térmica dun material de forma activa. No caso do BTO sobre STO é relevante coñecer tamén a estrutura da capa fina, xa que a policristalinidade afectará ao mesmo parámetro que as paredes de dominio, reducindo o posible efecto total que estas puideran ter sobre a condutividade térmica do dispositivo.

BIBLIOGRAPHY

1. The Nobel Prize in Physics 1956 - NobelPrize.org. https://www.nobelprize.org/prizes/physics/1956/summary/.

2. Hill, M. N. *Physical Oceanography*. (Harvard University Press, 1962).

3. Wells, P. N. T. Ultrasound imaging. *Physics in Medicine and Biology* vol. 51 R83 (2006).

4. Ziman, J. M. *Electrons and Phonons - The Theory of Transport Phenomena in Solids*. (Oxford University Press, 1960).

5. Maldovan, M. Sound and heat revolutions in phononics. *Nature* **503**, 209–217 (2013).

6. Schmotz, M., Maier, J., Scheer, E. & Leiderer, P. A thermal diode using phonon rectification. *New J. Phys.* **13**, 113027 (2011).

7. Liang, B., Guo, X. S., Tu, J., Zhang, D. & Cheng, J. C. An acoustic rectifier. *Nat. Mater.* **9**, 989–992 (2010).

8. Li, X. F. *et al.* Tunable unidirectional sound propagation through a sonic-crystal-based acoustic diode. *Phys. Rev. Lett.* **106**, 084301 (2011).

9. Li, N. *et al.* Colloquium: Phononics: Manipulating heat flow with electronic analogs and beyond. *Rev. Mod. Phys.* **84**, 1045–1066 (2012).

10. Wang, L. & Li, B. Thermal logic gates: Computation with phonons. *Phys. Rev. Lett.* **99**, 177208 (2007).

11. Ruskov, R. & Tahan, C. On-chip cavity quantum phonodynamics with an acceptor qubit in silicon. *Phys. Rev. B - Condens. Matter Mater. Phys.* **88**, 064308 (2013).

12. Ravichandran, J. *et al.* Crossover from incoherent to coherent phonon scattering in epitaxial oxide superlattices. *Nat. Mater.*

13, 168–172 (2014).

13. Luckyanova, M. N. *et al.* Coherent phonon heat conduction in superlattices. *Science (80-.).* **338**, 936–939 (2012).

14. Simkin, M. V. & Mahan, G. D. Minimum Thermal Conductivity of Superlattices. *Phys. Rev. Lett.* **84**, 927–930 (2000).

15. Ashcroft & Mermin. *Solid State Physics*. *Physics* vol. 06 (2006).

16. Atkins, P. & de Paula, J. *Physical Chemistry*. (Oxford, 2006).

17. Ziman, J. M. *Principles of the theory of solids*. (Cambridge University Press, 1972).

18. Christensen, M. *et al.* Avoided crossing of rattler modes in thermoelectric materials. *Nat. Mater.* **7**, 811–815 (2008).

19. Callaway, J. Model for lattice thermal conductivity at low temperatures. *Phys. Rev.* **113**, 1046–1051 (1959).

20. Grüneisen, E. Theorie des festen Zustandes einatomiger Elemente. *Ann. Phys.* **344**, 257–306 (1912).

21. Walker, C. T. & Pohl, R. O. Phonon scattering by point defects. *Phys. Rev.* **131**, 1433–1442 (1963).

22. Slack, G. A. Thermal Conductivity of CaF_2, MnF_2, CoF_2, and ZnF_2 Crystals. *Phys. Rev.* **122**, 1451–1464 (1961).

23. Slack, G. A. & Galginaitis, S. Thermal Conductivity and Phonon Scattering by Magnetic Impurities in CdTe. *Phys. Rev.* **133**, A253–A268 (1964).

24. Agrawal, B. K. & Verma, G. S. Lattice Thermal Conductivity at Low Temperatures. *Phys. Rev.* **126**, 24–29 (1962).

25. Casimir, H. B. G. Note on the conduction of heat in crystals. *Physica* **5**, 495–500 (1938).

26. Berman, R. The Thermal Conductivity of some Polycrystalline Solids at Low Temperatures. *Proc. Phys. Soc. Sect. A* **65**, 1029–

1040 (1952).

27. Klemens, P. G. The Scattering of Low-Frequency Lattice Waves by Static Imperfections. *Proc. Phys. Soc. Sect. A* **68**, 1113–1128 (1955).

28. Slack, G. A. Thermal Conductivity of MgO, Al2O3, MgAl2O4, and Fe2O4 Crystals from 3 to 300 K. *Phys. Rev.* **126**, 427–441 (1962).

29. Qu, Z., Sparks, T. D., Pan, W. & Clarke, D. R. Thermal conductivity of the gadolinium calcium silicate apatites: Effect of different point defect types. *Acta Mater.* **59**, 3841–3850 (2011).

30. Klemens, P. G. The Thermal Conductivity of Dielectric Solids at Low Temperatures (Theoretical). *Proc. R. Soc. A Math. Phys. Eng. Sci.* **208**, 108–133 (1951).

31. Langenberg, E. *et al.* Analysis of the temperature dependence of the thermal conductivity of insulating single crystal oxides. *APL Mater.* **4**, 104815 (2016).

32. Sarantopoulos, A. *et al.* Electronic Degeneracy and Intrinsic Magnetic Properties of Epitaxial Nb:$SrTiO_3$ Thin Films Controlled by Defects. *Phys. Rev. Lett.* **115**, 166801 (2015).

33. Iglesias, L., Sarantopoulos, A., Magén, C. & Rivadulla, F. Oxygen vacancies in strained SrTiO3 thin films: Formation enthalpy and manipulation. *Phys. Rev. B* (2017) doi:10.1103/PhysRevB.95.165138.

34. Suzuki, T., Nishi, Y. & Fujimoto, M. Defect structure in homoepitaxial non-stoichiometric strontium titanate thin films. *Philos. Mag. A Phys. Condens. Matter, Struct. Defects Mech. Prop.* **80**, 621–637 (2000).

35. Wiedigen, S. *et al.* Interplay of point defects, biaxial strain, and thermal conductivity in homoepitaxial $SrTiO_3$ thin films. *Appl. Phys. Lett.* **100**, 061904 (2012).

36. Fumega, A. O., Fu, Y., Pardo, V. & Singh, D. J. Understanding the lattice thermal conductivity of $SrTiO_3$ from an ab initio perspective. *Phys. Rev. Mater.* **4**, 033606 (2020).

37. Wang, Z., Alaniz, J. E., Jang, W., Garay, J. E. & Dames, C. Thermal conductivity of nanocrystalline silicon: Importance of grain size and frequency-dependent mean free paths. *Nano Lett.* **11**, 2206–2213 (2011).

38. Zhou, C. *et al.* Low voltage and high ON/OFF ratio field-effect transistors based on CVD MoS2 and ultra high-k gate dielectric PZT. *Nanoscale* **7**, 8695–8700 (2015).

39. Griffiths, D. J. *Introduction to electrodynamics*. (Prentice Hall, 1999).

40. Serway, R. A. & Jewett, J. W. J. *Principle of Physics-A Calculus Based Test*. (Brooks/Cole - Thomson Learning).

41. Lemmon, E. W. & Jacobsen, R. T. *Viscosity and Thermal Conductivity Equations for Nitrogen, Oxygen, Argon, and Air*. *International Journal of Thermophysics* vol. 25 (2004).

42. Anthony, T. R. *et al. Thermal diffusivity of isotopically enriched 12C diamond*. *PHYSICAL REVIEW B* vol. 42 (1990).

43. Joulain, K., Ezzahri, Y., Drevillon, J. & Ben-Abdallah, P. Modulation and amplification of radiative far field heat transfer: Towards a simple radiative thermal transistor. *Appl. Phys. Lett.* **106**, 133505 (2015).

44. Sood, A. *et al.* An electrochemical thermal transistor. *Nat. Commun.* **9**, 1–9 (2018).

45. Wang, J.-J., Wang, Y., Ihlefeld, J. F., Hopkins, P. E. & Chen, L.-Q. Tunable thermal conductivity via domain structure engineering in ferroelectric thin films: A phase-field simulation. *Acta Mater.* **111**, 220–231 (2016).

46. Zheng, R., Gao, J., Wang, J. & Chen, G. Reversible temperature regulation of electrical and thermal conductivity using liquid-

solid phase transitions. *Nat. Commun.* **2**, 286–289 (2011).

47. López-Bueno, C. *et al.* Low temperature glass/crystal transition in ionic liquids determined by H-bond: Vs. coulombic strength. *Phys. Chem. Chem. Phys.* **22**, 20524–20530 (2020).

48. Qin, G., Wang, H., Zhang, L., Qin, Z. & Hu, M. Giant effect of spin–lattice coupling on the thermal transport in two-dimensional ferromagnetic CrI_3. *J. Mater. Chem. C* **8**, 3520–3526 (2020).

49. Shafiee, S., McCay, M. H. & Kuravi, S. Effect of magnetic fields on thermal conductivity in a ferromagnetic packed bed. *Exp. Therm. Fluid Sci.* **86**, 160–167 (2017).

50. Maldovan, M. Phonon wave interference and thermal bandgap materials. *Nat. Mater.* **14**, 667–674 (2015).

51. Yu, J. K., Mitrovic, S., Tham, D., Varghese, J. & Heath, J. R. Reduction of thermal conductivity in phononic nanomesh structures. *Nat. Nanotechnol.* **5**, 718–721 (2010).

52. Pernot, G. *et al.* Precise control of thermal conductivity at the nanoscale through individual phonon-scattering barriers. *Nat. Mater.* **9**, 491–495 (2010).

53. Zhao, L. D. *et al.* Ultralow thermal conductivity and high thermoelectric figure of merit in SnSe crystals. *Nature* **508**, 373–377 (2014).

54. Kim, W. *et al.* Thermal conductivity reduction and thermoelectric figure of merit increase by embedding nanoparticles in crystalline semiconductors. *Phys. Rev. Lett.* **96**, 045901 (2006).

55. Kittel, C. *Introduction to Solid State Physics. (5th Edition) by John Wiley & Sons NY* (1976).

56. Valasek, J. Piezoelectric and allied phenomena in Rochelle salt. *Phys. Rev.* **15**, 537 (1920).

57. Geideman, W. A. *et al.* PZT thin films for GaAs ferroelectric RAM applications. in 258–262 (Publ by IEEE, 1992). doi:10.1109/isaf.1990.200237.

58. Bersuker, I. B. Recent development of the vibronic theory of ferroelectricity. *Ferroelectrics* **164**, 75–100 (1995).

59. Cochran, W. Crystal stability and the theory of ferroelectricity. *Phys. Rev. Lett.* **3**, 412–414 (1959).

60. Roychowdhury, S. *et al.* Soft Phonon Modes Leading to Ultralow Thermal Conductivity and High Thermoelectric Performance in AgCuTe. *Angew. Chemie* **130**, 4107–4111 (2018).

61. Delaire, O. *et al.* Giant anharmonic phonon scattering in PbTe. *Nat. Mater.* **10**, 614–619 (2011).

62. Fleury, P. A., Scott, J. F. & Worlock, J. M. Soft phonon modes and the 110°K phase transition in $SrTiO_3$. *Phys. Rev. Lett.* **21**, 16–19 (1968).

63. Müller, K. A. & Burkard, H. $SrTiO_3$: An intrinsic quantum paraelectric below 4 K. *Phys. Rev. B* **19**, 3593–3602 (1979).

64. Sarantopoulos, A. *et al.* Reduction of thermal conductivity in ferroelectric $SrTiO_3$ thin films. *Phys. Rev. Mater.* **4**, 054002 (2020).

65. Langenberg, E. *et al.* Ferroelectric domain walls in $PbTiO_3$ are effective regulators of heat flow at room temperature. *Nano Lett.* **19**, acs.nanolett.9b02991 (2019).

66. De Luca, G. *et al.* Domain Wall Architecture in Tetragonal Ferroelectric Thin Films. *Adv. Mater.* **29**, 1605145 (2017).

67. Huyan, H., Li, L., Addiego, C., Gao, W. & Pan, X. Structures and electronic properties of domain walls in $BiFeO_3$ thin films. *Natl. Sci. Rev.* **6**, 669–683 (2019).

68. Langenberg, E. *et al.* Strain-Engineered Ferroelastic Structures

in $PbTiO_3$ Films and Their Control by Electric Fields. *ACS Appl. Mater. Interfaces* **12**, 20691–20703 (2020).

69. Jiang, J. *et al.* Temporary formation of highly conducting domain walls for non-destructive read-out of ferroelectric domain-wall resistance switching memories. *Nat. Mater.* **17**, 49–55 (2018).

70. Seidel, J. *et al.* Conduction at domain walls in oxide multiferroics. *Nat. Mater.* **8**, 229–234 (2009).

71. Huang, H. H. *et al.* Nanoscale Origins of Ferroelastic Domain Wall Mobility in Ferroelectric Multilayers. *ACS Nano* **10**, 10126–10134 (2016).

72. Buscaglia, V. & Randall, C. A. Size and scaling effects in barium titanate. An overview. *Journal of the European Ceramic Society* vol. 40 3744–3758 (2020).

73. Shin, Y. H., Grinberg, I., Chen, I. W. & Rappe, A. M. Nucleation and growth mechanism of ferroelectric domain-wall motion. *Nature* **449**, 881–884 (2007).

74. Gu, Y., Hong, Z., Britson, J. & Chen, L. Q. Nanoscale mechanical switching of ferroelectric polarization via flexoelectricity. *Appl. Phys. Lett.* **106**, 022904 (2015).

75. Royo, M., Escorihuela-Sayalero, C., Íñiguez, J. & Rurali, R. Ferroelectric domain wall phonon polarizer. *Phys. Rev. Mater.* **1**, 051402 (2017).

76. Seijas-Bellido, J. A. *et al.* A phononic switch based on ferroelectric domain walls. *Phys. Rev. B* **96**, 140101 (2017).

77. Seijas-Bellido, J. A., Aramberri, H., Íñiguez, J. & Rurali, R. Electric control of the heat flux through electrophononic effects. *Phys. Rev. B* **97**, 184306 (2018).

78. Torres, P., Íñiguez, J. & Rurali, R. Giant Electrophononic Response in $PbTiO_3$ by Strain Engineering. *Phys. Rev. Lett.* **123**, 185901 (2019).

79. Foley, B. M. *et al.* Voltage-Controlled Bistable Thermal Conductivity in Suspended Ferroelectric Thin-Film Membranes. *ACS Appl. Mater. Interfaces* **10**, 25493–25501 (2018).

80. Mante, A. J. H. & Volger, J. Phonon transport in barium titanate. *Physica* **52**, 577–604 (1971).

81. Northrop, G. A., Cotts, E. J., Anderson, A. C. & Wolfe, J. P. Phonon Imaging of Highly Dislocated LiF. *Phys. Rev. Lett.* **49**, 54–57 (1982).

82. Weilert, M. A., Msall, M. E., Wolfe, J. P. & Anderson, A. C. Mode dependent scattering of phonons by domain walls in ferroelectric KDP. *Zeitschrift für Phys. B Condens. Matter* **91**, 179–188 (1993).

83. Liu, C., Chen, Y. & Dames, C. Electric-Field-Controlled Thermal Switch in Ferroelectric Materials Using First-Principles Calculations and Domain-Wall Engineering. *Phys. Rev. Appl.* **11**, 044002 (2019).

84. Ihlefeld, J. F. *et al.* Room-temperature voltage tunable phonon thermal conductivity via reconfigurable interfaces in ferroelectric thin films. *Nano Lett.* **15**, 1791–1795 (2015).

85. Breckenfeld, E. *et al.* Effect of Growth Induced (Non)Stoichiometry on the Structure, Dielectric Response, and Thermal Conductivity of $SrTiO_3$ Thin Films. *Chem. Mater.* **24**, 331–337 (2012).

86. Brooks, C. M. *et al.* Tuning thermal conductivity in homoepitaxial $SrTiO_3$ films via defects. *Appl. Phys. Lett.* **107**, 051902 (2015).

87. Sarantopoulos, A., Ong, W.-L., Malen, J. A. & Rivadulla, F. Effect of epitaxial strain and vacancies on the ferroelectric-like response of $CaTiO_3$ thin films. *Appl. Phys. Lett.* **113**, 182902 (2018).

88. Birkholz, M. *Thin Film Analysis by X-Ray Scattering*. (Wiley-

VCH, 2006).

89. Ewald, P. P. Introduction to the dynamical theory of X-ray diffraction. *Acta Crystallogr. Sect. A* **25**, 103–108 (1969).

90. Parker, M. W. Protein Structure from X-Ray Diffraction. in *Journal of Biological Physics* vol. 29 341–362 (Springer, 2003).

91. Komar, P. & Jakob, G. CADEM: calculate X-ray diffraction of epitaxial multilayers. *J. Appl. Crystallogr.* **50**, 288–292 (2017).

92. *International tables for X-ray crystallography*. (The Kynoch Press, 1964).

93. Peng, L. M., Ren, G., Dudarev, S. L. & Whelan, M. J. Debye-Waller factors and absorptive scattering factors of elemental crystals. *Acta Crystallogr. Sect. A Found. Crystallogr.* **52**, 456–470 (1996).

94. Ramanand, A. & Ramji Rao, R. Debye-Waller Factor and the Lindemann Parameter of Some Hexagonal Close-Packed Metals. *Can. J. Phys.* **58**, 384–387 (1980).

95. Atomic Scattering Factor. http://www.ruppweb.org/new_comp/scattering_factors.htm.

96. AMASS | XRD Analysis Software | Malvern Panalytical. https://www.malvernpanalytical.com/en/products/category/software/x-ray-diffraction-software/AMASS/.

97. Cahill, D. G. Thermal conductivity measurement from 30 to 750 K: The 3ω method. *Rev. Sci. Instrum.* **61**, 802–808 (1990).

98. Cahill, D. G. & Pohl, R. O. Thermal conductivity of amorphous solids above the plateau. *Phys. Rev. B* **35**, 4067–4073 (1987).

99. Carslaw, H. S. & Jaeger, J. C. *Conduction of Heat in Solids*. (Oxford University Press, 1959).

100. López-Bueno, C., Bugallo, D., Leborán, V. & Rivadulla, F. Sub-μL measurements of the thermal conductivity and heat capacity of liquids. *Phys. Chem. Chem. Phys.* (2018)

doi:10.1039/c8cp00165k.

101. Cahill, D. G., Katiyar, M. & Abelson, J. R. Thermal conductivity of a-Si:H thin films. *Phys. Rev. B* **50**, 6077–6081 (1994).

102. Pishchik, V. *et al.* Properties of Sapphire. in *Sapphire* 55–176 (Springer US, 2009). doi:10.1007/978-0-387-85695-7_2.

103. Nan, C.-W. & Birringer, R. Determining the Kapitza resistance and the thermal conductivity of polycrystals: A simple model. *Phys. Rev. B* **57**, 8264–8268 (1998).

104. Yang, H.-S., Bai, G.-R., Thompson, L. J. & Eastman, J. A. Interfacial thermal resistance in nanocrystalline yttria-stabilized zirconia. *Acta Mater.* **50**, 2309–2317 (2002).

105. Lambropoulos, J. C. *et al.* Thermal conductivity of dielectric thin films. *J. Appl. Phys.* **66**, 4230 (1989).

106. Yamane, T., Nagai, N., Katayama, S. I. & Todoki, M. Measurement of thermal conductivity of silicon dioxide thin films using a 3ω method. *J. Appl. Phys.* **91**, 9772–9776 (2002).

107. Cahill, D. G., Fischer, H. E., Klitsner, T., Swartz, E. T. & Pohl, R. O. Thermal conductivity of thin films: Measurements and understanding. *J. Vac. Sci. Technol. A Vacuum, Surfaces, Film.* **7**, 1259–1266 (1989).

108. Dechaumphai, E. & Chen, R. Thermal transport in phononic crystals: The role of zone folding effect. *J. Appl. Phys* **111**, 73508 (2012).

109. Chakraborty, S. *et al.* Thermal conductivity in strain symmetrized Si/Ge superlattices on Si(111). *Appl. Phys. Lett.* **83**, 4184–4186 (2003).

110. Venkatasubramanian, R. Lattice thermal conductivity reduction and phonon localizationlike behavior in superlattice structures. *Phys. Rev. B - Condens. Matter Mater. Phys.* **61**, 3091–3097 (2000).

111. Hicks, L. D. & Dresselhaus, M. S. Effect of quantum-well structures on the thermoelectric figure of merit. *Phys. Rev. B* **47**, 12727–12731 (1993).

112. Touzelbaev, M. N., Zhou, P., Venkatasubramanian, R. & Goodson, K. E. Thermal characterization of Bi_2Te_3/Sb_2Te_3 superlattices. (2001) doi:10.1063/1.1374458.

113. Cheaito, R. *et al.* Interplay between total thickness and period thickness in the phonon thermal conductivity of superlattices from the nanoscale to the microscale: Coherent versus incoherent phonon transport. *Phys. Rev. B* **97**, 085306 (2018).

114. Luckyanova, M. N. *et al.* Coherent phonon heat conduction in superlattices. *Science (80-.).* **338**, 936–939 (2012).

115. Choi, K. J. Enhancement of Ferroelectricity in Strained $BaTiO_3$ Thin Films. *Science (80-.).* **306**, 1005–1009 (2004).

116. Yanase, N., Abe, K., Fukushima, N. & Kawakubo, T. Thickness Dependence of Ferroelectricity in Heteroepitaxial $BaTiO_3$ Thin Film Capacitors. *Jpn. J. Appl. Phys.* **38**, 5305–5308 (1999).

117. Katsufuji, T., Saiki, T., Okubo, S., Katayama, Y. & Ueno, K. Thermal conductivity of $SrVO_3$−$SrTiO_3$ thin films: Evidence of intrinsic thermal resistance at the interface between oxide layers. *Phys. Rev. Mater.* **2**, 051002 (2018).

118. Capinski, W. S. & Maris, H. J. Thermal conductivity of GaAs/AlAs superlattices. *Phys. B Condens. Matter* **219–220**, 699–701 (1996).

119. Luckyanova, M. N. *et al. P H Y S I C S Phonon localization in heat conduction*. (2018).

120. Rogers, R. Deep Ocean Sediment–Hydrate Relationships. in *Offshore Gas Hydrates* 21–63 (Elsevier, 2015). doi:10.1016/b978-0-12-802319-8.00002-4.

121. Eason, R. *Pulsed Laser Deposition of Thin Films*. vol. 4 (John Wiley & Sons, Inc., 2006).

122. Cheung, J. & Horwitz, J. Pulsed Laser Deposition History and Laser-Target Interactions. *MRS Bull.* **17**, 30–36 (1992).

123. Hubler, G. K. Pulsed Laser Deposition. *MRS Bull.* **17**, 26–29 (1992).

124. Barker, A. S. & Tinkham, M. Far-infrared ferroelectric vibration mode in $SrTiO_3$. *Phys. Rev.* **125**, 1527–1530 (1962).

125. Bell, R. O. & Rupprecht, G. Elastic constants of strontium titanate. *Phys. Rev.* **129**, 90–94 (1963).

126. Haeni, J. H. *et al.* Room-temperature ferroelectricity in strained $SrTiO_3$. *Nature* **430**, 758–761 (2004).

127. Nuzhnyy, D. *et al.* Soft mode behavior in $SrTiO_3$/$DyScO_3$ thin films: Evidence of ferroelectric and antiferrodistortive phase transitions. *Appl. Phys. Lett.* **95**, 232902 (2009).

128. Biegalski, M. D. *et al.* Relaxor ferroelectricity in strained epitaxial SrTiO3 thin films on $DyScO_3$ substrates. *Appl. Phys. Lett.* **88**, 192907 (2006).

129. Lee, C.-H. *et al.* Effect of stoichiometry on the dielectric properties and soft mode behavior of strained epitaxial $SrTiO_3$ thin films on $DyScO_3$ substrates. *Appl. Phys. Lett.* **102**, 082905 (2013).

130. Jang, H. W. *et al.* Ferroelectricity in Strain-Free $SrTiO_3$ Thin Films. *Phys. Rev. Lett.* **104**, (2010).

131. Ohtomo, A. & Hwang, H. Y. A high-mobility electron gas at the $LaAlO_3$/$SrtiO_3$ heterointerface. *Nature* **427**, 423–426 (2004).

132. Santander-Syro, A. F. *et al.* Two-dimensional electron gas with universal subbands at the surface of $SrTiO_3$. *Nature* **469**, 189 (2011).

133. Mehta, V. V. *et al.* Ferromagnetism in tetragonally distorted $LaCoO_3$ thin films. *J. Appl. Phys.* **105**, 07E503 (2009).

134. Guo, E. J. *et al.* Nanoscale ferroelastic twins formed in strained

$LaCoO_3$ films. *Sci. Adv.* **5**, eaav5050 (2019).

135. Fuchs, D. *et al.* Tuning the magnetic properties of LaCo O3 thin films by epitaxial strain. *Phys. Rev. B - Condens. Matter Mater. Phys.* **77**, 014434 (2008).

136. Fuchs, D. *et al.* Ferromagnetic order in epitaxially strained $LaCoO_3$ thin films. doi:10.1103/PhysRevB.75.144402.

137. Rivadulla, F. *et al.* Strain-induced ferromagnetism and magnetoresistance in epitaxial thin films of $LaCoO_3$ prepared by polymer-assisted deposition. *Chem. Mater.* **25**, (2013).

138. Mompean, F. *et al.* Modified magnetic anisotropy at $LaCoO_3/La_{0.7}Sr_{0.3}MnO_3$ interfaces. *APL Mater.* **5**, 096104 (2017).

139. Gazquez, J. *et al.* Lattice mismatch accommodation via oxygen vacancy ordering in epitaxial $La_{0.5}Sr_{0.5}CoO_{3-\delta}$ thin films. *APL Mater.* **1**, 012105 (2013).

140. Thakur, R., Gaur, N. K. & Thakur, R. K. Effect of cation doping on low-temperature specific heat of $LaCoO_3$ cobaltate. *J. Magn. Magn. Mater.* **325**, 17–23 (2013).

141. Hopkins, P. E. *et al.* Effects of coherent ferroelastic domain walls on the thermal conductivity and Kapitza conductance in bismuth ferrite. *Appl. Phys. Lett.* **102**, 1–5 (2013).

142. Ju, S. *et al.* Designing Nanostructures for Phonon Transport via Bayesian Optimization. *Phys. Rev. X* **7**, 021024 (2017).

143. Hu, R. *et al.* Machine-Learning-Optimized Aperiodic Superlattice Minimizes Coherent Phonon Heat Conduction. *Phys. Rev. X* **10**, (2020).

144. Lu, D. *et al.* Synthesis of freestanding single-crystal perovskite films and heterostructures by etching of sacrificial water-soluble layers. *Nat. Mater.* **15**, 1255–1260 (2016).

145. Chen, Z. *et al.* Freestanding crystalline $YBa_2Cu_3O_{7-x}$

heterostructure membranes. *Phys. Rev. Mater.* **3**, 060801 (2019).

146. Langenberg, E., Maurel, L., Antorrena, G., Algarabel, P. A. & Pardo, J. A. Relaxation Mechanisms and Strain-Controlled Oxygen Vacancies in Epitaxial $SrMnO_3$ Films. *ACS Appl. Mater. Interfaces* (2021) doi:10.1021/acsomega.1c00953.

147. Matthews, J. W. & Blakeslee, A. E. Defects in epitaxial multilayers: I. Misfit dislocations. *J. Cryst. Growth* **27**, 118–125 (1974).

148. Wang, T., Ganguly, K., Marshall, P., Xu, P. & Jalan, B. Cite as. *Appl. Phys. Lett* **103**, 212904 (2013).

149. Wang, Y. *et al.* Interfacial thermal resistance and thermal conductivity in nanograined $SrTiO_3$. *Appl. Phys. Express* **3**, 5–7 (2010).

150. Malhotra, A., Kothari, K. & Maldovan, M. Cross-plane thermal conduction in superlattices: Impact of multiple length scales on phonon transport. *J. Appl. Phys.* **125**, (2019).

151. Chen, G. & Neagu, M. Thermal conductivity and heat transfer in superlattices. *Appl. Phys. Lett.* **71**, 2761–2763 (1997).

152. Gu, Y. *et al.* Controllable oxygen vacancies, orbital occupancy and magnetic ordering in $SrCoO_{3-\delta}$ films. *J. Magn. Magn. Mater.* **454**, 228–236 (2018).

153. Jeen, H. *et al.* Reversible redox reactions in an epitaxially stabilized SrCoO x oxygen sponge. *Nat. Mater.* **12**, 1057–1063 (2013).

154. Hu, S. *et al.* Strain Control of Giant Magnetic Anisotropy in Metallic Perovskite $SrCoO_{3-\delta}$ Thin Films. *ACS Appl. Mater. Interfaces* **10**, 22348–22355 (2018).

155. Balbashov, A. M., Mukhin, A. A., Yu Ivanov, V., Iskhakova, L. D. & Voronchikhina, M. E. Electric and magnetic properties of titanium-cobalt-oxide single crystals produced by floating zone melting with light heating. *Low Temp. Phys.* **43**, 965–970 (2017).

156. Zhang, N. *et al.* Thickness Dependence of Oxygen Vacancy Ordering in Strained $LaCoO_{3-x}$ Thin Films. *J. Phys. Chem. C* **124**, 12492–12501 (2020).

157. Zhang, H. *et al.* Structural and Magnetic Properties of $LaCoO_3$ /$SrTiO_3$ Multilayers. (2016) doi:10.1021/acsami.6b03756.

158. Acosta, M. *et al.* $BaTiO_3$-based piezoelectrics: Fundamentals, current status, and perspectives. *Applied Physics Reviews* vol. 4 41305 (2017).

159. Coursey, P. R. & Brand, K. G. Dielectric constants of some titanates. *Nature* vol. 157 297–298 (1946).

160. Fousek, J. Ferroelectricity: Remarks on historical aspects and present trends. *Ferroelectrics* **113**, 3–20 (1991).

161. Li, C. L., Chen, Z. H., Zhou, Y. L. & Cui, D. F. Effect of oxygen content on the dielectric and ferroelectric properties of laser-deposited $BaTiO_3$ thin films. *J. Phys. Condens. Matter* **13**, 5261–5268 (2001).

162. Li, C., Cui, D., Zhou, Y., Lu, H. & Chen, Z. Asymmetric rocking curve study of the crystal structure orientations for $BaTiO_3$ thin films grown by pulsed laser deposition. *Appl. Surf. Sci.* **136**, 173–177 (1998).

163. Everhardt, A. S., Matzen, S., Domingo, N., Catalan, G. & Noheda, B. Ferroelectric Domain Structures in Low-Strain $BaTiO_3$. *Adv. Electron. Mater.* **2**, (2016).

164. Ramana, E. V. *et al.* Ferroelectric and magnetic properties of Fe-doped $BaTiO_3$ thin films grown by the pulsed laser deposition. *J. Appl. Phys.* **113**, 1–5 (2013).

165. Donovan, B. F., Foley, B. M., Ihlefeld, J. F., Maria, J.-P. P. & Hopkins, P. E. Spectral phonon scattering effects on the thermal conductivity of nano-grained barium titanate. *Appl. Phys. Lett.* **105**, 8–12 (2014).

166. Mante, A. J. H. & Volger, J. The thermal conductivity of $BaTiO_3$

in the neighbourhood of its ferroelectric transition temperatures. *Phys. Lett. A* **24**, 139–140 (1967).

167. Davitadze, S. T. *et al.* Specific heat and thermal conductivity of BaTiO3 polycrystalline thin films. *Appl. Phys. Lett.* **80**, 1631–1633 (2002).

168. Catalan, G., Lukyanchuk, I., Schilling, A., Gregg, J. M. & Scott, J. F. Effect of wall thickness on the ferroelastic domain size of $BaTiO_3$. *J. Mater. Sci.* **44**, 5307–5311 (2009).

169. Luk'yanchuk, I. A., Schilling, A., Gregg, J. M., Catalan, G. & Scott, J. F. Origin of ferroelastic domains in free-standing single-crystal ferroelectric films. *Phys. Rev. B - Condens. Matter Mater. Phys.* **79**, 1–7 (2009).

170. Jezowski, A., Mucha, J., Pazik, R. & Strek, W. Influence of crystallite size on the thermal conductivity in $BaTiO_3$ nanoceramics. *Appl. Phys. Lett.* **90**, 50–52 (2007).

171. de Jong, M. *et al.* Charting the complete elastic properties of inorganic crystalline compounds. *Sci. Data* **2**, 150009 (2015).

172. Ledbetter, H. Grüneisen parameter of $Y_1Ba_2Cu_3O_7$. *Phys. C Supercond. its Appl.* **159**, 488–490 (1989).

173. Ledbetter, H. M., Austin, M. W., Kim, S. A. & Lei, M. Elastic constants and Debye temperature of polycrystalline Y 1 Ba 2 Cu 3 O 7− x. *J. Mater. Res.* **2**, 786–789 (1987).

174. West, A. R. *Solid state chemistry and its applications*. vol. 41 (Wiley, 2014).

175. Oyama, T., Wada, N., Takagi, H. & Yoshiya, M. Trapping of oxygen vacancy at grain boundary and its correlation with local atomic configuration and resultant excess energy in barium titanate: A systematic computational analysis. *Phys. Rev. B - Condens. Matter Mater. Phys.* **82**, 134107 (2010).

176. Tan, Y. *et al.* Unfolding grain size effects in barium titanate ferroelectric ceramics. *Sci. Rep.* **5**, 1–9 (2015).

177. Xiao, X. *et al.* Tailoring the structure and thermoelectric properties of $BaTiO_3$: Via Eu^{2+} substitution. *Phys. Chem. Chem. Phys.* **19**, 13469–13480 (2017).

178. Shuai, Y. *et al.* Decisive role of oxygen vacancy in ferroelectric versus ferromagnetic Mn-doped $BaTiO_3$ thin films. *J. Appl. Phys.* **109**, 084105 (2011).

179. Buscaglia, V. *et al.* Average and local atomic-scale structure in $BaZr_xTi_{1-x}O_3$ (x = 0.10, 0.20, 0.40) ceramics by high-energy x-ray diffraction and Raman spectroscopy. *J. Phys. Condens. Matter* **26**, (2014).

180. Lu, S. G. *et al.* High tunability in compositionally graded epitaxial barium strontium titanate thin films by pulsed-laser deposition. *Appl. Phys. Lett.* **82**, 2877–2879 (2003).

181. Harada, J., Pedersen, T. & Barnea, Z. X-ray and neutron diffraction study of tetragonal barium titanate. *Acta Crystallogr. Sect. A* **26**, 336–344 (1970).

182. Garratt-Reed, A. & Bell, D. *Energy Dispersive X-ray Analysis in the Electron Microscope*. (Garland Science, 2003). doi:10.4324/9780203483428.

183. Kan, D. & Shimakawa, Y. Controlled cation stoichiometry in pulsed laser deposition-grown $BaTiO_3$ epitaxial thin films with laser fluence. *Appl. Phys. Lett.* **99**, 081907 (2011).

184. Dubourdieu, C. *et al.* Switching of ferroelectric polarization in epitaxial BaTiO 3 films on silicon without a conducting bottom electrode. *Nat. Nanotechnol.* **8**, 748–754 (2013).

185. Rhodes, R. G. Structure of $BaTiO_3$ at low temperatures. *Acta Crystallogr.* **2**, 417–419 (1949).

186. Keeble, D. J. *et al.* Nonstoichiometry accommodation in SrTiO3 thin films studied by positron annihilation and electron microscopy. *Phys. Rev. B - Condens. Matter Mater. Phys.* **87**, 195409 (2013).

187. Cao, W. & Randall, C. A. Grain size and domain size relations in bulk ceramic ferroelectric materials. *J. Phys. Chem. Solids* **57**, 1499–1505 (1996).

188. Arlt, G. The Influence Of Microstructure On The Properties Of Ferroelectric Ceramics. *Ferroelectrics* **104**, 217–227 (1990).

189. Speck, J. S. & Pompe, W. Domain configurations due to multiple misfit relaxation mechanisms in epitaxial ferroelectric thin films. I. Theory. *J. Appl. Phys.* **76**, 466–476 (1994).

190. Speck, J. S., Seifert, A., Pompe, W. & Ramesh, R. Domain configurations due to multiple misfit relaxation mechanisms in epitaxial ferroelectric thin films. II. Experimental verification and implications. *J. Appl. Phys.* **76**, 477–483 (1994).

191. Speck, J. S., Daykin, A. C., Seifert, A., Romanov, A. E. & Pompe, W. Domain configurations due to multiple misfit relaxation mechanisms in epitaxial ferroelectric thin films. III. Interfacial defects and domain misorientations. *J. Appl. Phys.* **78**, 1696–1706 (1995).

192. Jehanathan, N., Lebedev, O., Gélard, I., Dubourdieu, C. & Van Tendeloo, G. Structure and defect characterization of multiferroic $ReMnO_3$ films and multilayers by TEM. *Nanotechnology* **21**, (2010).

193. Choi, K. J. *et al.* Enhancement of ferroelectricity in strained BaTiO3 thin films. *Science (80-.).* **306**, 1005–1009 (2004).

194. Tenne, D. A. *et al.* Probing Nanoscale Ferroelectricity by Ultraviolet Raman Spectroscopy. *Science (80-.).* **313**, 1614–1616 (2006).

195. Tenne, D. A. *et al.* Ferroelectricity in Ultrathin $BaTiO_3$ Films: Probing the Size Effect by Ultraviolet Raman Spectroscopy. *Phys. Rev. Lett.* **103**, 177601 (2009).

196. Cross, L. E. & Newham, R. E. History of ferroelectrics, ceramics and civilization. *High Technol. Ceram. past, Present Futur.* **3**,

(1987).

197. Ricote, J. *et al.* A TEM and neutron diffraction study of the local structure in the rhombohedral phase of lead zirconate titanate. *J. Phys. Condens. Matter* **10**, 1767–1786 (1998).

198. Haun, M. J., Furman, E., Jang, S. J. & Cross, L. E. Thermodynamic theory of the lead zirconate-titanate solid solution system, part I: Phenomenology. *Ferroelectrics* **99**, 13–25 (1989).

199. Khaenamkaew, P., Muensit, S., Bdikin, I. K. & Kholkin, A. L. Effect of Zr/Ti ratio on the microstructure and ferroelectric properties of lead zirconate titanate thin films. *Mater. Chem. Phys.* **102**, 159–164 (2007).

200. Remeika, J. P. & Glass, A. M. The growth and ferroelectric properties of high resistivity single crystals of lead titanate. *Mater. Res. Bull.* **5**, 37–45 (1970).

201. Joseph, J., Vimala, T. M., Sivasubramanian, V. & Murthy, V. R. K. Structural investigations on $Pb(Zr_xTi_{1-x})O_3$ solid solutions using the X-ray Rietveld method. *J. Mater. Sci.* **35**, 1571–1575 (2000).

202. Sheng, G. *et al.* Domain stability of $PbTiO_3$ thin films under anisotropic misfit strains: Phase-field simulations. *J. Appl. Phys.* **104**, (2008).

203. Li, Y. L., Hu, S. Y., Liu, Z. K. & Chen, L. Q. Phase-field model of domain structures in ferroelectric thin films. *Appl. Phys. Lett.* **78**, 3878–3880 (2001).

204. Sheng, G. *et al.* Phase-field simulations of thickness-dependent domain stability in PbTiO3thin films. *Acta Mater.* **60**, 3296–3301 (2012).

205. Tachibana, M., Kolodiazhnyi, T. & Takayama-Muromachi, E. Thermal conductivity of perovskite ferroelectrics. *Appl. Phys. Lett.* **93**, 092902 (2008).

206. Hlinka, J. *et al.* Lattice dynamics of ferroelectric $PbTiO_3$ by inelastic neutron scattering. *Phys. Rev. B - Condens. Matter Mater. Phys.* **73**, 140101 (2006).

207. Mccray, W. P. MBE deserves a place in the history books. *Nat. Nanotechnol.* **2**, 259–261 (2007).

208. Arthur, J. R. Interaction of Ga and As 2 Molecular Beams with GaAs Surfaces. (1968) doi:10.1063/1.1656901.

209. Neave, J. H., Joyce, B. A., Dobson, P. J. & Norton, N. Dynamics of film growth of GaAs by MBE from Rheed observations. *Appl. Phys. A Solids Surfaces* **31**, 1–8 (1983).

210. Schlom, D. G. Perspective: Oxide molecular-beam epitaxy rocks! *APL Mater.* **3**, 1–6 (2015).

211. Smith, E. H. *et al.* Exploiting kinetics and thermodynamics to grow phase-pure complex oxides by molecular-beam epitaxy under continuous codeposition. *Phys. Rev. Mater.* **1**, 023403 (2017).

212. Paik, H. *et al.* Adsorption-controlled growth of La-doped $BaSnO_3$ by molecular-beam epitaxy. *APL Mater.* **5**, 116107 (2017).

213. Theis, C. D. & Schlom, D. G. Cheap and stable titanium source for use in oxide molecular beam epitaxy systems. *J. Vac. Sci. Technol. A Vacuum, Surfaces, Film.* **14**, 2677–2679 (1996).

214. Theis, C. D. & Schlom, D. G. The Reactivity of Ozone Incident onto the Surface of Perovskite Thin Films Grown by MBE. in *High Temperature Materials Chemistry IX* (ed. Spear, K. E.) 610–616 (Electrochemical Society, Pennington, 1997).

215. Zhang, H.-T., Dedon, L. R., Martin, L. W. & Engel-Herbert, R. Self-regulated growth of $LaVO_3$ thin films by hybrid molecular beam epitaxy. *Appl. Phys. Lett.* **106**, 233102 (2015).

216. Haislmaier, R. C. *et al.* Unleashing Strain Induced Ferroelectricity in Complex Oxide Thin Films via Precise

Stoichiometry Control. *Adv. Funct. Mater.* **26**, 7271–7279 (2016).

217. Guzman, R., Heuver, J., Matzen, S., Magén, C. & Noheda, B. Structural and magnetic properties of [001] $CoCr_2O_4$ thin films. *Phys. Rev. B* **96**, 104105 (2017).

218. Daumont, C. J. M. *et al.* Epitaxial $TbMnO_3$ thin films on $SrTiO_3$ substrates: a structural study. *J. Phys. Condens. Matter* **21**, 182001 (2009).

219. Tavares, E. C. S., Pizani, P. S. & Eiras, J. A. Short-range disorder in lanthanum-doped lead titanate ceramics probed by Raman scattering. *Appl. Phys. Lett.* **72**, 897–899 (1998).

220. Bartasyte, A. *et al.* Raman Spectroscopy and X-ray Diffraction Studies of Stress Effects in PbTiO3 Thin Films. *2007 Sixt. IEEE Int. Symp. Appl. Ferroelectr.* **54**, 282–284 (2007).

221. Lichtensteiger, C., Weymann, C., Fernandez-Pena, S., Paruch, P. & Triscone, J.-M. Built-in voltage in thin ferroelectric $PbTiO_3$ films: the effect of electrostatic boundary conditions. *New J. Phys.* **18**, 043030 (2016).

222. Weymann, C. *et al.* Full Control of Polarization in Ferroelectric Thin Films Using Growth Temperature to Modulate Defects. *Adv. Electron. Mater.* **6**, 2000852 (2020).

223. Debye, P. Zur theorie der spezifischen wärmen. *Ann. Phys.* **344**, 789–839 (1912).

224. Pandech, N., Sarasamak, K. & Limpijumnong, S. Sound velocities and elastic properties of $PbTiO_3$ and $PbZrO_3$ under pressure: First principles study. *Ceram. Int.* **39**, S277–S281 (2013).

225. Wattanasarn, H. & Seetawan, T. Elastic properties and debye temperature of Zn doped $PbTiO_3$ from first principles calculation. in *Integrated Ferroelectrics* vol. 155 59–65 (Taylor and Francis Inc., 2014).

226. Shannon, R. D. Revised effective ionic radii and systematic studies of interatomic distances in halides and chalcogenides. *Acta Crystallogr. Sect. A* **32**, 751–767 (1976).

227. Huang, X., Jiang, P. & Tanaka, T. A review of dielectric polymer composites with high thermal conductivity. *IEEE Electr. Insul. Mag.* **27**, 8–16 (2011).

USC UNIVERSIDADE DE SANTIAGO DE COMPOSTELA

ANNEX: FIGURE PERMISSIONS

USC UNIVERSIDADE DE SANTIAGO DE COMPOSTELA

USC
UNIVERSIDADE
DE SANTIAGO
DE COMPOSTELA

CCC RightsLink®

Home | Help | Email Support | Sign in | Create Account

Ferroelectric Domain Walls in PbTiO3 Are Effective Regulators of Heat Flow at Room Temperature

Author: Eric Langenberg, Dipanjan Saha, Megan E. Holtz, et al
Publication: Nano Letters
Publisher: American Chemical Society
Date: Nov 1, 2019

Copyright © 2019, American Chemical Society

PERMISSION/LICENSE IS GRANTED FOR YOUR ORDER AT NO CHARGE

This type of permission/license, instead of the standard Terms and Conditions, is sent to you because no fee is being charged for your order. Please note the following:

- Permission is granted for your request in both print and electronic formats, and translations.
- If figures and/or tables were requested, they may be adapted or used in part.
- Please print this page for your records and send a copy of it to your publisher/graduate school.
- Appropriate credit for the requested material should be given as follows: "Reprinted (adapted) with permission from {COMPLETE REFERENCE CITATION}. Copyright {YEAR} American Chemical Society." Insert appropriate information in place of the capitalized words.
- One-time permission is granted only for the use specified in your RightsLink request. No additional uses are granted (such as derivative works or other editions). For any uses, please submit a new request.

If credit is given to another source for the material you requested from RightsLink, permission must be obtained from that source.

BACK CLOSE WINDOW

© 2021 Copyright - All Rights Reserved | Copyright Clearance Center, Inc. | Privacy statement | Terms and Conditions
Comments? We would like to hear from you. E-mail us at customercare@copyright.com

USC
UNIVERSIDADE
DE SANTIAGO
DE COMPOSTELA

ACKNOWLEDGEMENTS

La curiosidad es el motor de la ciencia, y sin duda tengo que agradecer a mi director, Fran, por tu curiosidad incesante, por haber hecho que me pregunte tantas cosas, así como por todos los momentos en los que me has guiado y resuelto dudas, en esta etapa tan difícil que es el doctorado. Espero haber estado a la altura como científico, yo sin duda he aprendido mucho.

Eric, gracias por enseñarme que la ciencia también puede ser más amigable de lo que me parece a veces, tu actitud y personalidad, así como tus conocimientos, me ayudaron mucho, aunque no lo haya dicho abiertamente antes. Creo que ambos mis directores comparten esa curiosidad insaciable y eso al final empuja a querer saber más y más a los que estamos cerca.

Todos los compañeros que he tenido en el laboratorio que me han apoyado y ayudado durante esta etapa: Alexandros, Carlos, Elías, Lucía, Rafa y Víctor; por los momentos tanto en el laboratorio como fuera, gracias. También a todos con los que han estado en algún momento en nuestro laboratorio, especialmente a Irene y Pilar. Además

de todos los compañeros de despacho, con los que pude compartir comida y momentos (antes del coronavirus).

Un agradecimiento especial a Adolfo y Víctor por todos los cálculos ab initio de STO y LCO, además de por la discusión de resultados.

Me gustaría agradecer a todos los profesores que he tenido desde pequeño, especialmente a aquellos que me hicieron querer no solo saber, si no entender todo tipo de cosas. Especialmente quiero nombrar a Jose Antonio, de Cluny, creo que sus clases me marcaron mucho y han hecho de mí una persona mejor y con más hambre de conocimiento, no sé si habría llegado aquí sin él. También al Dr. Florencio Sánchez, del cual aprendí mucho en el máster, siempre agradeceré su apoyo durante y después del máster.

También a todos los amigos que me han apoyado en todo momento, especialmente a toda la gente con los que he compartido momentos musicales, que tanto me ayuda a despejar la mente, algo también necesario durante esta época.

Gracias a mi familia, a mi madre, mi padre y mis hermanos, por soportarme en todo momento y darme siempre su apoyo, por haberme ayudado a ser quien soy y llegar aquí.

Por último, gracias a Natalia, sin quien todo esto habría sido mucho más difícil, gracias por ser siempre mi apoyo.